Department of Physics and Astronomy

University of Heidelberg

Master thesis

in Physics

submitted by

Sandro Kraemer

born in Esslingen am Neckar

2017

Towards Laser Cooling of Beryllium Ions at the ALPHATRAP Experiment

This Master thesis has been carried out by Sandro Kraemer

at the

Max-Planck-Institut für Kernphysik

under the supervision of

Prof. Dr. Klaus Blaum

and

Dr. Sven Sturm

Zusammenfassung

ALPHATRAP ist ein Penningfallen-Experiment zur Messung des g-Faktors des in einem hochgeladenen Ion gebundenen Elektrons. Die hohe Kernladungszahl Z in wasserstoffähnlichen Ionen wie etwa $^{208}Pb^{81+}$ erlaubt eine Überprüfung der Quantenelektrodynamik gebundener Zustände unter höchsten Feldstärken. Kalte Ionen sind für diese hochpräzisen Messungen notwendig, die den kleinen zusätzlichen Einfluss der Quantenelektrodynamik sichtbar machen.

Als neue Entwicklung soll eine Laserkühlung von Beryllium-Ionen zur sympathetischen Kühlung der hochgeladenen Ionen zum Einsatz kommen. Die niedrigeren erreichbaren Temperaturen sollen die Messgenauigkeit weiter erhöhen. Gleichzeitig werden neue Messprozesse wie etwa die gleichzeitige Messung von g-Faktoren an Ionenpaaren, die einen Coulomb-Kristall bilden, möglich.

Im Rahmen dieser Arbeit wurde ein System zur Laserkühlung mit 313 nm Licht am ALPHATRAP-Experiment konzeptioniert. Die Experiment-spezifischen Anforderungen an eine Laserkühlung in einer Penningfalle sowie sympathetisches Kühlen werden diskutiert und die Ergebnisse der Inbetriebnahme des Lasersystems gezeigt.

Abstract

ALPHATRAP is a Penning-trap experiment aiming for the test of bound-state quantum electrodynamics (QED) by measuring the g-factor of electrons bound in highly charged ions up to hydrogen-like $^{208}Pb^{81+}$. The high atomic number Z allows a test of bound-state QED under highest field strengths. Cold ions are necessary for high-precision measurements revealing the small additional effect of QED.

As a novel development, laser cooling of beryllium ions will be used to sympathetically cool highly charged ions. The lower achievable temperatures are expected to further increase the precision of the measurement. Additionally, new measurement schemes such as simultaneous g-factor measurements on Coulomb crystallized ion pairs become feasible.

In the context of this thesis, a concept for implementation of laser cooling at the ALPHATRAP experiment using 313 nm light was developed. The experiment specific requirements on laser cooling in a Penning trap and sympathetic cooling are discussed and the results of the commissioning of the laser system are presented.

Contents

List of Figures

List of Tables

1 Introduction

Quantum Electrodynamics (QED) is among the most stringently tested theories in physics. Being a quantum field theory, it has been mainly developed in the 1940s by Richard Feynman, Shin'ichiro Tomonaga and Julian Schwinger. QED describes the interaction between the electromagnetic field and charged elementary particles extending quantum mechanics and unifying it with special relativity in a common theoretical framework. The first success of QED was the calculation of the energy shift between the 2s and 2p levels in hydrogen, which Eugene Lamb and Robert Retherford had found experimentally in 1947 [1, 2]. To date, many measurements have tested the predictions of QED, culminating in the agreement between the calculated free electron g-factor and its measured counterpart [3, 4].

The behavior of an electron bound to a nucleus forming an atom or ion is described by Bound-State QED (BS-QED). This theoretical framework allows amongst others to calculate magnetic moments of bound electrons to extremely high precision. A number of high-precision experiments using highly charged ions (HCI) stored in Penning traps have not found any deviation from the BS-QED predictions so far [5–9]. As a result of the excellent performance of this framework even in relatively strong field strengths, it was used to determine the electron's mass, one of nature's fundamental constants [10].

A g-factor determination for BS-QED tests in a Penning trap reduces to the measurement of the cyclotron and the Larmor frequency by inducing transitions between Zeeman sub-levels of the trapped ion. The measurement precision is ultimately limited by the stability of the electromagnetic trapping field and the energy of the ion. Improvement of the experimental techniques over the past two decades allowed a striking increase in measurement precision, competing with the decreasing uncertainty of theoretical predictions. Milestones have been the introduction of the double-trap technique and a phase-sensitive cyclotron frequency measurement scheme.

A single electron bound to a heavy nucleus, such as hydrogen-like lead, experiences field strengths close to values where the electric field is predicted to become unstable [11]. The Alphatrap experiment was designed to measure the g-factor of electrons bound in highly charged heavy ions using a Penning trap. However, new challenges arise with the high charge state of the ion under investigation. For instance, the non-destructive spin orientation determination becomes more challenging as the measurement fidelity is expected to decrease. Reducing the energy of the ion helps to increase the reliability of the spin state detection and is at the same time expected to increase the measurement precision.

In order to cool the ion motion beyond the limits of established techniques, laser cooling is currently being implemented at Alphatrap. Direct laser cooling of highly charged ions is however not feasible, as no suitable optical transition is present. A cold singly charged beryllium ion will sympathetically cool the HCI. Beryllium features a suitable transition in the ultraviolet region of the light spectrum at 313 nm. Its laser cooling capability has been shown in a number of experiments in Paul and Penning traps [12, 13]. Laser cooling in

general has however never been applied in g-factor experiments and is expected to increase the accuracy of upcoming next-generation experiments as ALPHATRAP.

While laser cooling is an established technique in many areas of atomic physics, it is challenging to combine it with the stringent requirements on electromagnetic field shape necessary for high-precision g-factor measurements. This thesis focuses on the implementation of laser cooling at the ALPHATRAP experiment. It discusses a concept of axial Doppler cooling of singly charged beryllium ions and addresses the requirements on a suitable laser system. Additionally, it provides the results of the commissioning of the available system.

In the second chapter, a short overview over g-factors and their role in precision tests of QED is given. The necessary experimental techniques for g-factor measurements in Penning traps are presented and the impact of temperature on measurement precision is discussed. It is complemented by a short discussion of laser cooling in Penning traps and sympathetic cooling techniques. The third chapter introduces the ALPHATRAP setup, highlighting its peculiarities with regard to laser cooling and their implications. Laser cooling using beryllium is addressed and the laser system available at ALPHATRAP is presented. The fourth chapter discusses the experimental results of the commissioning of the laser system. The thesis is completed by a conclusion and a short outlook in the fifth chapter.

2 Theory

The g-factor denotes a dimensionless proportionality constant that relates the magnetic moment of a charged particle to its external or internal degree of angular momentum. The magnetic moment μ created by this particle is given by

$$\boldsymbol{\mu} = g\frac{\hbar q_{\text{ion}}}{2m_{\text{ion}}}\frac{\boldsymbol{S}}{\hbar}, \tag{2.1}$$

where $\boldsymbol{S}$ is the angular momentum, q_{ion} the particle's charge and m_{ion} its mass. $\hbar$ denominates the reduced Planck constant. This magnetic moment couples to a magnetic field B and increases classically the systems potential energy by the amount

$$\Delta E = -\boldsymbol{\mu} \cdot \boldsymbol{B}. \tag{2.2}$$

For an electron with angular momentum S, the factor $\mu_{\text{B}} = \hbar e/(2m_e)$ is the so-called Bohr magneton where e is the elementary charge and m_e the electron's mass. The influence of the electron's magnetic moment emerges from a relativistic treatment and appears e.g. in the fine structure splitting in atomic or ionic systems. If the nucleus carries furthermore a nonzero nuclear spin, its magnetic moment creates an additional energy shift giving rise to the hyperfine structure splitting. For the nuclear spin, the nuclear magneton $\mu_{\text{N}} = e/2m_p$ is introduced, where the mass of the electron is replaced by the proton's mass m_p.

2.1 The Electron g-factor

The g-factor was first introduced in 1921 by Alfred Landé, who introduced this factor in his work in order to explain heuristically the observed spectroscopic line splitting as a result of the anomalous Zeeman-effect [14]. For the g-factor of the electron, the term Landé g-factor has been coined. At that time, it was not yet known that the electron carries an additional angular momentum. It took until 1925 before Samuel Goudsmit and George Uhlenbeck introduced the concept of the spin [15]. Two years later, Wolfgang Pauli first used spinors to describe the electron in a still non-relativistic treatment [16]. In 1928 Paul Dirac wrote down his relativistic wave equation for fermionic particles, where the spin, being a relativistic phenomenon, emerged naturally [17]. As a result of this treatment, the electron's g-factor could be derived and its calculated value was found to be in agreement with the findings of previous experiments of Alfred Landé. It turned out that the spin contributes twice as strong to the magnetic moment as the orbital angular momentum.

In 1947 Willis Lamb and Robert Retherford found an energy difference of around 1 GHz between the 2s and 2p levels in hydrogen using microwave spectroscopy, a phenomenon these days known as Lamb shift, that could not be explained using the Dirac treatment of the atom. One year later, the anomalous magnetic moment of the electron was found experimentally by Polykarp Kusch and Henry Foley [18]. These discoveries

triggered the development of renormalization in QED. Julian Schwinger derived the first order radiative correction of the electron g-factor, giving an explanation for the earlier observations [1]. Within the framework of QED, the additional, so-called "anomalous" contributions to the g-factor derived from Dirac theory can be calculated. Nowadays, these QED contributions to the g-factor of the free electron can be evaluated using perturbation theory up to tenth order [4]. Together with the successful development of high-precision experiments, these make the free electron g-factor an ideal observable for testing QED to highest precision [3].

In the following sections role of the g-factor in Dirac theory is explained, QED corrections to the obtained value are outlined and other contributions to the measured value and their implications on the experimental approach are briefly discussed.

2.1.1 Dirac Theory

The electron's spin is a purely relativistic phenomenon. The Dirac equation is a wave equation for fermionic particles and fulfills the requirements of special relativity. Starting with this treatment, the spin magnetic moment emerges naturally. The derivation of the corresponding g-factor constitutes one of its early successes. For the free unbound electron, a Landé g-factor of

$$g_{\text{free}} = 2 \tag{2.3}$$

is obtained [17]. For an electron bound in a central potential of an infinitely heavy and point-like nucleus its g-factor depends on the motional angular momentum quantum number. This was first derived by Gregory Breit in 1928 [19]. The g-factor of an electron in a hydrogen-like system with nuclear charge Z in the ground state is given by [20, 21]:

$$g_{\text{bound,1s}} = \frac{2}{3}\left(1 + 2\sqrt{1-(Z\alpha)^2}\right). \tag{2.4}$$

This g-factor accounts for the presence of the nuclear potential. Being a quantum theory, the description of a particle with the Dirac equation has undergone first quantization. The particle can thus only be in allowed discrete states found as eigenvalues of the Hamilton operator. For the electric field however, a classical description is used. The electric field is quantized in the framework of QED (second quantization) leading to new effects altering the g-factor. Additional effects result from the properties of the nucleus. The observable deviations from Dirac theory constitute the main quantity of interest in all modern g-factor experiments.

2.1.2 QED Contributions

QED is a quantum field theory, describing the interaction of charged particles with a field of photons, quanta of the electromagnetic field. The wave function of the electron is a superposition of all processes including charged particles and photons that are allowed by the rules of quantum mechanics. The solutions for the free electron g-factor can be found perturbatively, classified by the order of perturbation theory used. Contributions can intuitively be thought of as particles involved in processes represented by Feynman diagrams such as in figure 2.1. Virtual particles with lifetimes permitted by Heisenberg's uncertainty principle can be emitted and reabsorbed altering the state of the particle

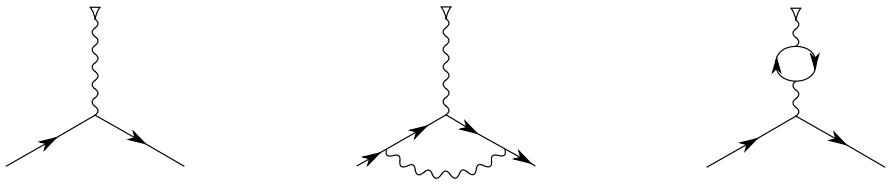

(a) (b) (c)

Figure 2.1: Feynman-diagrams of the tree level and 1-loop QED contributions to the free electron g-factor. The electron is depicted as a solid line propagating in time from the left to the right, a photon is drawn as a wavy line, the triangle represents the external electromagnetic field. The tree level process in (a) gives a g-factor as in equation (2.3). Diagrams (b) and (c) represent the first order corrections. The vertex correction in diagram (b) creates the second term in equation (2.5). (c) is the vacuum polarization correction.

during interaction. Momentum loops, occurring in Feynman diagrams with a closed circle of vertices, give rise to divergences during calculation and make renormalization necessary. The one-loop self energy correction has been calculated by Julian Schwinger in 1948 and yields [1]

$$g_{\text{free}} = 2 + \frac{\alpha}{\pi}. \tag{2.5}$$

Here, α is the dimensionless coupling constant of the electromagnetic field. This process is depicted in figure 2.1 (b). This represents the largest QED contribution, which has a relative size on the order of 10^{-3} compared to the absolute value of the g-factor.

Nowadays higher number of loops are included into the calculation in order to give more accurate results. This makes higher orders of perturbation theory necessary. These results can be expanded in a series of α, where the contributions of different diagrams are merged into the coefficients C_n:

$$g_{\text{free}} = \sum_{n=0}^{\infty} C_n \left(\frac{\alpha}{\pi}\right)^n. \tag{2.6}$$

Here, $C_0 = 2$ is given by the result of Dirac theory (equation (2.3)), while $C_1 = 1$ contains the first order radiative correction in equation (2.5). C_2 and C_3 can be calculated analytically, while for C_4 onwards a numerical evaluation is used. The current most precise value for the g-factor calculated using QED is $g_{\text{free}} = 2.00231930436(154)$. This value incorporates an experimental value of the fine structure constant and the electron to muon mass ratio [4].

The g-factor of the free electron has been measured experimentally among other techniques using Penning traps and the continuous Stern-Gerlach effect (c.f. sections 2.2.1 and 2.2.4). This technique was developed by Hans Dehmelt and co-workers, leading to a precise measurement of the anomalous effect [22]. The currently most precise value was measured in the group of Gerald Gabrielse and yields an experimental value of 2.00231930436146(56) [3]. If QED is assumed to describe nature with sufficient accuracy to be able to fully explain the experimental result, a value of the fine structure constant α can be obtained from the data.

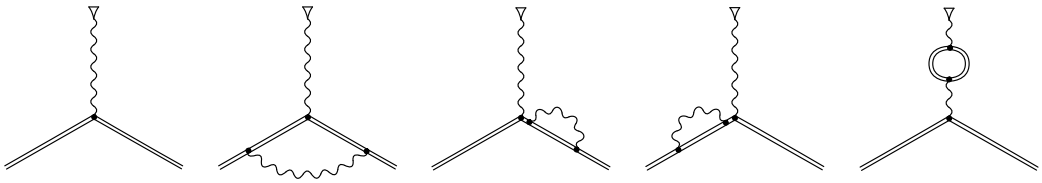

(a) (b) (c) (d) (e)

Figure 2.2: Feynman-diagrams of the tree level and 1-loop QED contributions to the bound electron g-factor. The electron bound to the nucleus with a wave function obtained using the Dirac equation is depicted by a double line. The tree level process in (a) gives a g-factor as in equation (2.4). Diagram (b) represents the vertex correction, diagrams (c) and (d) the self-energy corrections. (e) is the vacuum polarization contribution.

In the case of an electron bound in an atomic or ionic system, the interaction with the nucleus and the other electrons has to be taken into account. To the weak external magnetic field the very strong electromagnetic potential of the nucleus is superimposed. The theoretical framework that is used to describe this situation is called Bound State QED (BS-QED). It incorporates already the relativistic Dirac solution of the electron in the field of the nucleus and constitutes a non-perturbative approach [20]. Feynman-diagrams of the relevant processes to first order are shown in figure 2.2.

A suitable expansion for hydrogen-like systems is again given by [23]

$$g_{\text{bound}} = \sum_{n=0}^{\infty} \tilde{C}_n \left(\frac{\alpha}{\pi}\right)^n . \tag{2.7}$$

Until present, BS-QED calculations for hydrogen-like systems including two-loop corrections are available [24]. Several measurements using Penning traps on hydrogen and lithium-like systems, such as $^{12}C^{5+}$, $^{16}O^{7+}$, $^{28}Si^{13+}$, $^{28}Si^{11+}$, $^{40}Ca^{17+}$ and $^{48}Ca^{17+}$ have found a good agreement between theory and experiment and constitute the most stringent test of BS-QED in the regime of low atomic number Z [5–9]. This led to the most precise determination of the electron mass, assuming again a well understood theory [10].

High Z systems however offer laboratory systems with the strongest available fields on earth, which can be orders of magnitude higher than what can be achieved in the most intense laser fields. The mean field strength of a hydrogen-like system is given in figure 2.3. For high Z systems, it can come close to the Schwinger-limit at $E_s = m_e^2 c^3/e\hbar \approx 1.3 \times 10^{18}\,\mathrm{V\,m^{-1}}$. At this field strength, the electromagnetic field is expected to become nonlinear [11, 25]. For heavy nuclei αZ becomes a value close to one, e.g. for hydrogen-like lead $\alpha Z \approx 0.59$. The ALPHATRAP experiment aims for the measurement of g-factors in high Z systems such as hydrogen-like ^{54}Xe or ^{208}Pb to test BS-QED under these extreme field conditions.

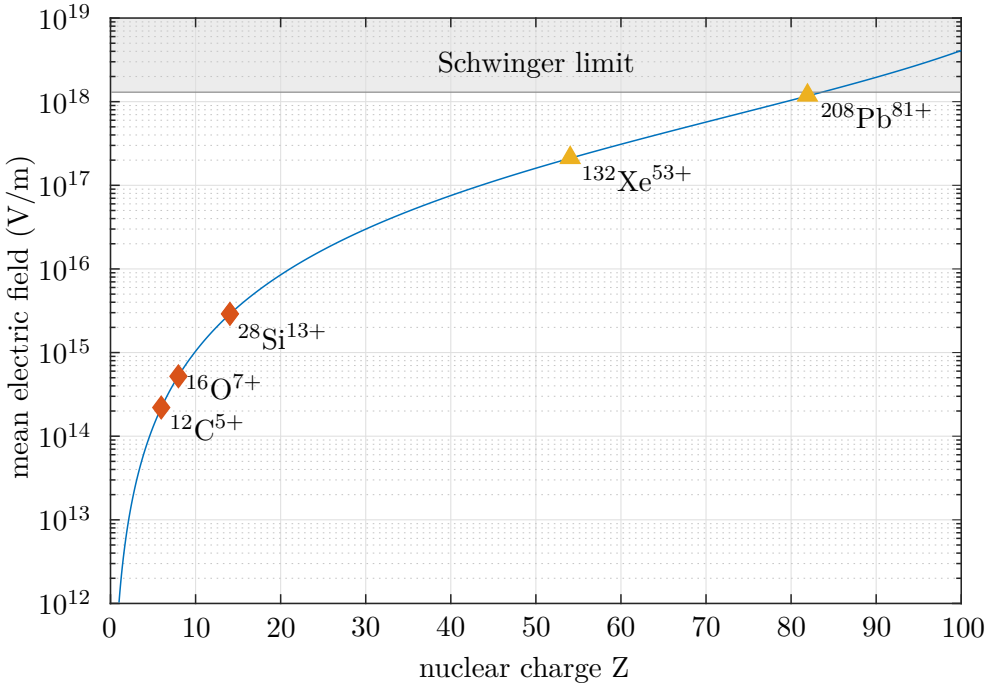

Figure 2.3: Mean nuclear electric field strength $\langle 1s|\hat{E}|1s\rangle$ as a function of the nuclear charge Z in a hydrogen-like system in the ground state. The electric field $E = Z(4\pi\epsilon_0)^{-1}\langle r^{-2}\rangle$ is calculated using the relativistic matrix element from [26]. Diamonds show previous g-factor measurements while triangles represent candidates for ALPHATRAP.

2.1.3 Other Contributions

QED can describe the interaction between photons and leptons. The Standard Model of physics however distinguishes between four different fundamental interactions and four groups of elementary particles. Quantum chromodynamics (QCD) is a field theory describing the interaction of the gluon mediating the strong force and quarks. QCD processes can also be part of the different contributions which describe the dynamics of the electron on a quantum field level. Therefore a small QCD correction has to be added to the g-factor. QCD contributions can be classified into hadronic vacuum polarization processes and hadronic light-by-light scattering processes. Additionally a small contribution due to the electroweak interaction has to be added. However, this contribution is currently below experimental precision [27]. The free electron g-factor can thus be written as

$$g_{\text{free}} = g_{\text{Dirac}} + \Delta g_{\text{QED}} + \Delta g_{\text{hadronic}} + \Delta g_{\text{weak}}. \tag{2.8}$$

g_{Dirac} is given by equation (2.3). Δg_{QED} is given by equation (2.6) when C_0 is set to 0. $\Delta g_{\text{hadronic}}$ is on the order of $2 \cdot 10^{-12}$, while Δg_{weak} is on the order of $3 \cdot 10^{-14}$ [27].

In the case of the bound electron g-factor, a number of contributions due to the interaction

with the nucleus have to be considered:

- nuclear size effect: The Dirac equation assumes a point-like nucleus. The nucleus has however a finite charge distribution characterized by the root mean square radius r_{RMS} and leading to a small correction of the g-factor. It scales in the non-relativistic limit in the ground state of hydrogen-like systems as $\Delta g_{\mathrm{size}} \propto (\alpha Z)^4 \, r_{\mathrm{RMS}}^2$ [28]. Higher moments, such as nuclear quadrupole moment also can influence the g-factor, but are highly suppressed for nuclei with spin zero due to random orientation [20].

- nuclear recoil effect: In the classical treatment of the hydrogen-like atom with the Dirac equation one assumes an infinitely heavy nucleus to obtain analytical solutions. This reduces the system to an one-body problem and neglects the recoil motion of the nucleus. The recoil contribution to the g-factor for the ground state of a hydrogen-like system with a nucleus with mass m_{nuc} becomes $\Delta g_{\mathrm{recoil}} = m_e/m_{\mathrm{nuc}} \, (\alpha Z)^2$ [29].

- nuclear polarization effect: Nuclear models describe the nucleon-nucleon interaction and predict discrete energy levels to which the nucleus can be excited from its ground state. The electron can couple to these excited nuclear states, altering its g-factor. The effect for $^{208}\mathrm{Pb}^{81+}$ has been calculated and contributes with $\Delta g_{\mathrm{polarization}} \approx 2 \cdot 10^{-7}$ [30].

The complete g-factor for a bound electron taking into account the different QED and nuclear corrections thus becomes

$$g_{\mathrm{bound}} = g_{\mathrm{Breit}} + \Delta g_{\mathrm{QED}} + \Delta g_{\mathrm{size}} + \Delta g_{\mathrm{recoil}} + \Delta g_{\mathrm{polarization}}. \tag{2.9}$$

The main contribution for the ground state is given by equation (2.4), while the QED contributions are given by equation (2.7) with $\tilde{C}_0$ set to zero. Hadronic and weak corrections are below the uncertainty of the other contributions and are therefore neglected.

For highly charged ions, the uncertainties of nuclear contributions start to obscure higher order QED contributions. For g-factor differences of two ions with the same nucleus and different electronic configurations however, e.g. a hydrogen-like and a lithium-like system, the nuclear contributions cancel out each other. Laser cooling allows for Coulomb crystallization in the trap strongly coupling both ions. This opens up the opportunity for new measurement schemes aspiring to measure g-factor differences [31]. The leading order contribution of QED corrections given by equation (2.5) is a factor of $\alpha/(2\pi) \approx 0.0012$ smaller than the absolute value of the g-factor. Without increasing the measurement precision, such a difference value would be almost three orders of magnitude more precise. Additionally, weighted g-factor differences aiming for the fine structure constant α have been proposed [32, 33].

2.2 g-factor Measurements in Penning Traps

The most precise measurements of g-factors are performed in Penning traps using a technique developed by Hans Dehmelt [34]. This technique uses transitions between Zeeman levels of the electron for the measurement of the g-factor-resonance.

The coupling of the electron spin to an external magnetic field leads according to equation (2.2) to a splitting into two states distinguished by the spin orientation. The

system precesses around its quantization axis with a fixed frequency called Larmor frequency. The Larmor frequency is given by

$$\nu_L = \frac{1}{2\pi} g \frac{e}{2m_e} B. \tag{2.10}$$

An externally applied magnetic dipole field with a frequency matching the Larmor frequency induces Rabi oscillations between the two energy levels. Applying a resonant π-pulse changes the orientation of the spin. The g-factor measurement technique discussed in the context of this thesis uses a microwave source to alter the spin orientation. The continuous Stern-Gerlach effect is employed to detect the spin state of the electron non-destructively [34].

The motion of a charged particle in a homogeneous magnetic field is characterized by the angular cyclotron frequency

$$\nu_c = \frac{1}{2\pi} \frac{q_{\text{ion}}}{m_{\text{ion}}} B. \tag{2.11}$$

The ion is stored in a Penning trap, which can also be used to determine the cyclotron frequency to the very high precision. Combining equations (2.10) and (2.11), the condition for the g-factor resonance can be written as

$$g = 2 \frac{q_{\text{ion}}}{e} \frac{m_{\text{e}}}{m_{\text{ion}}} \frac{\nu_L}{\nu_c}. \tag{2.12}$$

The measurement scheme at ALPHATRAP reduces thus to a determination of a ratio of frequencies, which can be done with very high precision. The shape of the resonance curve as function of the Larmor frequency is dominated by the cyclotron frequency fluctuations, which are predominantly normally distributed [35]. Modern experiments, such as ALPHATRAP, use an arrangement of several traps optimized for different tasks and transport the ion forth and back without altering its motional or spin state [36]. The measurement precision is ultimately limited by frequency shifts discussed in the last part of this section.

2.2.1 Ion Confinement

SAMUEL EARNSHAW proved in 1942 that no static configuration of either magnetic or electrostatic fields with a potential minimum can be created in order to store a charged particle permanently [37]. However, it is possible to use a superposition of a static magnetic field and an electrostatic potential. This configuration was developed by HANS DEHMELT, who coined the name Penning trap after FRANS MICHEL PENNING and its idea to use magnetic fields to increase the storage time of electrons in vacuum gauges [38].

In an ideal Penning trap, a quadrupolar potential of the form

$$U = U_0 \frac{C_2}{2} \left(2z^2 - x^2 - y^2 \right) \tag{2.13}$$

is superimposed to an homogeneous magnetic field $\mathbf{B} = (0, 0, B_0)'$ along the symmetry axis of the trap. U_0 is the applied voltage and C_2 characterizes the strength of the potential depending on the exact geometry of the electrode configuration. The trajectory of the particle in the trap is governed by the equations of motion $m_{\text{ion}} \ddot{\mathbf{x}} = q_{\text{ion}} \left(-\nabla U + \dot{\mathbf{x}} \times \mathbf{B} \right)$. The

movement along the z-direction consists of harmonic motion with the axial eigenfrequency

$$\nu_z = \frac{1}{2\pi}\sqrt{\frac{2q_{\text{ion}}U_0C_2}{m_{\text{ion}}}}. \tag{2.14}$$

Its trajectory is given by $z(t) = \Re(r_z exp(-i2\pi\nu_z t))$. In this complex notation, r_z contains phase and amplitude information. Motion in the x-y-plane consists of two coupled eigenmotions with eigenfrequencies

$$\nu_+ = \tfrac{1}{2}\left(\nu_c + \sqrt{\nu_c^2 - 2\nu_z^2}\right) \tag{2.15}$$

$$\nu_- = \tfrac{1}{2}\left(\nu_c - \sqrt{\nu_c^2 - 2\nu_z^2}\right). \tag{2.16}$$

The electrostatic potential alters the cyclotron frequency of a charged particle given by equation (2.11) resulting in the so-called modified cyclotron eigenfrequency ν_+. The superposition of an electric and a magnetic field results in a E×B-drift, creating the magnetron motion, which is characterized by the magnetron eigenfrequency ν_-. The motion in the radial plane can be written in complex notation $u(t) = x(t) + iy(t)$ as $u(t) = r_+\exp(-i2\pi\nu_+ t) + r_-\exp(-i2\pi\nu_- t)$. Here, r_+ and r_- contain amplitude and phase information. An example of such a particle trajectory resulting from the three eigenmotions is sketched in figure 2.4 (b).

Closely related to the amplitudes $|r_z|$, $|r_+|$ and $|r_-|$ in the conservative potential of the ideal trap are the eigenenergies of the three modes, which can be defined as [39]

$$E_z = \frac{1}{2}m_{\text{ion}}(2\pi)^2\nu_z^2|r_z|^2 \tag{2.17}$$

$$E_+ = \frac{1}{2}m_{\text{ion}}(2\pi)^2\left(\nu_+^2 - \frac{\nu_z^2}{2}\right)|r_+|^2 \approx \frac{1}{2}m_{\text{ion}}(2\pi)^2\nu_+^2|r_+|^2 \tag{2.18}$$

$$E_- = \frac{1}{2}m_{\text{ion}}(2\pi)^2\left(\nu_-^2 - \frac{\nu_z^2}{2}\right)|r_-|^2 \approx -\frac{1}{4}m_{\text{ion}}(2\pi)^2\nu_z^2|r_-|^2. \tag{2.19}$$

The energy of the magnetron motion is negative[1]. Note that the quadrupolar potential results in eigenfrequencies that are independent of the ion's energy.

Most modern experiments use cylindrically shaped electrodes to create an electrostatic quadrupolar potential at the trap center, while the first Penning traps had electrodes of hyperbolical shape [40]. The cylindrical geometry facilitates bringing ions or electromagnetic waves from outside through the end caps into the trap. Cylindrical traps consist of a ring electrode surrounded by typically one or two sets of correction electrodes and a pair of end cap electrodes. A typical setup for a cylindrical Penning trap is sketched in figure 2.4 (a). This type of trap exhibits cylindrical symmetry around the trap axis orientated along the magnetic field lines and has a symmetric electrode configuration with respect to the central ring electrode. The potential can thus be expanded in a series of Legendre polynomials $P_k(x)$ [41]:

$$U(\rho, z) = U_0\sum_{k=0}^{\infty}C_k\rho^k P_k(\frac{z}{\rho}) \tag{2.20}$$

[1]Reducing the radius $|r_-|$ by laser cooling of the magnetron mode thus leads to an increase in energy E_-.

The coordinate $\rho = \sqrt{x^2 + y^2 + z^2}$ is the distance to the trap center and z designates the component along the trap axis. The coefficients C_k used hereafter describe the geometry of the trap configuration and have a different meaning than the coefficients C_n and $\tilde{C}_n$ in the g-factor expansions in equations (2.6) and (2.7). For symmetry reasons, uneven coefficients C_k are vanishing in most situations and are set to zero hereafter. The coefficient C_0 sets a potential offset and is usually chosen such that the end cap potential corresponds to 0 V and the ring electrode is supplied by U_0.

A quadrupolar potential shape corresponds to vanishing coefficients C_k with $k > 2$ and is realized in real traps only close to the trap center. Higher order contributions are called trap anharmonicities and lead to undesirable energy dependent frequency shifts. Correction electrodes help to enlarge the region where the ion motion can be treated as harmonic. As electrodynamics is a linear theory, the geometric coefficients C_k which create the harmonic potential can be separated into a contribution by the end cap electrodes C_k^{endc} and a contribution by the i-th correction electrode set $C_k^{\mathrm{cor,i}}$ [42]:

$$C_k = C_k^{\mathrm{endc}} + \sum_i C_k^{\mathrm{cor,i}} \frac{U_C^i}{U_0}. \tag{2.21}$$

Here, U_C^i is the voltage supplied to the i-th correction electrode. By choosing the correct geometrical dimensions and an appropriate correction voltage, the leading contributions of trap anharmonicities can cancel out. Choosing the ratio between the correction voltage U_C and the end cap voltage U_0 in a five electrode trap such that $C_4^{\mathrm{endc}} = -C_4^{cor} U_C/U_0$, the shift due to a non vanishing C_4 can be avoided. This voltage ratio is called tuning ratio. By choosing additionally the correct geometrical dimensions (compensated trap) or by using an additional set of correction electrodes (seven electrode trap with two sets of correction electrodes), the tuning ratios can be set such that the C_6 shift cancels out as well [40]. Dimensions and properties of the ALPHATRAP traps can be found in table 3.1.

2.2.2 Interaction with the Resonator

The oscillating ion creates induced charges on the electrodes and, if they are electrically connected by a finite impedance, an image current. The induced charge is given by $q_{\mathrm{ind}}(t) = -q_{\mathrm{ion}} D_{\mathrm{eff}}^{-1} \dot{z}(t)$ and the induced image current is its time derivative $I(t) = \dot{q}_{\mathrm{ind}}(t)$. D_{eff} is the effective distance between two infinitely extended capacitor plates which create the same electric potential as the given trap geometry. The image current induces a voltage drop across the, in general complex, impedance $Z(\nu)$. The real part of the impedance creates a counteracting electric potential in the end caps giving rise to a damping force $F_z = qU D_{\mathrm{eff}}^{-1} = -m_{\mathrm{ion}} \tau^{-1} \dot{z}(t)$. This energy dissipation is characterized by the cooling time constant τ, which can be calculated yielding [35, 43]

$$\tau = \frac{m_{\mathrm{ion}} D_{\mathrm{eff}}^2}{\Re(Z(\nu)) q_{\mathrm{ion}}^2}. \tag{2.22}$$

In practice, the parasitic capacitance of the trap C_p has to be taken into account. To counterbalance the effect of a finite capacitance, a superconducting tank circuit with a inductance L used as a resonator is attached to the trap (see figure 2.5). The ion is cooled until the heating due to Johnson-Nyquist noise of the attached circuit becomes dominant.

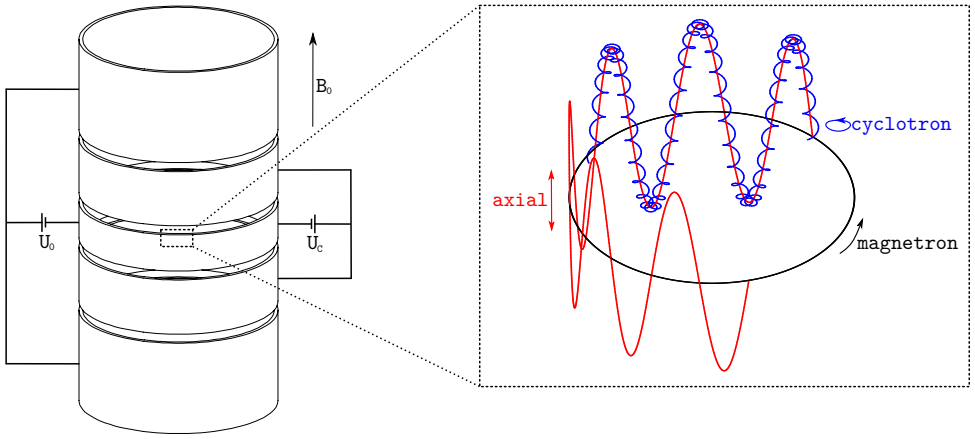

(a) (b)

Figure 2.4: (a) Cylindrical five-pole configuration for a Penning trap. The central ring electrode in the center is surrounded by a pair of correction electrodes supplied with U_C and outer endcap electrodes supplied with U_0. (b) Typical classical trajectory of an ion in the trap with modified cyclotron, axial and magnetron motion.

At this point, the noise keeps the ion at the temperature of the electron plasma in the resonator circuit, implementing a thermal equilibrium with the ion. The potential depth is chosen such that the eigenfrequency of the ion lies close to the maximum of the resonator spectrum.

Ion detection and frequency measurements can be achieved via image current detection. One can show that the ion behaves in the given situation like a series resonance circuit with an effective capacitance $C_{\text{ion}} = q_{\text{ion}}^2 m_{\text{ion}}^{-1} D_{\text{eff}}^{-2} (2\pi\nu_z)^{-2}$ and an effective inductance $L_{\text{ion}} = q_{\text{ion}}^{-2} m_{\text{ion}} D_{\text{eff}}^2$, as shown in figure 2.5 (a) [44, 45]. The ion acts as a sharp filter around the frequency given by the Penning trap. The linewidth of the dip is determined by the Fourier limit of the cooling time constant (2.22) with $\Delta\nu = \tau^{-1}$ and is proportional to the square of the charge and inversely proportional to the mass of the ion. This linewidth sets a minimum measurement time for a single Fourier spectrum. The field fluctuations on this timescale eventually limit measurement precision. Using a fit of the corresponding line shape, the axial and modified cyclotron frequencies can be determined.

If the ion's motional frequency is tuned sufficiently away from the resonance frequency of the resonator, in an ideal Penning trap no heating occurs and the ion preserves its energy forever. In a real Penning trap, so-called anomalous heating occurs, increasing the amplitudes $|r_z|$, $|r_+|$ and $|r_-|$.

2.2.3 Phase Space Distribution and Thermal Energy Fluctuations

The axial motion in the presence of normally distributed noise experiences energy fluctuations. This noise can either originate from anomalous heating or from the electron plasma in the resonator when it is in resonance with the ion. In the latter case, an additional damping

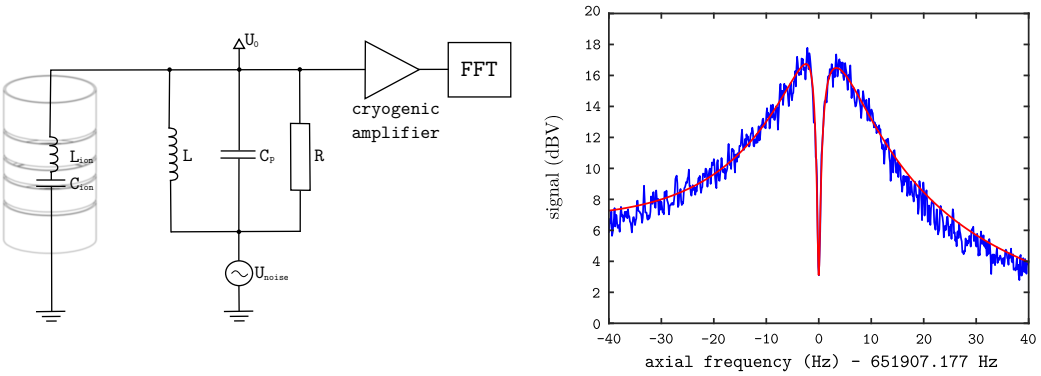

a b

Figure 2.5: Detection system for the image current induced by the axial motion of the ion (a). The parasitic capacitance C_p is created by the trap electrodes and the tank circuit. The ohmic resistance is mainly an effect of the wires connecting the trap with the resonator, which itself is superconducting. U_{noise} is the Johnson-Nyquist-noise of the tank circuits' ohmic resistance. A typical noise spectrum of a resonator with a $^{12}C^{5+}$ ion in the trap is shown in (b). The dip in the center is created by the ion in thermal equilibrium to the resonator. From a fit with the corresponding line shape, the frequency of the ion can be deduced [36].

through the image current has to be considered, omitted below. The energy fluctuations can be treated in a phase space picture of the ion. The amplitude is described by the magnitude of the phase space vector $\tilde{r}$. The classical undisturbed oscillatory motion at angular frequency ω of the particle is then described by $\tilde{r}(t) = \tilde{r}\exp(i\omega t)$, where the phase space vector $\tilde{r}$ can be any complex number. The trajectory and momentum can be obtained from this description by using the relations $z(t) = \Re(\tilde{r}(t))$ and $p(t) = m_{\text{ion}}\omega\Im(\tilde{r(t)})$. This situation is depicted in figure 2.6.

When the ion interacts with the white noise on the electrodes, its position in phase space is smeared out as consequence of the stochastic fluctuations of its phase space vector $\tilde{r}$. The voltage fluctuations on the electrodes can be modeled as a resonant dipole drive $\dot{p} = qUD_{\text{eff}}^{-1}$, yielding an absolute value of the radius fluctuations due to voltage fluctuations given by

$$|\delta\tilde{r}| = \frac{qU}{2i\omega m_{\text{ion}} D_{\text{eff}}}\delta t. \tag{2.23}$$

The direction of the fluctuation vector $\delta\tilde{r}$ in phase space is always pointing along the complex axis. However, the fluctuations occur at points in time isotropically distributed over a motional period. This situation corresponds to a fixed space radius $\tilde{r}$ and a radius fluctuation $\delta\tilde{r}$ with a randomly distributed angle φ between $\tilde{r}$ and $\delta\tilde{r}$. For the energy change during a radius fluctuation $\tilde{r} \to \tilde{r} + \delta\tilde{r}$ one obtains

$$\delta E = \frac{1}{2}m_{\text{ion}}\omega^2\left(2\cos(\varphi)\tilde{r}\delta\tilde{r} + \delta\tilde{r}^2\right) \tag{2.24}$$

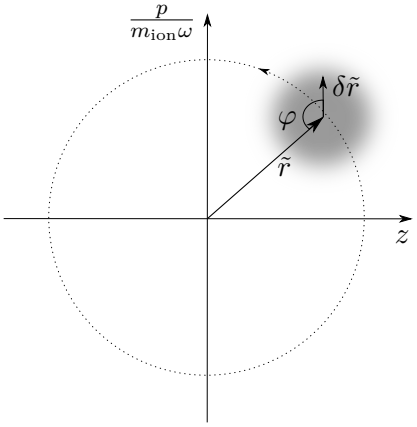

Figure 2.6: Phase space representation of the axial motion. Noise on the electrodes transfers energy to the ion, which performs a random 2d walk in the gray shaded area. The time evolution of the ensemble is represented by the dotted line.

Calculating the first statistical moment of the energy fluctuations induced due to anomalous heating assuming a normally distributed φ and a normally distributed $\delta\tilde{r}$ with variance σ_r^2 yields[2]

$$\langle \delta E^2 \rangle = \left(\frac{1}{2} m_{\mathrm{ion}} \omega^2 \right)^2 \left(2\tilde{r}^2 \langle \delta \tilde{r}^2 \rangle + \langle \delta \tilde{r}^4 \rangle \right). \tag{2.25}$$

The magnitude of thermal energy fluctuations increases thus with the radius of the eigenmotion. This general treatment can be applied to the different modes of a Penning trap, in particular also to the cyclotron mode. The contribution δr_+^4 in real traps becomes very small for $\delta t \to 0$ and its contribution can be neglected. Under this assumption, the energy fluctuations in the cyclotron mode become

$$\langle \delta E_+^2 \rangle \approx \frac{1}{2} m_{\mathrm{ion}} (2\pi)^2 \nu_+^2 r_+^2 \langle \delta r_+^2 \rangle. \tag{2.26}$$

A low energy jitter is important for axial spin detection, especially for highly charged ions as explained in the next section. Laser cooling and mode coupling reduce the amplitudes $|r_+|$ and $|r_z|$, and thereby help to decrease the thermal energy fluctuations.

2.2.4 Continuous Stern-Gerlach Effect

The principle of the continuous Stern-Gerlach Effect is a coupling of the spin orientation to the axial frequency. This can only be done using the magnetic moment as the electron is expected by the Standard Model to have a negligible electric dipole moment [46].

In order to realize this coupling with a sufficient strength, a magnetic bottle is introduced around the trap center, weakly altering the motion of the ion. This magnetic bottle is usually created by a ring electrode made out of ferromagnetic material as shown in figure 2.7 (a). The axial magnetic field component can be developed in analogy to the expansion of the electric potential in (2.20) in a series of Legendre polynomials such that

[2]Here, it is assumed that the voltage noise U on the electrodes is Gaussian white noise.

the z-component becomes

$$B_z(z,\rho) = \sum_{k=0}^{\infty} B_k \rho^k P_k(\frac{z}{\rho}). \tag{2.27}$$

The radial component of the magnetic field is usually very small and the effect on the ion can be neglected. In the region of ion motion near the trap center, the magnetic bottle is approximated as a harmonic potential. Due to symmetry reasons, uneven coefficients B_k are vanishing. The magnetic bottle as seen by the ion thus becomes

$$B_z(z,\rho) = B_0 + \frac{B_2}{2}\left(3z^2 - \rho^2\right). \tag{2.28}$$

The magnetron and the modified cyclotron motion create a current $I_\pm = q_{\text{ion}}\nu_\pm$ causing together with the electron's spin S_z the magnetic moment [35]

$$\mu_z^{S_z} = -I_+\pi\left|r_+\right|^2 - I_-\pi\left|r_-\right|^2 - g\mu_{\text{B}}\frac{S_z}{\hbar} = -\frac{q_{\text{ion}}E_+}{m_{\text{ion}}2\pi\nu_+} + \frac{q_{\text{ion}}E_-\nu_-}{m_{\text{ion}}\pi\nu_z^2} - g\mu_{\text{B}}\frac{S_z}{\hbar}. \tag{2.29}$$

The relation of the radii $|r_+|$ and $|r_-|$ to the energies E_+ and E_- are given by equations (2.18) and (2.19). The z-dependent field creates together with the magnetic moment an additional potential adding to the axial potential. Transforming this expression to a force allows to rewrite the axial equation of motion as

$$\begin{aligned}\ddot{z} &= -(2\pi\nu_z)^2 z + \frac{1}{m_{\text{ion}}}\frac{\mathrm{d}}{\mathrm{d}z}\left(\mu_{\text{z}}\cdot B_{\text{z}}\right) = \\ &\quad -\left((2\pi\nu_z)^2 + \frac{q_{\text{ion}}B_2E_+}{m_{\text{ion}}^2\pi\nu_+} - \frac{2q_{\text{ion}}B_2E_-\nu_-}{m_{\text{ion}}^2\pi\nu_z^2} \pm \frac{g\mu_{\text{B}}B_2}{m_{\text{ion}}}\right)z.\end{aligned} \tag{2.30}$$

For a cooled magnetron and modified cyclotron motion, the frequency shift due to the finite magnetron energy is in most situations negligible compared to the shift due to the cyclotron motion, as $\nu_- \ll \nu_z$. The measured shift due to finite cyclotron energy can serve to determine the temperature of this mode. A fit of a Boltzmann curve to the obtained distribution of axial frequency fluctuations due to thermal energy fluctuations can be used to determine the temperature of the cyclotron mode. At the same time, this frequency shift can be used to detect the spin state: The frequency shift due to the coupling of the spin to the magnetic bottle to the first order neglecting the influence of the magnetron motion is given by

$$\Delta\nu_z \approx \frac{1}{4\pi^2}\frac{B_2}{m_{\text{ion}}\nu_z}\left(\frac{q_{\text{ion}}E_+}{2\pi m_{\text{ion}}\nu_+} \mp \frac{g\mu_{\text{B}}}{2}\right) \approx \frac{1}{4\pi^2}\frac{B_2}{m_{\text{ion}}\nu_z}\left(\frac{E_+}{B_0} \pm \frac{g\mu_{\text{B}}}{2}\right). \tag{2.31}$$

The last approximation assumes $\nu_+ \approx \nu_c$. Thus, a strong magnetic field in combination with weak axial confinement eases the discrimination of spin states. The frequency jump when a spin flip has occurred between two consecutive measurements

$$\Delta\nu_{\text{z}}^{\uparrow} - \Delta\nu_{\text{z}}^{\downarrow} \approx \frac{1}{4\pi^2}\frac{g\mu_{\text{B}}B_2}{m_{\text{ion}}\nu_z} \tag{2.32}$$

can be detected by observing the axial frequency of the ion in a trap with a magnetic bottle. For a reliable spin state detection it is necessary that the random thermal noise of

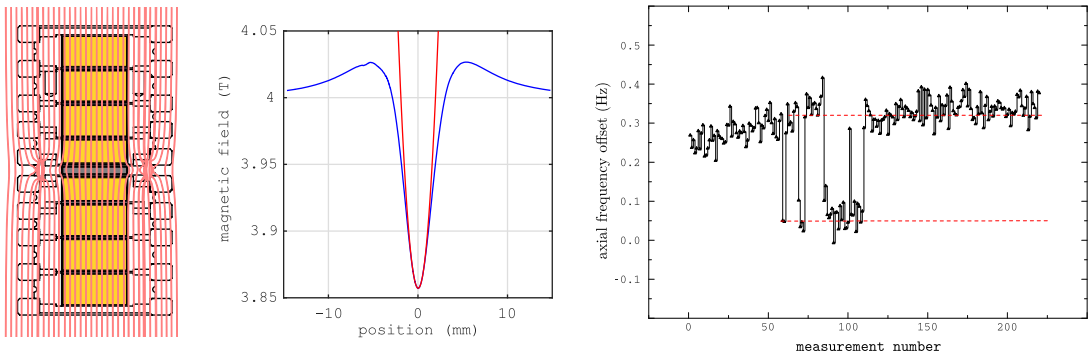

a b c

Figure 2.7: Spin state detection system: (a) shows a model of the Analysis Trap with a magnetic bottle created by an ferromagnetic ring electrode with a simulation of the magnetic field lines drawn in red. In (b) the simulated magnetic field along the trap axis is plotted in blue. An approximated potential with coefficients only up to B_2 is printed in red. (c) shows the measured frequency shift of consecutive measurements on a $^{28}Si^{13+}$-ion. The two spin states are separated by 240 mHz indicated by the two red dashed lines. Figure adapted from [35].

the finite cyclotron energy shift is significantly smaller than the frequency jump given by (2.32). Equation (2.26) shows that the frequency jitter scales with the overall radius of the mode. Strong cooling of the modified cyclotron mode therefore improves the signal-to-noise ratio of the spin state readout. This can be achieved by laser cooling of the axial mode and coupling between the axial and cyclotron motion, as explained below.

2.2.5 Measurement Scheme

The measurement of the spin orientation via the continuous Stern-Gerlach effect needs a strong magnetic inhomogeneity. The accurate measurement of the frequency ratio to find the g-factor resonance however requires a very good magnetic field homogeneity. These two contradictory factors limited the achievable precision of experiments reading out the Larmor and cyclotron frequency in the same region where the spin state is measured. The introduction of the so-called "double-trap technique" allowed to circumvent this contradiction [36]. The setup consists of two separate traps. The spin orientation is determined in a trap called "analysis trap" (AT) with a strong magnetic bottle and connected to an axial resonator. The spin flip is induced in another trap called "precision trap" (PT), where also the measurement of the cyclotron frequency takes place. This trap is characterized by the highest achievable magnetic field homogeneity and connected to an axial resonator. A resonator for the cyclotron mode, connected to split electrodes can be present as well. The ion is transported adiabatically[3] back and forth between these traps without altering the spin state.

The cyclotron frequency ν_c is determined from the measured three eigenfrequencies ν_+,

[3]Here adiabatically refers to a timescale longer than the inverse of the lowest motional frequency ν_-

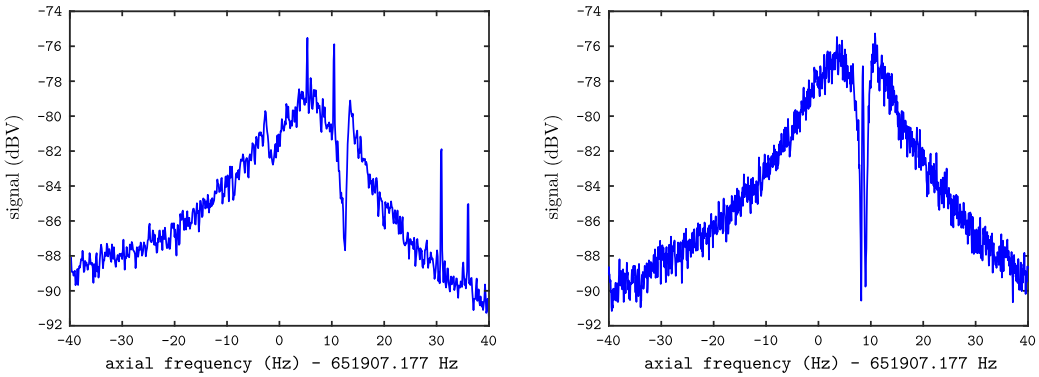

Figure 2.8: Typical spectra of a $^{12}C^{5+}$ ion on the axial resonator when a coupling of the axial mode to the modified cyclotron (left) and magnetron mode (right) is applied. In the left spectrum, additional environmental noise is visible.

ν_z and ν_- using the invariance theorem [43]

$$\nu_c^2 = \nu_+^2 + \nu_z^2 + \nu_-^2. \tag{2.33}$$

This method is generally favored over the summation of modified cyclotron and magnetron frequency $\nu_+ + \nu_- = \nu_c$ as some frequency shifts due to apparatus imperfections cancel out in (2.33), as will be discussed below.

The eigenfrequencies are measured with a resonator attached to one end cap. When a harmonically modulated quadrupolar field is added to the static end cap potential at a specific drive frequency, the modes are coupled and action is transferred between them. This situation can be treated in analogy to an avoided crossing, where usually two electronic eigenmodes are coupled with a resonant light field [47]. The coupling of modified cyclotron and axial mode takes place at a drive frequency $\nu_{dd}^{a,+} = \nu_+ - \nu_z$, coupling between the axial and the magnetron mode is driven by $\nu_{dd}^{a,-} = \nu_- + \nu_z$. Applying π-pulses can swap action between the coupled modes. This technique is useful for transferring energy between modes, as outlined below.

It is further used for frequency determination of the magnetron and modified cyclotron mode. In the presence of a resonant coupling field, sidebands appear in place of the axial frequency dip. The distance of these sideband depends on the coupling strength, which can be chosen such that both dips are visible on the resonator. If ν_u denotes the frequency of the upper sideband and ν_l the frequency of the lower sideband, it can be shown that the relations

$$\nu_+ = \nu_{dd}^{a,+} + \nu_l + \nu_u - \nu_z \tag{2.34}$$

$$\nu_- = \nu_{dd}^{a,-} + \nu_l + \nu_u - \nu_z \tag{2.35}$$

hold. Consecutive measurements of the axial frequency and the lower and upper sideband frequencies reveal the magnetron or modified cyclotron frequency [35]. Typical resonator spectra with a coupling of the modified cyclotron and magnetron to the axial mode are shown in figure 2.8. Another method, based on the ideas of Ramsey interferometry, called

"Pulse 'n Amplify" (PnA) can be used to further increase the precision of the measurement of the motional eigenfrequencies compared to the double-dip method [48].

A complete typical measurement cycle consists of different steps in both traps including the adiabatic transport of the ion between the traps:

- The ion is stored in the AT. Microwaves near the resonance frequency are irradiated until a spin flip can be observed and the spin state is well defined.
- The ion is transported to the PT.
- Cooling of all three modes by means of the resonator damping and coupling of modes is applied.
- The motional eigenfrequencies ν_+, ν_z and ν_- are determined using the double-dip or PnA method.
- Simultaneously, microwaves at a given frequency ν_{mw} are irradiated into the trap.
- The ion is transported to the AT.
- The spin state of the electron is determined.

This process is repeated many times, such that a spin flip probability for a given frequency ratio can be determined. The irradiated microwave frequency ν_{mw} is swept through a range around the expected resonance and the frequency ratio ν_{mw}/ν_c as a function of ν_{mw} is calculated. Combined with the knowledge of the complete line shape of the resonance given in equation (2.12), the g-factor can be determined from a maximum likelihood fit[35].

2.2.6 Frequency Shifts

So far, the Penning-trap system has been described as an ideal system. Finite energies of the eigenstates together with the deviation of the real apparatus from the idealized case and the classical non-relativistic treatment of the particle motion shift the measured eigenfrequencies of the system. These shifts have to be taken into account and they eventually limit the measurement accuracy. The different shifts can be categorized into apparatus shifts, effects induced by the deviation of the real setup from the idealized description, and method inherent effects.

The idealized apparatus assumes a quadrupolar potential as well as a homogeneous magnetic field along the trap axis and for the continuous Stern-Gerlach effect a harmonic magnetic field component along the z-axis. It is further postulated that all fields are constant over time constituting as well an approximation. The relative effect of temporal fluctuations of the electric and magnetic fields over time can be reduced by either increasing their stability or by reducing the measurement time.

The spatial deviation of the electric field from the idealized case leads to non-vanishing coefficients $C_{k>2}$. If an electrostatic (or magnetic) potential is described by higher order coefficients than of second order, the frequency becomes amplitude dependent. The first order frequency shift for the motional eigenfrequencies and the Larmor frequency are given

by the matrix equation [35, 49]

$$\begin{pmatrix} \Delta\nu_+/\nu_+ \\ \Delta\nu_z/\nu_z \\ \Delta\nu_-/\nu_- \\ \Delta\nu_L/\nu_L \end{pmatrix} = \frac{6C_4}{C_2^2} \begin{pmatrix} (\nu_z/\nu_+)^4/4 & -(\nu_z/\nu_+)^2/2 & -(\nu_z/\nu_+)^2 \\ -(\nu_z/\nu_+)^2/2 & 1/4 & 1 \\ -(\nu_z/\nu_+)^2 & 1 & 1 \\ 0 & 0 & 0 \end{pmatrix} \cdot \begin{pmatrix} E_+ \\ E_z \\ E_- \end{pmatrix}. \tag{2.36}$$

All contribution scale linearly with the size of C_4, which can be reduced by choosing an appropriate trap geometry and the correct tuning ratio as described in equation (2.21).

The real magnetic field also deviates from the ideal homogeneous field. The weak components of the radial field compared to the strong axial component make shifts due to a radial field in typical magnetic fields negligible. The z-component can be described by the expansion (2.27) used to describe the effect of the magnetic bottle. A linear magnetic field gradient created by a B_1 term creates a spatially uniform force along the trap axis, shifting the center of motion. This force is independent of the axial energy E_z, but depends via the magnetic moment of the modified cyclotron and magnetron motion on the energies E_+ and E_-. The B_2 term creates a harmonic potential, that gives the largest contribution to the shift of the eigenfrequencies due to magnetic field inhomogeneities [35]:

$$\begin{pmatrix} \Delta\nu_+/\nu_+ \\ \Delta\nu_z/\nu_z \\ \Delta\nu_-/\nu_- \\ \Delta\nu_L/\nu_L \end{pmatrix} = \frac{B_2}{m_{\mathrm{ion}}(2\pi\nu_z)^2 B_0} \begin{pmatrix} -(\nu_z/\nu_+)^2 & 1 & 2 \\ 1 & 0 & -1 \\ 2 & -1 & -2 \\ -(\nu_z/\nu_+)^2 & 1 & 2 \end{pmatrix} \cdot \begin{pmatrix} E_+ \\ E_z \\ E_- \end{pmatrix}. \tag{2.37}$$

Note, that the spin precession frequency ν_L, being a purely magnetic phenomenon, is shifted by the magnetic field inhomogeneities while electric field inhomogeneities do not influence it in the non-relativistic approximation.

An ion coupled to an axial or modified cyclotron resonator is in thermal equilibrium with the thermal bath of the charge carriers. The energy therefore undergoes thermal fluctuations inducing frequency jitter. As a result of the stochastic nature of this jitter, it is impossible to correct for induced shifts limiting the measurement precision. Additionally, the energy fluctuations create thermal noise on the axial signal during the spin orientation measurement with the continuous Stern-Gerlach effect as can be seen from equations (2.31) and (2.37). Reducing the temperature of each mode with an additional cooling mechanism reduces these fluctuations and improves the signal-to-noise ratio of the spin state detection, making a spin orientation measurement in some cases at all possible.

So far, electrodes are assumed to be perfectly cylindrical and the magnetic field to be aligned with the trap axis and thus with the symmetry axis of the electric field. The lowest order deviation from roundness can be characterized by an ellipticity ϵ. If this ellipticity is non-zero and the tilting angle between the magnetic and the electric field θ is non-vanishing, Brown and Gabrielse showed that using the invariance theorem (c.f. equation (2.33)) to calculate the free cyclotron frequency ν_c, the first order shifts cancel out each other. The relative uncertainty of the free cyclotron frequency yields

$$\frac{\Delta\nu_c}{\nu_c} = \sqrt{\left(\frac{\nu_+^2}{\nu_c^2}\frac{\Delta\nu_+}{\nu_+}\right)^2 + \left(\frac{\nu_z^2}{\nu_c^2}\frac{\Delta\nu_z}{\nu_z}\right)^2 + \left(\frac{\nu_-^2}{\nu_c^2}\frac{\Delta\nu_-}{\nu_-}\right)^2}. \tag{2.38}$$

Considering the scaling of the eigenfrequencies for weak axial confinement $\nu_+ \gg \nu_z >\!\!> \nu_-$ it becomes apparent that the relative modified cyclotron error constitutes the largest contribution to the uncertainty of the free cyclotron frequency.

The minimization of the apparatus shifts is, in principle, only limited by the machining and aligning precision. Method inherent effects however constitute a natural lower limit, which cannot be changed by technical means.

One inherent contribution is the image charge effect, which increases with the charge state of the ion. The ion produces image charges on the electrodes, creating an electric field altering the trap frequencies. The influence on the radial motional degrees has been calculated to be approximately $\Delta\nu_\pm \approx \mp q_{\text{ion}}/(8\pi^2\epsilon_0 B_0 d^3 \nu_{pm})$, where d is the typical electrode radius [36]. The shift of the free cyclotron frequency using the invariance theorem (2.33) becomes

$$\frac{\Delta\omega_c}{\omega_c} \approx \left(\frac{\omega_-}{\omega_c} - \frac{\omega_+}{\omega_c}\right) \frac{q_{\text{ion}}}{4\pi\epsilon_0 B_0 \omega_c d^3} \tag{2.39}$$

for split electrodes in a typical mean distance d. This shift decreases with an increasing trap radius and magnetic field B_0. The z-component is negligible if no closed end caps are present, as it is the case in most cylindrical trap geometries. The dominant part due to the image charge effect on the modified cyclotron frequency scales approximately with the mass of the ion. In the ALPHATRAP experiment, this shift for a $^{208}\text{Pb}^{81+}$ ion with the trap parameter d and for $\omega_z \to 0$ would become $\Delta\omega_c/\omega_c \approx -6 \cdot 10^{-9}$ in the AT while for the PT with its larger diameter, the shift would be $\Delta\omega_c/\omega_c \approx -2 \cdot 10^{-10}$.

Another important method inherent shift is the relativistic shift, which is due to the relativistic mass increase $m_{\text{rel}} = \gamma m_{\text{ion}}$ for a fast moving ion with Lorentz factor $\gamma = (1 - v^2/c^2)^{-1/2}$ with velocity v and speed of light c. The shift of the free cyclotron frequency is given by

$$\frac{\Delta\nu_c}{\nu_c} = \frac{\nu_{c,\text{rel}}}{\nu_c} - 1 = \frac{m_{\text{ion}}}{\gamma m_{\text{ion}}} - 1 \approx -\frac{v^2}{2c^2} = -\frac{E_+}{m_{\text{ion}} c^2}. \tag{2.40}$$

Here, only the contribution of the modified cyclotron motion was taken into account. A typical energy for the cyclotron mode of a $^{12}\text{C}^{5+}$ ion in a 4 T magnetic field coupled to the axial mode at $\nu_z = 660\,\text{kHz}$, which is in thermal equilibrium with a cryogenic tank circuit at $T_{\text{res}} = 4.2$ K is given by $E_+ = \nu_+/\nu_z k_B T_{\text{res}} \approx 14\,\text{meV}$ with the Boltzmann constant k_B. The relative relativistic shift for this ion is then $8 \cdot 10^{-12}$. A more detailed calculation reveals the different contributions including also shifts of the Larmor-frequency [43]:

$$\begin{pmatrix} \Delta\nu_+/\nu_+ \\ \Delta\nu_z/\nu_z \\ \Delta\nu_-/\nu_- \\ \Delta\nu_L/\nu_L \end{pmatrix} = \frac{1}{m_{\text{ion}} c^2} \begin{pmatrix} 1 & 1/2 & -(\nu_z/\nu_+)^2 \\ 1/2 & 3/8 & -(\nu_z/\nu_+)^2/4 \\ -(\nu_z/\nu_+)^2 & -(\nu_z/\nu_+)^2/4 & -(\nu_z/\nu_+)^4/4 \\ 2/9 & 1/2 & -(\nu_z/\nu_+)^2 \end{pmatrix} \cdot \begin{pmatrix} E_+ \\ E_z \\ E_- \end{pmatrix}. \tag{2.41}$$

This shift depends on the energy of the ion and can be reduced by cooling of the motional modes. The relativistic mass shift to lowest order scales linear with the energy of the ion, such that cooling can efficiently increase the measurement precision. Note that the axial and the modified cyclotron energy both strongly contribute to the shift of the axial and the modified cyclotron mode.

2.3 Laser Cooling

As showed in the previous section of this chapter, energy dependent frequency shifts constitute a limit for the measurement precision. With increasing loop order however, the effects of BS-QED become smaller and smaller. For this reason, cooling of the ion motion plays an important role in modern Penning-trap g-factor experiments. Additionally, for experiments on HCI using the continuous Stern-Gerlach effect for spin state detection, the spin jump frequency decreases inversely to the mass of the ion in accordance with equation (2.32). Noise due to temperature induced shifts limits the signal-to-noise ratio of the spin detection. Equation 2.26 shows, that decreasing the radius of motion also decreases the noise in the spin state detection.

Established techniques for cooling of the trapped ion are resistive cooling with a resonator as described in section 2.2.1 and electronic feedback cooling [35, 45, 50]. Resistive cooling of the ion's axial mode results in an equilibrium temperature equal to the one of the electron plasma in the resonator, which at ALPHATRAP will be near the boiling temperature of helium. Electronic feedback cooling allows to further decrease the temperature of the mode in thermal contact with the resonator. It has been shown in the g-factor experiment in Mainz that temperatures as low as 250 mK can be achieved [35]. At ALPHATRAP laser cooling should be implemented in order to further reduce the ion's temperature.

Laser cooling was pioneered in the groups around THEODOR HÄNSCH and ARTHUR SCHAWLOW and independently by DAVID WINELAND and HANS DEHMELT for trapped ions [51–53]. For neutral atoms it was later mainly influenced by the development of the Zeeman slower in the group of WILLIAM PHILLIPS and the optical molasses technique pioneered by the group of STEVEN CHU [54, 55]. Laser cooling of neutral atoms and ions has by now become a standard technique in atomic physics. To date, it has however not been used for g-factor experiments in Penning traps.

2.3.1 Doppler Cooling

The principle of laser cooling is based upon the resonant absorption of photons in a closed two-level system and its spontaneous emission. During Doppler cooling, absorption of light leads to a transfer of momentum from the photon to the atom directed along the axis of laser beam propagation. The momentum carried by a single photon is $p = \hbar k$ where $k = 2\pi/\lambda$ is the wavelength-dependent wave vector. The change in velocity, the so-called recoil velocity, of a $^9Be^{1+}$ ion upon the absorption of a single photon with wavelength 313.13 nm can be calculated, yielding approximately $0.14\,\mathrm{m\,s^{-1}}$. While the absorption process is directed, the distribution of the direction of spontaneously emitted photon is spread over the whole solid angle. This leads to a net momentum transfer along the beam axis. At the same time stimulated emission can occur, where the momentum transfer by absorption and emission cancels out. In this section, the fundamental ideas of laser cooling using a classical treatment of the particle's motion is given.

The momentum transfer leads to a light pressure force on the particle. The absolute value of this light pressure force can be written as [56]

$$F_{\mathrm{scatt}} = \hbar k \frac{1}{2\tau} \frac{I/I_{\mathrm{sat}}}{1 + I/I_{\mathrm{sat}} + 4\delta^2\tau^2} \tag{2.42}$$

and is composed of the momentum transfer of a single photon $\hbar k$ and a scattering rate of

the atomic transition of the two-level system. The scattering rate depends on its strength on resonance $(2\tau)^{-1}$ and the detuning from the resonance frequency δ. τ is the lifetime of the upper state under the assumption that the lower state does not decay. Note that this result can be derived from the steady state solution of the optical Bloch equations and has the shape of a Lorentzian. Power broadening of the transition is included and enters in the form of the fraction of the saturation intensity I/I_{sat}, where I is the power density of the laser light. The saturation intensity of a transition in a two-level system describes the intensity at which the upper and lower state are equally populated and is given by [56]

$$I_{\mathrm{sat}} = \frac{\pi}{3}\frac{hc}{\lambda_0^3 \tau}. \tag{2.43}$$

λ_0 is the resonance wavelength of the transition and h denominates the Planck constant. For an electronic transition with wavelength 313.13 nm and a lifetime of 8.1(4) ns as it can be found in $^9\mathrm{Be}^{1+}$ the saturation intensity is hit at $836(42)\,\mathrm{W\,m^{-2}}$ [57].

The net force on an atom or ion depends on the detuning δ of the photon frequency in the rest frame of the atom with respect to the resonant transition frequency $\nu_0 = c/\lambda_0$ between the two states of the two level system. The frequency of the cooling laser beam in the laboratory frame is given by ν_B. The first order Doppler shift modifies the laser frequency seen by the particle in its rest frame and depends on the projection of the particle's velocity $\mathbf{v}$ to the direction of propagation of the laser beam $\mathbf{e_B}$. The detuning of the laser frequency as seen in the rest frame of the atom is given by

$$\delta(v) = \nu_B \left(1 - \frac{\mathbf{v}\cdot\mathbf{e_B}}{c}\right) - \nu_0. \tag{2.44}$$

The Doppler shift makes the light pressure velocity dependent, allowing to address only a certain class of velocities. Lasers used for cooling are usually narrow in linewidth such that they can be assumed to be perfectly monochromatic.

The interaction of the laser beam with the particle has to fulfill energy and momentum conservation. If the laser is detuned to the red side of the resonance frequency by $\delta_B < 0$, energy from the motional state is necessary for the transition, which is only fulfilled for particles moving in the opposite direction of the laser beam. The resonance is driven for those particles where $\delta(v) = \delta_B$. If the laser is detuned to the blue side of the resonance frequency, such that $\delta_B > 0$, the excess energy of the photon is transferred to the motion of the particle (c.f. figure 2.9). For cooling particles, the laser has thus to be red detuned.

The description above assumed a very long lifetime of the upper state and therefore a narrow natural linewidth. With smaller temperatures and smaller velocities, the detuning of the laser must become smaller as can be seen from equation (2.44). The finite natural linewidth leads to an increasing number of absorbed blue detuned photons as the detuning approaches zero. A fundamental lower limit of Doppler cooling is hit, when the heating due to photons on the blue detuned side balances the cooling effect of the red shifted photons. This steady state is called Doppler limit and is usually expressed in terms of a temperature T_D. It was derived to be [56]

$$T_D = \frac{h}{2k_B\tau}. \tag{2.45}$$

This minimum temperature can be reached with a detuning set to $\delta_B = -(2\tau)^{-1}$.

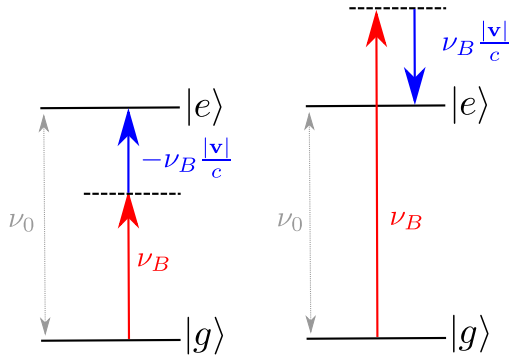

Figure 2.9: Energy diagram of the Two-level system used for laser cooling for red detuning (left) and blue detuning (right) of the laser frequency using a semi-classical description. With red detuning motional energy $h\nu_B \mathbf{v}\cdot\mathbf{e_B}/c$ is absorbed slowing the motion, in the blue detuned case this energy is emitted, accelerating the motion, during a photon-particle interaction. For details, see text.

2.3.2 Laser Cooling in Penning Traps

Compared to the case of neutral atoms, where not only the cooling but also the trapping has to be achieved by means of light pressure, Penning traps offer already a mechanism for storing the ion using the Lorentz force, keeping it on a well defined trajectory [58, 59]. Therefore, a single laser beam in combination with mode coupling is sufficient. At ALPHATRAP the laser beam will be oriented along the symmetry axis of the trap. Assuming a perfectly oriented beam, only a cooling impact on the axial motion is expected. A tilted laser beam with respect to the trap axis introduces a small effect on the cyclotron and magnetron motion. For the magnetron motion, this leads to a heating of the temperature and eventually to ion loss [60].

These difficulties can be resolved by coupling to another eigenmotion by means of an externally applied quadrupolar field (c.f. section 2.2.5). This coupling also allows to cool only a single eigenmotion. With resonant coupling, action is transferred between the eigenmodes. The temperatures of the different modes in thermal equilibrium with an suitable quadrupolar drive applied are related by the trap frequencies with

$$T_+ = \frac{\omega_+}{\omega_z} T_z \tag{2.46}$$

$$T_- = -\frac{\omega_-}{\omega_z} T_z. \tag{2.47}$$

If the axial mode is cooled and coupled to the cyclotron mode, energy is removed from both modes.

Additional difficulties compared to Paul traps arise from the presence of a strong magnetic field, coupling to the spin of the electron and shifting the energy levels. Laser cooling allows to reduce the temperature of ions with a suitable closed optical transition. Typical candidates are $^{24}Mg^{1+}$ and $^{9}Be^{1+}$, but laser cooling has also been demonstrated on $^{40}Ca^{1+}$ [61–63]. For cooling of other ions, an indirect technique has to be used, as discussed below.

2.4 Sympathetic Cooling

Highly charged ions with their tightly bound electrons have dipole transitions with very large energy spacing. Hydrogen-like xenon has a transition wavelength of 0.040 192 nm for the $1s_{1/2} \leftrightarrow 2p_{1/2}$ transition, a wavelength range which lies in the regime of soft X-rays [64]. These ions do not have suitable optical transitions for laser cooling, making sympathetic cooling, thus cooling by interaction with other cooled ion species, necessary. Since all particles in the trap are charged, sympathetic cooling is based on the Coulomb interaction between the ions in the trap which can either be direct or via induced image charges on the trap electrodes. There are two fundamentally different methods, common electrode coupling and the direct Coulomb coupling. For the common electrode coupling the laser cooled ion (LCI) and the HCI are stored in two different potential wells, coupled by the induced image charges on a shared electrode. For direct Coulomb coupling, both ions are stored in the same well resulting in a relative small distance and thus strong interaction between the ions. To date, these techniques have not been used for g-factor measurements in Penning traps. Both methods and their advantages will be sketched and discussed in this section.

2.4.1 Coulomb Crystallization

Sympathetic cooling of a second ion species via a laser coolable species was first experimentally observed in 1980 [61] in a two species non neutral plasma. Since then, several studies in Penning traps have been performed using a large number of ions in the trap. [65–68]. For high-precision g-factor measurements at ALPHATRAP, the number of ions stored in the same trap as the HCI has to be decreased in order to reduce the induced shifts by the ion-ion interaction, called space charge shift [69].

At very low energies, ions undergo a phase transition from chaotic motion to an ordered structure called Coulomb crystals [70]. For a non-neutral plasma of ions of a single species in the trap, the behaviour can be characterized by the Coulomb coupling parameter

$$\Gamma = \frac{q_{\text{ion}}^2}{4\pi\epsilon_0 a_0 k_B T}, \tag{2.48}$$

describing the relative size of the Coulomb potential energy to the thermal energy of the plasma. Here, a_0 denotes the average distance between the ions and T the plasma temperature. It has been shown, that for $\Gamma > 2$, the plasma shows a liquid-like behavior, while around $\Gamma \approx 175$ it experiences a phase transition forming Coulomb crystals [71].

In order to get a rough estimate on the behavior of the ions in such a crystal once cooled to very low temperatures, one can simplify the three-dimensional situation in the Penning trap by limiting the motion of both ions to the symmetry axis of the trap. The trap should by filled with a two-ionic crystal with a laser coolable ion (denominated with index 1) and a highly charged ion (denominated with index 2) with charge q_i, mass m_i and oscillation frequencies ω_i. An external potential U_0 is applied, resulting in motional angular frequencies $\omega_i = \sqrt{2q_{\text{ion}}U_0/m_{\text{ion}}}$. The potential energy of this system becomes

$$E_{\text{pot}} = \frac{1}{2}m_1\omega_1^2 x_1^2 + \frac{1}{2}m_2\omega_2^2 x_2^2 + \frac{q_1 q_2}{4\pi\epsilon_0}\frac{1}{|x_1 - x_2|} \tag{2.49}$$

where x_i are the positions of the ions. The equilibrium distance d_0 for two ions at rest can be calculated, yielding

$$d_0 = \left(\frac{q_1 + q_2}{8\pi\epsilon_0 U_0}\right)^{\frac{1}{3}}. \tag{2.50}$$

Assuming a $^{9}Be^{1+}$ ion as LCI and a $^{208}Pb^{81+}$ ion as HCI in the trap with a U_0 chosen such that $\omega_1 = 2\pi \cdot 300\,\mathrm{kHz}$, the equilibrium distance d_0 is approximately 25 µm. However, the laser cooled ion can not be removed adiabatically[4]. This makes a new measurement scheme necessary.

Coulomb crystals could be used to measure g-factor differences in a Ramsey type measurement [31]. Spins are initialized in a well-defined state, e.g. both spins oriented along the magnetic field. Using a microwave $\pi/2$ pulse, the system is brought into a coherent state and each spin evolves with a frequency given by its Larmor frequency. The phase difference of both states with g-factors g_1 and g_2 is given by

$$\Delta\varphi(t) = \varphi_1(t) - \varphi_2(t) = \int_0^t \frac{g_1\mu_\mathrm{B}}{\hbar} B_1(t)dt - \int_0^t \frac{g_2\mu_\mathrm{B}}{\hbar} B_2(t)dt. \tag{2.51}$$

This equation assumes that the Zeeman shift is linear in B. After an evolution time, a second microwave pulse prepares the system for the readout of the spin orientation. Varying the evolution time allows to observe Ramsey fringes, from which the phase difference as a function of evolution time can be deduced under the assumption, that $B_1(t) = B_2(t)$. Coulomb crystallization keeps both ions at a stable, very small distance, decreasing the effect of spatial magnetic field variations. Coulomb crystallization is therefore an essential prerequisite for g-factor difference measurements.

For absolute g-factor measurements, LCI and HCI have to be stored in separate potential wells, making them adiabatically separable [31]. In this case the coupling strength via Coulomb interaction dramatically decreases for traditional cylindrical Penning traps. Microfabricated surface traps with typical equilibrium distances of 40 µm have been used [72] and allow to circumvent the problem of the weak coupling strength. On the other hand, these traps are not suitable for high-precision measurements requiring a good harmonicity of the potential over a large region in the trap. Common Electrode Coupling can be used to store ions in potential wells separated by a large distance.

2.4.2 Common Endcap Coupling

Common endcap coupling stores the LCI and the HCI in two different potential wells, rendering an adiabatic separation possible. The motion of one ion periodically induces image charges on a common grounded electrode, often but not necessarily an end cap. These image charges create an additional electric potential on the electrode and exert force on the other ion and vice versa. One can simplify the treatment by only allowing the motion on the symmetry axis and thereby reducing again the dimensionality of the system. The highly charged ion induces a voltage on the common electrode. This voltage can be

[4] When the LCI is removed from the trap by changing the shape of the electric potential, the HCI is heated [31]. Therefore high-precision g-factor measurements are only feasible on an ensemble of a laser cooled and highly charged ion, making the introduction of new measurement schemes necessary.

expanded as a power series of the position along the axis, yielding

$$U_{\mathrm{ind}}(x_1, x_2) = q_1 \sum_{k=1}^{\infty} C_k^{(1)} x_1^k q_1 \sum_{k=1}^{\infty} C_k^{(2)} x_2^k \approx q_1 C_1^{(1)} x_1 + q_2 C_1^{(2)} x_2. \tag{2.52}$$

Coefficients $C_k^{(i)}$ describe the capacity of the electrode and have dimensions $\mathrm{V\,m^{-k}}$. The force on the laser cooled ion using the effective electrode distance $D_{\mathrm{eff}}^{(i)}$ introduced in section 2.2.2 can be linearized for small motions with the force given by

$$F_1(x_1, x_2) = \frac{q_1}{D_{\mathrm{eff}}^{(1)}} U_{\mathrm{ind}}(x_1, x_2) = \frac{q_1^2 C_1^{(1)}}{D_{\mathrm{eff}}^{(1)}} x_1 + \frac{q_1 q_2 C_1^{(2)}}{D_{\mathrm{eff}}^{(1)}} x_2. \tag{2.53}$$

A similar equation can be written down for the HCI. The term proportional to x_1 causes a frequency shift, being one contribution to the image charge frequency shift, as discussed in section 2.2.6. The x_2-dependent term gives the interaction between the ions to first order. Using Newton's third principle, one receives a system of coupled equations of motion of the form

$$\ddot{x}_1 + \tilde{\omega}_1^2 x_1 = -\frac{q_1 q_2 C_1^{(2)}}{m_1 D_{\mathrm{eff}}^{(1)}} x_2 \tag{2.54}$$

$$\ddot{x}_2 + \tilde{\omega}_2^2 x_2 = -\frac{q_1 q_2 C_1^{(1)}}{m_2 D_{\mathrm{eff}}^{(2)}} x_1. \tag{2.55}$$

Here, the eigenfrequencies of a system without image charge contributions have been replaced by the perturbed eigenfrequencies $\tilde{\omega}_i$ accounting for the presence of the interaction between the ions. The coupling strength of this system under the condition $\tilde{\omega} = \tilde{\omega_1} = \tilde{\omega_2}$ using the rotating wave approximation is given by

$$\Omega = \frac{q_1 q_2}{2\tilde{\omega}} \frac{\sqrt{C_1^{(1)} C_1^{(2)}}}{\sqrt{m_1 m_2}\sqrt{D_{\mathrm{eff}}^{(1)} D_{\mathrm{eff}}^{(2)}}}. \tag{2.56}$$

By changing the well depths, the motional frequencies can be adjusted. The coupling between the ions shifts again their eigenfrequencies. Before a measurement, the HCI is cooled by common electrode coupling to a laser cooled ion. The coupling between the ions is removed by emptying the potential well used to store the LCI, such that a g-factor measurement on a cold HCI can be performed.

3 Laser Cooling at ALPHATRAP

3.1 The ALPHATRAP Setup

The ALPHATRAP setup consists of three main parts grouped by their functionality: At the heart of the experiment is the trap tower with the detection electronics attached. The trap is housed in a cryostat that is installed in the bore of a superconducting magnet. While the cryostat provides the cryogenic environment for trap tower and electronics, the superconducting magnet creates a magnetic field of roughly 4 T for trapping. The setup is completed by the offline beamline with its large variety of ion sources and allowing for injection of externally produced ions. An overview over the complete ALPHATRAP setup is shown in figure 3.1. The offline beamline and the trap system are described below, emphasizing the particularities affecting laser cooling.

3.1.1 Ion Production and Cryosystem

ALPHATRAP will in the future have a number of different sources for ion production. These sources are attached to the offline beamline, described in detail elsewhere [73]. A compact electron beam ion trap (EBIT), called table top EBIT (tt-EBIT), serves as ion source for low charge states. It is characterized by a magnetic field of 0.74 T, an electron current of up to 5 mA and a acceleration voltage of 1.5 kV. A segmented einzel lens with beam steering functionality and a Wien-type velocity filter serve for a rough beam purification. A pair of 90° electrostatic benders deflect the ions from the horizontal to the vertical part of the beamline. In the future the online beamline connecting the Heidelberg-EBIT will be attached at this point. The Heidelberg-EBIT will deliver the HCI for the measurement of g-factors in the high Z regime [74]. Additionally, a Laser Ion Source (LIS), currently under development, will be connected to the bender as well [75]. It delivers singly charged beryllium ions necessary for laser cooling by ablation from solid material using non-resonant laser ablation.

The vertical part consists of two different ion optics assemblies. The first set of electrodes can focus and steer the beam. A deceleration drift tube slows down ions extracted from the ion sources at energies of $2 - 5\,\mathrm{kV}/q_{\mathrm{ion}}$, as the capture section of the trap can be used only with voltages of up to 1 kV. The second ion optics assembly is used to focus the ions into the trap chamber. The whole beam line is at room temperature and is operated in the regime of ultra high vacuum. The detection units with a micro-channel plate detector and Faraday cup can be used for temporal and spatial beam monitoring. A cryogenic valve separates the beamline operated at room temperature from the cryogenic trap chamber improving the vacuum in the trap region [76].

The superconducting magnet (Oxford Instruments, Type 200 / 130) is charged to a magnetic field strength of approximately 4 T. Its bore has a diameter of 130 mm, is evacuated and houses the temperature shields of the nitrogen and helium cryostat. The nitrogen cryostat is cooled with liquid N_2 lowering the temperature of the temperature

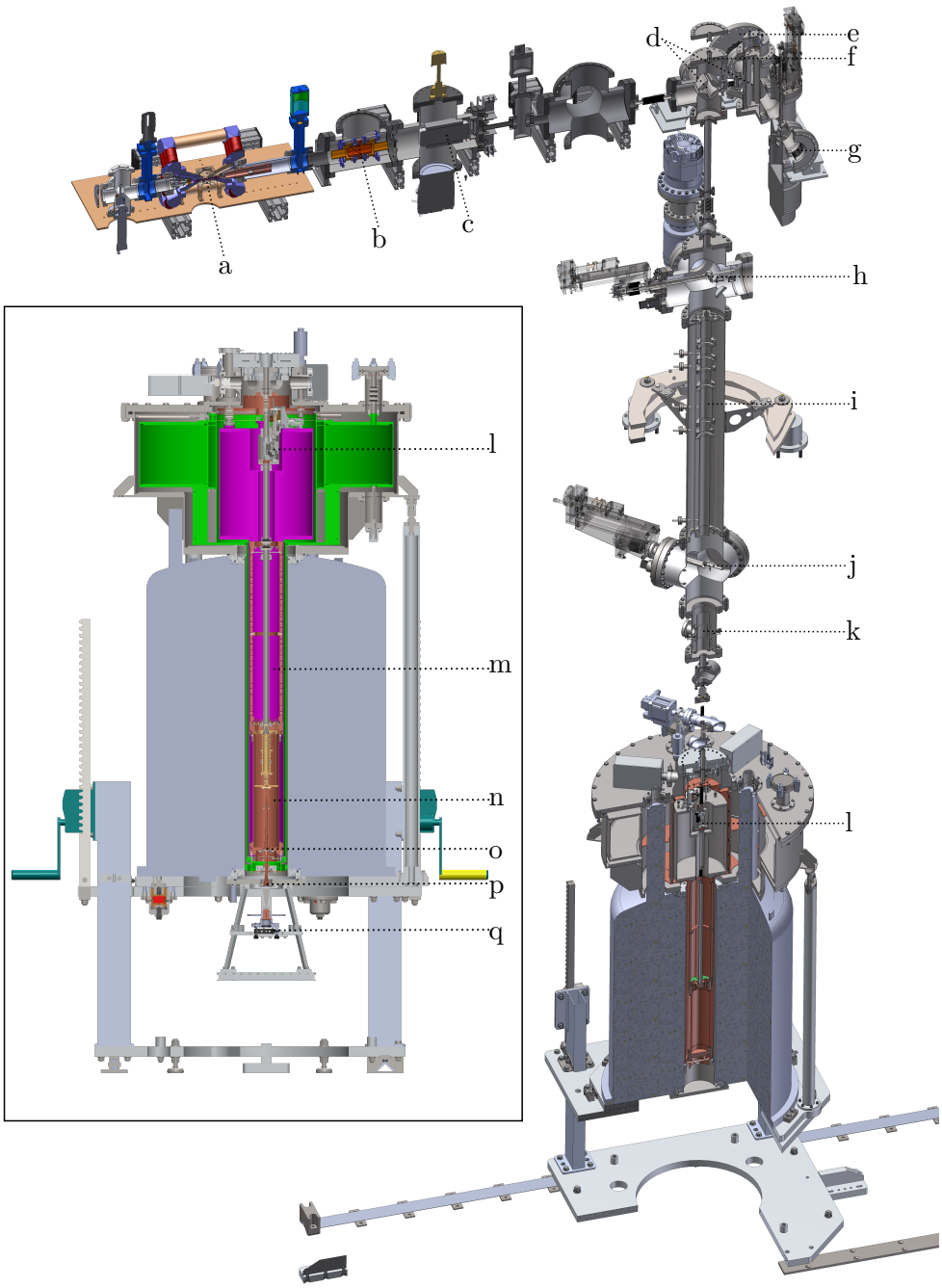

Figure 3.1: Overview over the ALPHATRAP setup. The offline beamline is formed by the tt-EBIT (a), a steering lens (b), a velocity filter (c), two electrostatic benders (d), diagnostic units (h,j), the first ion optics section (i), the second ion optics section (k) and a cryogenic valve (l). The laser ion source will be attached at (e) and the Heidelberg-EBIT will be connected to (g). In the inset, the magnet with the cryostat cooled with liquid N_2 (in green) and He (in purple) is shown. The electronics section housing the cryogenic part of the detection system (m, parts not shown), the trap chamber (n) and the mechanical adjustment for the microwave/laser system (q) can be seen. Optical access is guaranteed by the upper viewport(f), trap chamber viewport (o) and lower viewport (p).

shield connected to it to a value slightly above the nitrogen boiling temperature, isolating the trap chamber from the room temperature black body radiation. A second cryostat vessel filled with liquid helium is connected to the electronics section and the trap chamber, cooling them to a temperature slightly above 4.2 K. Ultra high vacuum in the trap chamber leading to very long storage times is guaranteed by the cryogenic conditions.

Access for ions, microwaves and laser light is given by the top and bottom end of the bore. Ions will be guided from the offline beamline via the top end of the bore into the trap chamber. During loading, the cryogenic valve is opened and stays closed otherwise to maintain good vacuum conditions in the trap chamber. In order to be able to keep the valve closed during laser cooling, the laser is intended to be coupled into the trap chamber together with the microwaves from the bottom through the lower viewport and the trap chamber viewport. A further point to consider is the length of the vertical beamline. It stretches from the benders to the upper end of the trap chamber over a length of approximately 4.03 m. This upper end is formed by a diaphragm (c.f. with figure 3.2) which is used as a Faraday cup for ion detection and has an inner diameter of 3 mm. Adding another 0.17 m for the distance between the bender and the upper viewport on top of the vertical beamline, the angle of a laser beam coupled in from above the magnet has to be stable better than $\pm\arctan(1.5\,\text{mm}/4200.8\,\text{mm}) \approx \pm 0.02°$. A laser beam coupled in from the bottom has to pass a diaphragm with a 0.95 mm diameter formed by the mode cleaner of the microwave system, which is installed 0.27 m away from the lower viewport. The angle for this solution has to stay within the range of $\pm 0.10°$, a five times larger allowance than for the incoupling from the top.

3.1.2 The Trap and the Detection System

The heart of the experiments is the trap tower consisting of the Precision Trap and Analysis Trap[1] shown in figure 3.2. The upper entrance to the trap tower is formed by a Faraday cup with a hole of 3 mm diameter. This diaphragm serves as pumping barrier between the trap chamber and the ion transport tube. It is electrically connected to a cryogenic charge amplifier in order to detect ions impinging on its surface. The lower end is used to couple laser light and microwaves into the trap. It is connected to a waveguide with a small diameter of 0.95 mm serving as mode cleaner. The microwaves are guided from the outside through the lower viewport, a waveguide section installed to the shield of the liquid nitrogen cryostat and the trap chamber viewport into the trap. Simulations have shown that the microwaves passing this guiding setup are not single-mode any more, making a mode cleaner in front of the trap necessary[2]. The laser beam with its much shorter wavelength is assumed to behave as in free space and its diameter has to be small enough to allow its spatial description be approximated by a Gaussian mode (c.f section 4.1.3).

The ions are extracted in bunches from the ion source, guided through the beamline to the drift tubes, decelerated and finally captured in the capture section of the trap tower. In order to minimize the transport losses due to angular spread of the ion beam, the transport energy between the drift tubes and the trap section should be chosen as high as possible, limited by the maximum operation voltage of the trap electrodes. The capture electrodes are designed to withstand up to 1 kV. The ions are subsequently cooled by means of evaporative cooling. A large number of thin electrodes allows to transport

[1] PhD thesis by Ioanna Arapoglou, in preparation
[2] Master thesis by Timo Steinsberger, in preparation

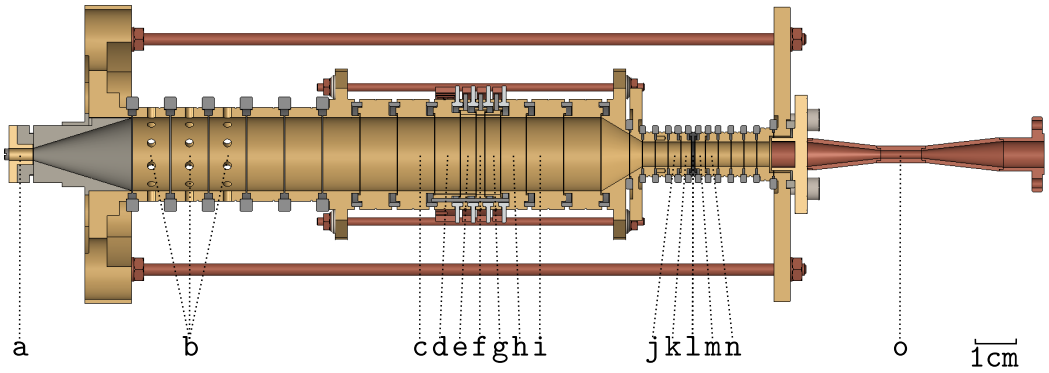

Figure 3.2: The trap tower. The Faraday Cup (a) is situated at the upper end. Capture electrodes (b) allow to capture and store ions with high voltages. The Precision Trap is formed of 7 electrodes: end caps (c,i), outer correction electrodes (d,h), inner correction electrodes (e,g) and ring electrode (f). The Analysis Trap consists of 5 electrodes: end caps (j,n), correction electrodes (k,m) and ring electrode (l) made out of ferromagnetic material. The microwaves and the laser light is guided into the trap by a waveguide with mode cleaner (o).

ions adiabatically between the capture section, the Precision Trap and the Analysis Trap. Currently the trap setup is in the commissioning stage. The microwave system is not installed and capturing ions from sources at the beamline is not yet implemented. An in-trap Electron Beam Ion Source is used to create carbon ions for trap commissioning [73].

The Analysis Trap consists of five electrodes, a pair of end caps and a pair of correction electrodes surround the ring electrode with an inner diameter of 6 mm. Important trap properties are given in table 3.1. The ring electrode is made out of a ferromagnetic cobalt iron alloy, which creates a magnetic bottle at the center of the trap. The magnetic field created by this configuration is shown in figure 2.7 (a), the z-component of the field strength along the trap axis is shown in 2.7 (b). The strong magnetic bottle is necessary for a reliable detection of the spin state even for highly charged ions. Considering equation (2.32), the frequency jump decreases for heavy ions. For a $^{208}Pb^{81+}$ ion at an axial frequency of 350 kHz it becomes 151 mHz. The shift induced by the standard deviation of the energy fluctuations should be at least a factor of 5 smaller than the shift of a spin jump in order to allow a reliable spin state detection. To meet this requirement, the standard deviation of the energy fluctuations of the cyclotron mode in accordance to equation (2.31) has to be smaller than 78 µeV, corresponding to a temperature of 0.90 K. This value could in principle be reached with direct electronic feedback cooling of the modified cyclotron mode. In the AT however, no cyclotron resonator is present, which is necessary for electronic feedback cooling of the cyclotron mode. Its cooling is realized by coupling to the axial mode. The temperatures of both modes are related by equation (2.47). Thus, a small temperature well beyond 14 µK is necessary in the axial mode for a reliable spin state detection, a value lying beyond the limits of electronic feedback cooling. The lower end cap is connected to a resonator, serving for axial cooling and frequency measurement. The electrode above the upper end cap is split into two halves, such that a quadrupolar drive

property	Analysis Trap	Precision Trap
electrodes	5	7
trap radius r_0	3 mm *	9 mm *
electrostatic field coefficient C_2	$-0.041\,63\,\mathrm{mm}^{-2}$ *	$-3.525 \times 10^{-3}\,\mathrm{mm}^{-2}$ *
typical tuning ratio U_C/U_0	0.8804	0.9642 * (inner)
		0.8156 * (outer)
magnetic field B_0	3.868 169 4(50) T	4 T *
magnetic bottle strength B_2	$45\,\mathrm{T\,mm}^{-2}$*	$\approx 0\,\mathrm{T\,mm}^{-2}$ $-0.041\,63\,\mathrm{mm}^{-2}$ *
axial resonator center frequency	350 kHz*	660 kHz*

Table 3.1: Summary of the properties of the Analysis Trap (AT) and Precision Trap (PT) used in the ALPHATRAP experiment. Values marked with an asterisk (*) are design values.

for coupling of the magnetron or modified cyclotron motion to the axial mode can be achieved.

The precision trap is formed of seven electrodes with a diameter of 18 mm. In this trap, the cyclotron frequency is measured and the spin flip is induced. The image charge shift scaling inversely to the third power of the trap diameter (c.f equation (2.39)) is reduced by the large dimensions. The seven electrode design with two sets of correction electrodes creates a potential with very small deviation from the ideal quadrupolar potential in the range of typical ion radii and amplitudes. A larger diameter also improves the harmonicity of the potential compared to smaller traps such as the AT. Two resonators are attached to the trap, configured for the measurement of the axial and the modified cyclotron motion. The ring electrode as well as the upper and lower correction electrodes are split into two halves. To the ring electrode, a dipolar drive can be applied acting on the radial eigenmotions. To the upper first correction electrode a quadrupolar drive can be applied to couple one of the radial modes to the axial mode. The lower first correction electrode is connected to the modified cyclotron resonator. The upper second correction electrode is split with a ratio of 1:3 such that a quadrupolar drive coupling magnetron and modified cyclotron motion can be applied. Lastly, the lower end cap electrode connects to the PT axial resonator for the axial frequency measurement and cooling. Both resonators allow for electronic feedback cooling of the corresponding mode. Important properties of the trap can be found in table 3.1.

The detection system[3] includes in its cryogenic part the resonators, amplifiers, filter stages and switches for the drive signals. It is complemented by amplifiers, downmixer, FFT analyzer and voltage sources exposed to room temperature. The resonators are superconducting in order to reach a high quality factor. While the axial resonators together with the trap attached are fixed at a center frequency of 660 kHz, the center frequency of

[3]PhD thesis by Andreas Weigel, in preparation

Ion	Transition	Wavelength	Charge-to-mass Ratio	Repumper	Reference
$^{9}Be^{1+}$	$^{2}S_{1/2} \leftrightarrow {}^{2}P_{3/2}$	313 nm	$\approx 0.111\, e\, u^{-1}$	no	[62]
$^{24}Mg^{1+}$	$^{2}S_{1/2} \leftrightarrow {}^{2}P_{3/2}$	280 nm	$\approx 0.042\, e\, u^{-1}$	no	[61]
$^{40}Ca^{1+}$	$^{2}S_{1/2} \leftrightarrow {}^{2}P_{1/2}$	397 nm	$\approx 0.025\, e\, u^{-1}$	yes	[63]

Table 3.2: Overview over ion species where laser cooling in Penning traps has been shown. The charge-to-mass ratio is given in units of the elementary charge over the atomic mass unit.

the modified cyclotron resonator can be tuned. The axial frequency can be chosen by the potential, bringing the ions motion into resonance with the tank circuit. The modified cyclotron frequency however is mainly determined by the strength of the magnetic field and essentially fixed. Using a varactor diode, the frequency of the modified cyclotron resonator can be tuned away from resonance. This additionally allows to observe ions of different masses without changes in the setup. Further details can be found in [77]. A separate cryogenic amplifier for each resonator picks up the signal and amplifies it. The signal is amplified a second time with a room temperature amplifier and mixed down using a single sideband mixer to analyze it on an FFT audio analyzer. The electrodes of the trap tower are supplied with filtered voltage. The end cap electrodes are grounded by the voltage source during normal operation.

Most Penning trap setups with laser cooling use fluorescence detection to find and stabilize the wavelength on the resonance of the electronic transition. Photodiodes are installed perpendicular to the cooling laser to collect light emitted by the fluorescent ions. At ALPHATRAP however, it is hard to include photodiodes into the trap setup. On one hand the efficiency of the light collection increases with the solid angle covered by them. On the other hand, electric field distortions created by the necessary holes in the electrodes are at odds with the aim of a high-precision measurement. The effect of laser cooling can be observed via the measurable temperature of the different modes. This measurement however requires a couple of minutes. For effective cooling, the laser system therefore has to be stabilized with an external system to the resonance wavelength. The lack of fluorescence feedback puts stringent requirements on the absolute accuracy and the stability. Below laser cooling with beryllium at the ALPHATRAP-experiment and its implications and requirements on the laser system and the wavelength stabilization are discussed.

3.2 Laser Cooling with Beryllium

For laser cooling, an ion with a closed electronic dipole transition in the optical range is necessary. If ions can decay to any other state, additional laser beams, so-called repumpers, are necessary to depopulate these states. Additionally, the lifetime of the upper state should be as short as possible such that scattering events happen frequently and the cooling effect is strong. Only for a few ions, laser cooling has been shown (c.f table 3.2). Magnesium and beryllium have the most suitable term structure, as, in contrast to calcium, no ^{2}D state

below the excited level exists, to which the electron can decay[4].

The ALPHATRAP experiment is aiming to sympathetically cool highly charged ions by trapping the LCI in a Penning trap. The handling of two different ion species in the trap becomes easier, the closer their charge-to-mass ratio is. This is especially important if both ions are stored in the same potential well. For $^{208}Pb^{81}$ this value becomes approximately $0.39\,e\,u^{-1}$ for $^{132}Xe^{53+}$ a value of $0.40\,e\,u^{-1}$ is found. The most suitable candidate for ALPHATRAP is therefore beryllium, as it has the largest charge-to-mass ratio, does not use a repumper as explained below and requires a wavelength that is accessible with narrowband laser systems.

3.2.1 Laser Cooling Transition

The magnetic field of the Penning trap shifts the different fine and hyperfine structure levels thereby complicating the situation compared to other trap types. Beryllium shows a fine structure splitting of the ^2P state with transition frequencies to the ground state given by 957.199 65(12) THz (313.197 416(39) nm in vacuum) for the $^2S_{1/2} \leftrightarrow {}^2P_{1/2}$ and 957.396 80(14) THz (313.132 922(45) nm in vacuum) for the $^2S_{1/2} \leftrightarrow {}^2P_{3/2}$ transition. The fine structure splitting of the excited state is 197.15(064) GHz [62]. A transition between the $^2S_{1/2}$ and the $^2P_{3/2}$ manifolds is used for laser cooling.

The lifetime of the excited states has been measured, yielding $\tau = 8.1(4)$ ns [57]. The natural linewidth Γ is given by the Fourier limit, the corresponding line shape is a Lorentzian with full width half maximum (FWHM) Γ [56]:

$$\Gamma = \frac{1}{\tau}. \tag{3.1}$$

It has a value of $2\pi \cdot 19.6(10)$ MHz for the natural linewidth of the laser cooling transition. The ^9Be isotope carries a nuclear spin with quantum number $I = 3/2$ [78].

The energy level shifts ΔE of the ground state in the magnetic field compared to the zero-field case are described by the Breit-Rabi formula. This analytic expression for the Zeeman effect in a state with electron spin quantum number $j = 1/2$ of an atom or ion with one valence electron including fine structure and hyperfine structure was derived by GREGORY BREIT and ISODOR RABI [79]:

$$\Delta E = \frac{A}{2(2I+1)} + g_I m_F \mu_n B + \frac{A}{2}\sqrt{1 - 4m_F\frac{(g_J\mu_b - g_I\mu_n)B}{A(2I+1)} + \left(\frac{(g_J\mu_b - g_I\mu_n)B}{A}\right)^2}. \tag{3.2}$$

Here, I is the absolute value of the nuclear spin $\mathbf{I}$ in units of $\hbar$, g_J and g_I are the g-factors of the electron and the nucleus respectively, A is the hyperfine structure constant and B is the applied external magnetic field strength. m_F is the z-component of the total angular momentum of the system with $\mathbf{F} = \mathbf{J} + \mathbf{I}$. The hyperfine structure constant was measured including a diamagnetic correction [80]. For a magnetic field of 4 T, a value of 1.250 017 674(44) GHz is obtained. The g-factors of the electron and the nucleus have been measured yielding values of $g_S = 2.002\,262\,06(42)$ and $g_I = -1.177\,432(3)\mu_N$ [12, 81].

[4] In beryllium (magnesium), no level between the $1s^2 2s$ ($2p^6 3s$) at 0 eV and $1s^2 2p$ ($2p^6 3p$) at 3.9 eV (4.4 eV) manifolds exist. The next energetically close state is the $1s^2 3s$ ($2p^6 4s$) state at 10.9 eV (8.7 eV). In calcium, the $3p^6 3d$ state at 1.7 eV lies between the $3p^6 4s$ and the $3p^6 4p$ manifold at 3.2 eV used for cooling [64].

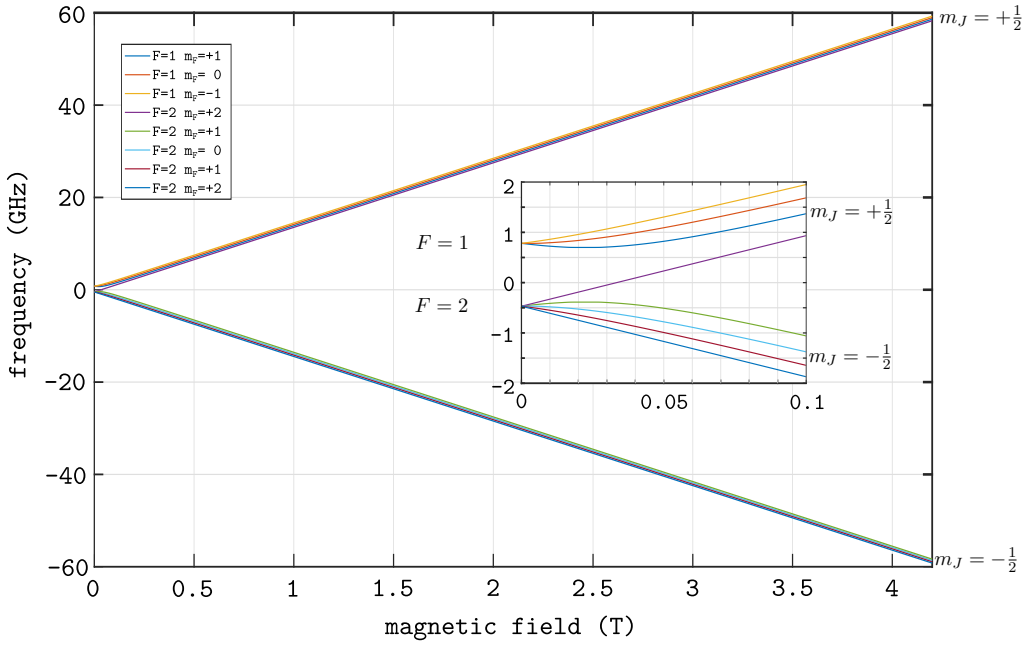

Figure 3.3: Term structure of the beryllium $^2S_{1/2}$ ground state with an external magnetic field applied. The inset shows the behaviour in the transition range between the anomalous Zeeman effect and the Paschen-Back regime of the hyperfine structure.

Being a state with orbital angular momentum zero, $g_J = g_S$ holds. The energy levels of the different hyperfine levels as a function of the external magnetic field are plotted in figure 3.3. A critical field strength estimate, where the anomalous Zeeman effect turns over into the hyperfine Paschen-Back effect can be defined as

$$B_{\text{crit}} = \frac{A}{\mu_B g_J}. \tag{3.3}$$

At this field strength, nuclear spin I and electron spin J start to decouple and F is not a good quantum number for the description of the system any more. For the ground state, it is 45 mT, such that for the ion in the magnetic field of 4 T a Paschen-Back effect of the hyperfine structure is observed. The transition regime is plotted in the inset of figure 3.3.

The upper level used for laser cooling is the $^2P_{3/2}$ manifold. The hyperfine splitting is significantly smaller than the natural linewidth of the laser cooling transition. Theoretical calculations have found a value of $A = 2.030(6)$ MHz [82]. The nuclear g-factor g_I is assumed to be identical for all electronic states.

For this level, no general analytic solution exists. By diagonalizing the Hamiltonian, one obtains the eigenenergies as a function of the magnetic field. The system is described in a basis of wave function characterized by quantum numbers J, m_J, I and m_I. The Hamiltonian of the coupling of nuclear and electron magnetic moment to the external

magnetic field describing the normal Zeeman shift is given by [56]

$$H_{\mathrm{Z}} = \left(g_J \mu_{\mathrm{B}} \hat{J}_z + g_I \mu_{\mathrm{N}} \hat{I}_z\right) B. \tag{3.4}$$

The Landé g-factor for a state with non-zero angular momentum can be found by first order perturbation theory, yielding [83]

$$g_J = g_L \frac{J(J+1) + L(L+1) - S(S+1)}{2J(J+1)} + g_S \frac{J(J+1) - L(L+1) + S(S+1)}{2J(J+1)}. \tag{3.5}$$

For beryllium with its single valence electron, $g_L = 1$ is useful. The resulting matrix for a specific basis contains only diagonal elements. The Hamiltonian of the hyperfine structure, describing the interaction between the nuclear magnetic moment and the electron magnetic moment, can be written as [56]

$$H_{\mathrm{HFS}} = A\, \hat{\mathbf{I}} \cdot \hat{\mathbf{J}} = A \left(\frac{1}{2}\hat{I}_+ \hat{J}_- + \frac{1}{2}\hat{I}_- \hat{J}_+ + \hat{I}_z \hat{J}_z\right). \tag{3.6}$$

Here, the angular momentum vector operators $\hat{\mathbf{I}}$ and $\hat{\mathbf{J}}$ have been rewritten in terms of the angular momentum raising and lowering operators $\hat{J}_+$ and $\hat{J}_-$. These operators have an eigenvalue equation [83]

$$\hat{J}_\pm \, |J\ m_J\rangle = \sqrt{J(J+1) - m_J(m_J \pm 1)}\ \ |J\ m_J \pm 1\rangle. \tag{3.7}$$

The matrix thus has off-diagonal elements. In matrix notation, it becomes

$$\begin{aligned}
&\langle\ J\ m_J\ I\ m_I | H_{\mathrm{Z}} + H_{\mathrm{HFS}} | J'\ m'_J\ I'\ m'_I\rangle = \\
&\left(\left(g_J \mu_{\mathrm{B}} m_J + g_I \mu_{\mathrm{N}} m_I\right) B + A m_J m'_J\right) \delta_{m_J m'_J} \delta_{m_I m'_I} \\
+&\frac{1}{2}\sqrt{J'(J'+1) - m'_J(m'_J - 1)}\sqrt{I'(I'+1) - m'_I(m'_I + 1)}\,\delta_{m_J m'_J - 1}\delta_{m_I m'_I + 1} \\
+&\frac{1}{2}\sqrt{J'(J'+1) - m'_J(m'_J + 1)}\sqrt{I'(I'+1) - m'_I(m'_I - 1)}\,\delta_{m_J m'_J + 1}\delta_{m_I m'_I - 1}.
\end{aligned} \tag{3.8}$$

From this matrix, the magnetic field dependent eigenenergies can be determined for each state by solving the eigenvalue problem. The resulting term structure of the $^2\mathrm{P}_{3/2}$ state is shown in figure 3.4.

The $^2\mathrm{P}_{1/2}$ state can again be described using the Breit-Rabi formula in equation (3.2). The fine structure constant is given by $A = 237.2(72)\,\mathrm{MHz}$ [62]. The Landé g-factor can be calculated using equation (3.5). The critical field strength is 25 mT. The levels are shown in figure 3.4.

From the solution, estimates of the transition wavelengths in a magnetic field of 4 T and 3.86 T as it can be found in the AT and PT of the ALPHATRAP experiment can be obtained. Numerical values for the shift of different states relevant for laser cooling are summarized in table 3.3. Error estimates for the ground and the $^2\mathrm{P}_{1/2}$ state can be calculated from the uncertainties of the constants used in equation (3.2). For the $^2\mathrm{P}_{3/2}$ state however, the system has been solved using numerical evaluation of the eigenvalue problem. For this reason, no uncertainty is specified. The values given should be understood as an estimate and serve as a starting point for finding the resonance. Additionally, the g-factor g_J in

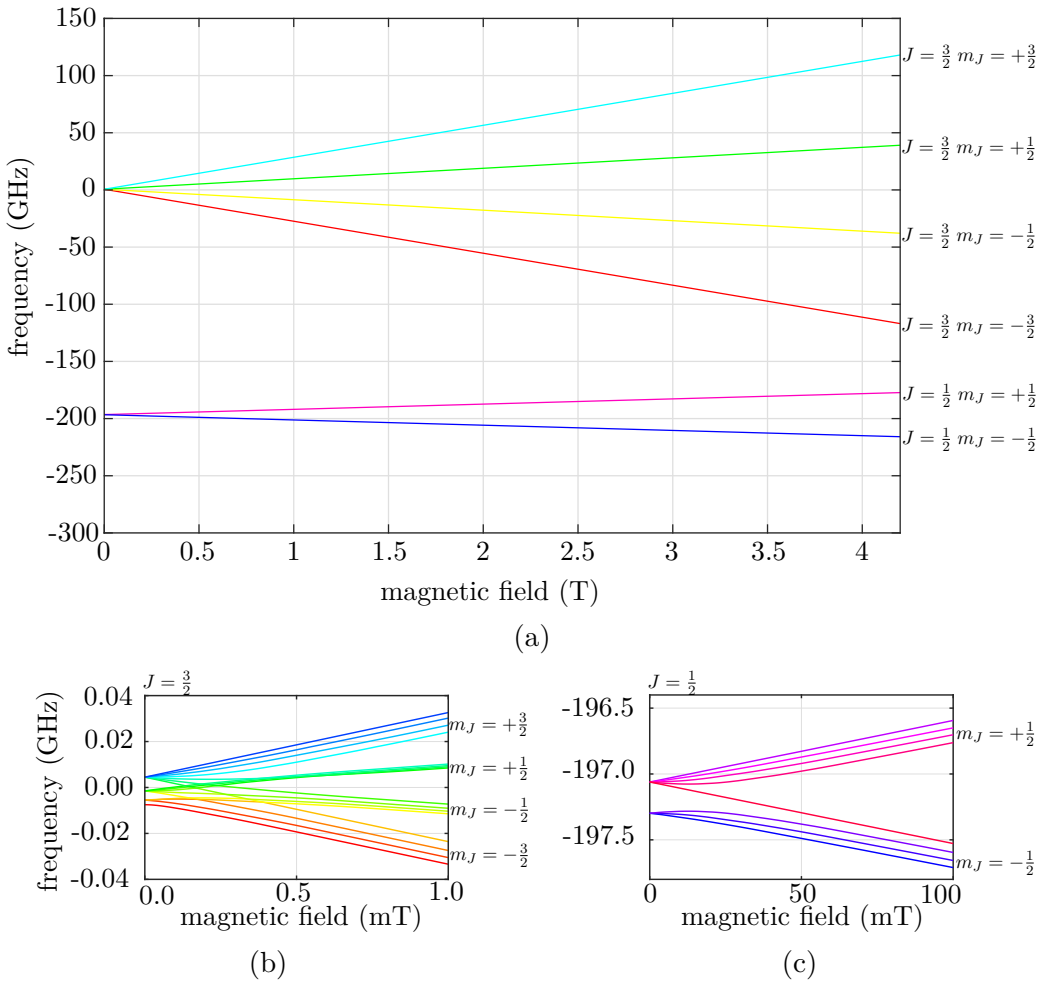

Figure 3.4: Term structure of the beryllium ^{2}P excited state in a strong magnetic field (a) and in the transition regime between F coupling and I-J coupling for the $^2P_{3/2}$ state (b) and for the $^2P_{1/2}$ state (c).

equation (3.5) used for the $^2P_{1/2}$ and $^2P_{3/2}$ states is obtained using first order perturbation theory.

The cooling transition should form a closed cycle where the electron in the excited state could only fall back to one Zeeman level of the $^2S_{1/2}$ ground state via an allowed (i.e. dipole) transition. This requirement is fulfilled by the $^2P_{3/2}$ $m_J = -3/2$ and $^2S_{1/2}$ $m_J = -1/2$ hyperfine multiplets, forming a σ^- transition. To drive this transition with a change in j quantum number of $\Delta m_j = -1$, laser light with circular polarization along the quantization axis given by the magnetic field is necessary. Equivalently, a closed cycle is also formed with the $^2S_{1/2}$ $m_J = +1/2$ level as ground state and the $^2P_{3/2}$ $m_J = 3/2$ level as excited state, forming a σ^+-transition driven by laser light with opposite circular polarization. With polarized laser light along the quantization axis, the electron is additionally pumped optically into a specific hyperfine level. All states with exception of the states with $I = 3/2$ and $I = -3/2$ contain admixtures of other states. For laser light with circular polarization

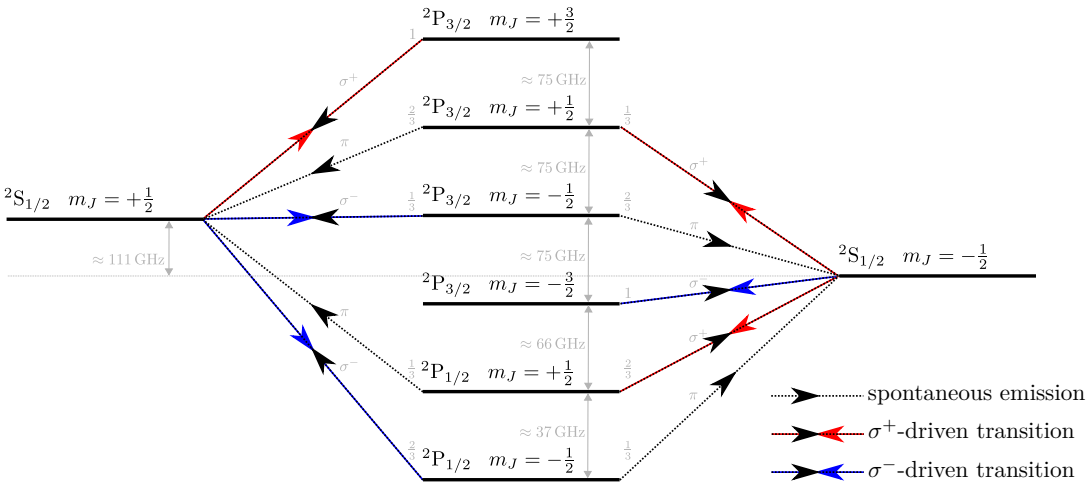

Figure 3.5: Laser cooling transitions in $^9Be^{1+}$. The Zeeman levels of the $^2S_{1/2}$ ground state are to the left and right of the levels of the ^2P excited state. Frequency spacing between the levels (at 4 T) and spontaneous emission decay probabilities as well as photon polarization are indicated.

driving σ^+ transitions optical pumping to the $I = 3/2$ states can be observed, for light driving σ^- transitions optical pumping to the $I = -3/2$ state occurs. A discussion for $^{24}Mg^{1+}$ with a similar term structure is given in [84]. Optical pumping of the fine structure states is discussed below.

Knowledge of absolute frequencies of the laser cooling transition is necessary to narrow down the range where the resonance is expected. This is particularly important at ALPHATRAP, as no fluorescent detection facilitates the search of the resonance. By adding the normal and anomalous Zeeman effect of the ground state and excited state to the relevant fine structure zero-field transition frequency, estimates of the frequency value in the PT and AT at ALPHATRAP can be calculated. Numerical values are given in table 3.3. The given error includes the error of the ground state, the excited state $^2P_{1/2}$ state and the zero-field transition frequency. With an error on the order of 100 MHz, the latter is the dominant contribution. For the Zeeman shift of the $^2P_{3/2}$ state, no uncertainties are available and do not contribute to the error budget. These transition values should be considered an estimate.

3.2.2 Darkstates

As discussed in the previous section, two transitions are suitable for laser cooling, driven by light along the quantization axis of circular polarization $\sigma^{\pm}$. Therefore, only transitions with quantum numbers $\Delta m_J = \pm 1/2$ can be driven. Hyperfine substructure is neglected as with polarized light optical pumping occurs. In the following discussion, the lower state of the two-level system is referred to as bright ground state while the other Zeeman level of $^2S_{1/2}$ is designated as dark ground state. Once the electron is in the dark ground state, the cooling effect stops. However, additional transitions can be off-resonantly driven

depopulating the dark ground state. In the case of a σ^+ cooling transition, an electron in the dark ground state $^2\mathrm{S}_{1/2}$ $m_J = -1/2$ is excited to the $^2\mathrm{P}_{1/2}$ $m_J = +1/2$ and the $^2\mathrm{P}_{3/2}$ $m_J = +1/2$ states. For a σ^- cooling transition, excitation to the $^2\mathrm{P}_{1/2}$ $m_J = -1/2$ and the $^2\mathrm{P}_{3/2}$ $m_J = -1/2$ states can occur. The electron decays from these two excited states to either Zeeman level of the ground state. The $^2\mathrm{P}_{3/2}$ $m_J = 1/2$ state for instance can decay emitting π and σ^- radiation. The transition probability $A_{m_{J,e},m_{J,g}}$ from a state with angular momentum z-component $m_{J,e}$ to a state with $m_{J,g}$ is proportional to the square of the corresponding Clebsch-Gordan coefficients $\langle J_\mathrm{g},\ m_{J,g},\ L_\mathrm{photon},\ m_{L,photon}|J_\mathrm{e},\ m_{J,e}\ \rangle$ [85]:

$$A_{\frac{1}{2},-\frac{1}{2}} \propto \ |\langle 3/2,\ 1/2,\ 1,\ -1|1/2,\ -1/2\rangle|^2 = \tfrac{2}{3} \qquad (\sigma^-\text{-polarization}) \tag{3.9}$$

$$A_{\frac{1}{2},\frac{1}{2}} \propto \ \ |\langle 3/2,\ 1/2,\ 1,\ 0|1/2,\ 1/2\rangle|^2 = \tfrac{1}{3} \qquad (\pi\text{-polarization}). \tag{3.10}$$

The slightly higher probability to decay to the bright ground state is a specific feature of beryllium and constitutes an intrinsic repumping mechanism. The same treatment applies to the $^2\mathrm{P}_{3/2}$ $m_J = -1/2$, $^2\mathrm{P}_{3/2}$ $m_J = +1/2$ and the $^2\mathrm{P}_{3/2}$ $m_J = -1/2$ states with different resulting probabilities. Laser driven transition for σ^+ and σ^- light and spontaneous emission decay channels with their corresponding probabilities are shown in figure 3.5.

For both circular polarizations of the cooling light, the nearby off-resonant transitions are driven depopulating the dark ground state, followed with a probability > 0.5 by a decay to the bright ground state. To estimate the time scale on which this process takes place, one considers the off-resonant scattering rate $R_\mathrm{scatt}(\delta)$ given by the scattering force (c.f. equation (2.42)) divided by $\hbar k$:

$$R_\mathrm{scatt}(\delta) = \frac{1}{2\tau}\frac{I/I_\mathrm{sat}}{1 + I/I_\mathrm{sat} + 4\delta^2\tau^2}. \tag{3.11}$$

For cooling using a σ^+-transition at saturation intensity, the $^2\mathrm{S}_{1/2}$ $m_J = -1/2 \leftrightarrow$ $^2\mathrm{P}_{3/2}$ $m_J = 1/2$ transition off-resonant by 35.18(20) GHz depopulates the dark ground state at a rate of 0.77 Hz. In the case of σ^--polarized light, the $^2\mathrm{S}_{1/2}$ $m_J = +1/2 \leftrightarrow$ $^2\mathrm{P}_{3/2}$ $m_J = -1/2$ transition off-resonant by 37.04(20) GHz is useful, resulting in a scattering rate of 0.69 Hz. σ^+ has a slightly higher transition rate, making it the prefereed candidate transition. As a result, the electron is transferred back to the bright ground state with a 66 % probability after 1.3 s and with a 96 % probability after 4 s. The transitions to the $^2\mathrm{P}_{1/2}$ states are further off-resonant with ≈ 180 GHz (σ^+) and ≈ 216 GHz (σ^-) resulting in scattering rates of 29 mHz and 20 mHz. They do not optically pump the dark ground state, but their contribution can be neglected. Depopulation occurs for instance, if a small amount of light of the opposite handness is present in the cooling laser beam.

Thus, laser cooling of singly charged beryllium ions in a Penning trap with a magnetic field of 4 T has an inherent re-pumping mechanism working on a seconds time scale. Typical heating rates expected for the cyclotron mode are on the order of phonons per second [31]. During this time, the electron is in the dark ground state and anomalous heating increases the radius of the cyclotron mode.

3.2.3 Dip Detection in Presence of Laser Cooling

The axial motion of an ion on resonance with the resonator tank circuit is driven by the electric field fluctuations induced by the temperature dependent Johnson-Nyquist noise. At the same time, the ion is damped via the energy dissipation of the image charge current through the resonator. In the absence of laser cooling, the ion creates a sharp dip on the resonator, as long as it is in thermal equilibrium with the electron gas in the tank circuit, as explained in section 2.2.2. If however laser cooling is present, an additional independent damping force acts on the ion, cooling it below the equilibrium temperature and thereby affecting its spectral filtering effect. The dip is expected to disappear for an ion cooled below the temperature of the electron gas in the resonator.

This effect has been simulated under conditions similar to the ones in the PT of the ALPHATRAP experiment. The simulation was simplified by replacing the tank circuit by a simple ohmic resistor at $T_{\mathrm{res}} = 4.2\,\mathrm{K}$ with a resistance of $R_{\mathrm{res}} = 75\,\mathrm{G\Omega}$ and by only considering the axial motion. The resistance value has been chosen higher than the real value of 370 MΩ of the ALPHATRAP PT. A $^9\mathrm{Be}^{1+}$ ion is simulated at axial frequency of $\nu_z = 300\,\mathrm{kHz}$ in a trap with trap parameter $D_{\mathrm{eff}} = 18.32 \times 10^{-3}\,\mathrm{m}$, corresponding to the trap diameter of the PT. The laser light was detuned by $\tilde{\delta} = -2.5\tau^{-1}$, where τ is the 8.1 ns lifetime of the upper state of the laser cooling transition with wave vector $k = 2\pi/313\,\mathrm{nm}$.

The simulation has been performed for different laser light intensities using the numerical software package MATLAB. Random numbers n_R have been created using the built-in function giving random samples of a normal distribution with unity variance. The Johnson-Nyquist noise used for simulation has been calculated using the relation

$$U_{\mathrm{noise}}(t) = \sqrt{4k_B T_{\mathrm{res}} R_{\mathrm{res}} \Delta f} \cdot n_R. \tag{3.12}$$

The bandwidth was chosen such that $\Delta f = 2 \cdot \#samples/T$, where $\#samples$ denotes the number of discrete time steps and T the overall integration time. The equation of motion to be integrated becomes

$$\ddot{z}(t) = -(2\pi\nu_z)^2 z(t) - \frac{U_{\mathrm{noise}}(t) q_{\mathrm{ion}}}{m_{\mathrm{ion}} D_{\mathrm{eff}}} - \frac{R_{\mathrm{res}} q_{\mathrm{ion}}^2}{m_{\mathrm{ion}} D_{\mathrm{eff}}^2} \dot{z}(t) - \hbar k \frac{1}{2\tau} \frac{I/I_{\mathrm{sat}}}{1 + I/I_{\mathrm{sat}} + \mathbf{4}(\dot{z}(t)k + \tilde{\delta})^2 \tau^2}. \tag{3.13}$$

The first term on the right hand side describes the action of the harmonic potential, the second gives the excitation due to noise on the electrodes and the third represents the damping due to the image current in the resonator. The fourth term describes the effect of laser cooling on the axial motion of the ion and compares to equation (2.42).

Results for three different saturation intensities are shown in figure 3.6. One can observe that the peak starts to vanish with increasing intensity. For the situation in the PT, a much stronger effect is expected. Here, a coupling to the resonator approximately 200 times stronger compared to the situation in the real trap was simulated, as can be seen from the cooling time constant in equation (2.22). As a consequence, the disappearance of the dip is expected at much smaller intensities of the laser light in the real trap.

This effect can be used to find the resonant wavelength for laser cooling, as it is much less time consuming compared to a full temperature measurement. While for a reasonable temperature measurement, many dip spectra have to be taken, each single one requiring a measurement time of approximately 1 min, this method requires only the measurement of one spectrum. Additionally it can be used in the PT without modification of the trap

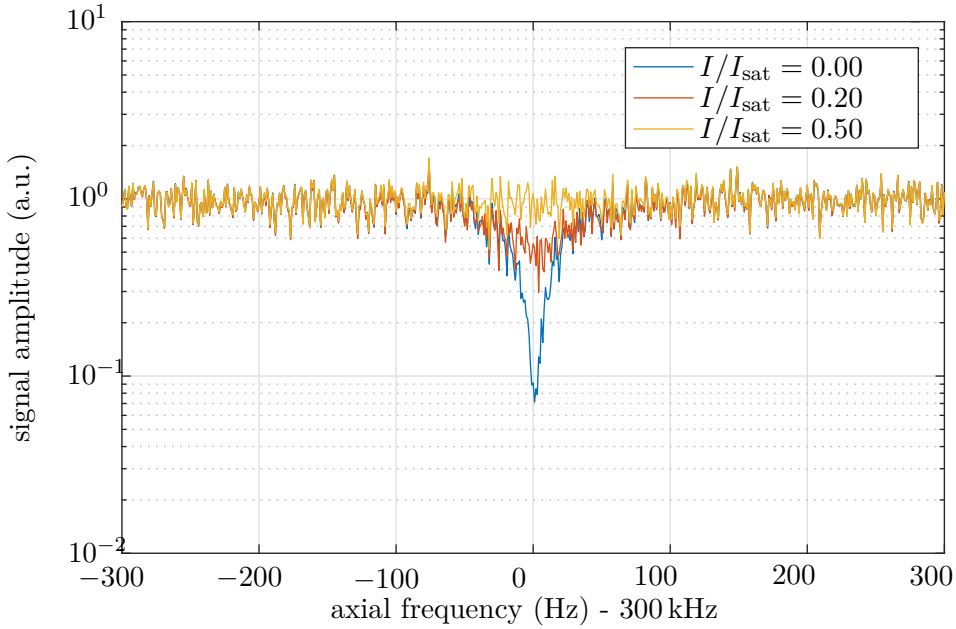

Figure 3.6: Simulation of the dip detection in presence of laser cooling. The ion motion was simulated for three different saturation intensities and with a bin width of 0.1 Hz in the obtained spectrum. For details, see text.

potential. However, this method cannot deliver quantitative information on the achieved temperature of the ion. For a full temperature measurement in the PT in absence of a magnetic bottle with energy dependent frequency shift, the trap potential can be made on purpose anharmonic such that the C_4 shift in equation (2.36) introduces an energy dependent shift.

3.3 The Cooling Laser System

The laser system has to fulfill certain requirements in terms of wavelength and its temporal stability. The strong magnetic field in the magnet shifts the energy level as a function of the magnetic field. A broad tuning range of the laser is therefore advantageous to be able to cover all fine and hyperfine transitions. Compared to other experiments using laser cooled beryllium, ALPHATRAP will not have a fluorescent detection making it necessary to measure the wavelength with high accuracy. Based on the measurement result, a regulation loop locks the laser to the desired frequency. However, if the laser drifts on timescales below the regulation loop interval, heating of the ion can occur, eventually limiting the lowest achievable temperature. For cooling to the Doppler limit, a detuning of $\delta_B = \Gamma/2$ is necessary. For a detuning $\delta_B < \Gamma/2$ however, more blue detuned than red detuned photons are absorbed, leading to a net heating effect. Drifts of the laser frequency below the regulation interval can be characterized by a linewidth measured with an integration time comparable to this regulation time scale. In practice, a detuning slightly above the ideal value $\delta_B > \Gamma/2$ is chosen. From these experiment specific constraints, requirements

on the laser system can be identified. The following specifications have been set to evaluate different proposals for light generation at 313 nm:

- The wavelength should be tunable in the range 313 nm ± 1 nm. This covers all transitions between the S and P states in the magnetic field of ALPHATRAP.
- The spectral linewidth should be lower than 100 kHz measured with an integration time of 5 µs and lower than 2 MHz measured with an integration time of 100 ms. Both values ar significantly lower than the natural linewidth of $^{9}Be^{+}$, such that heating of the ion due to drifts in laser frequency even for a detuning close to the Doppler limit is avoided.
- The wavelength should be stabilized to a fixed value with an absolute accuracy of better than 4 MHz. The accurate knowledge of the laser frequency compensates the lack of fluorescence detection during normal operation.

The system used at ALPHATRAP is a fully commercial "TA FHG pro" laser system manufactured by Toptica Photonics AG [86]. It consists of a External Cavity Diode laser (ECDL) emitting in the infrared at 1252 nm and a Tapered Amplifier (TA). Subsequently the light is fed into a series of two cavities with a non-linear medium, each doubling the frequency of the input light. The cavities are called Second Harmonic Generation (SHG) and Fourth Harmonic Generation (FHG), corresponding to the multiples of the fundamental wavelength emitted by the diode. The system is completed by a wavelength meter with regulation loop for wavelength stabilization and a wavelength reference. The system is shown in figure 3.7. The details of the individual constituents are discussed in the sections below.

3.3.1 The Cooling Laser

The fundamental light is emitted by an External Cavity Diode Laser. An optical resonator is formed by the amplifying semiconductor laser diode with an high reflectivity surface forming a mirror and an external grating which can by adjusted in angle for wavelength selection. The other end of the semiconductor material is anti-reflection coated to avoid undesired resonances. A lens in between adjusts the numerical aperture of the light coming out of the semiconductor laser diode. This is the so-called Littrow configuration of an ECDL. The extended length of the resonator compared to solitary semiconductor diodes as well as the small bandwidth of the resonator imposed by the grating help to reduce the linewidth [87]. The linewidth of the 313 nm light originates from frequency fluctuations in the laser diode. The intrinsic noise of an ECDL is estimated to be on the order of a few tens of kilohertz [88]. To this intrinsic noise due to quantum processes as stimulated emission and optical losses in the cavity, technical noise adds. This technical noise is induced by fluctuations in the diode current and diode temperature as well as by mechanical vibrations [89]. A piezo is used to adjust the resonator length, which is useful when stabilizing the wavelength.

This specific laser diode has a typical output power of 85 mW. For the conversion in a non-linear crystal, higher intensities are necessary. The light passes an optical isolator to protect the ECDL and is fed into a Tapered Amplifier. The TA consists of an anti-reflection coated semiconductor material acting as gain medium. The light is amplified by stimulated emission during its transit, conserving its time-spectral characteristics. With a current of

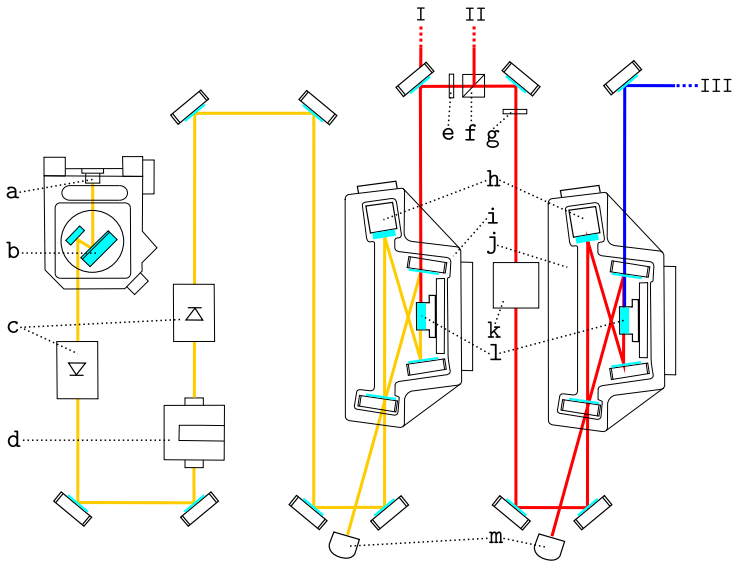

Figure 3.7: Overview over the laser system. The laser diode (a) with the external grating (b), the Tapered Amplifier (d), the SHG cavity (i) and FHG cavity (j) are shown. Optical isolators (c) prevent damage from reflected light. A polarizing beam splitter (f) in conjunction with an adjustable (e) and fixed (g) $\lambda/2$-plate allows outcoupling of light at 626 nm. Cavities contain a non-linear crystal (l) and piezos for length adjustment (h). For the cavity lock, external photodiodes (m) are used. The signal is modulated by the diode (a) and an electro optical modulator (k). Adapted from [86].

5.2 A applied to the semiconductor, a typical output power of 1.8 W is observed at typical ECDL power.

Frequency conversion to 626 nm and then subsequently to 313 nm takes place in two second harmonic generating cavities. A non-linear crystal in the beam waist of the cavity doubles the frequency. This light is coupled out via a dichroic cavity mirror. The crystal is temperature-stabilized, a stack of piezo elements behind one of the mirrors allows to adjust the cavity length. To obtain the highest possible intra cavity power, making the conversion process more efficient, the cavity has to be on resonance with the wavelength of the in-coupled light. A Pound-Drever-Hall lock is used to electronically stabilize the effective cavity length on resonance [90]. For this technique, the laser light of the ECDL is modulated such that at the entrance of the cavity, sidebands can be observed. The modulated light is partially reflected at the incoupling mirror onto a photodiode (c.f figure 3.7 (m)) and brought into interference with the light leaking from the cavity. The envelope of the beat note as a function of the cavity length is measured. This signal is an antisymmetric function with a zero crossing at the cavity length that matches a multiple of the wavelength. A regulation loop locked to this zero crossing is used to stabilize the length on resonance. The modulation at the input of the FHG cavity is obtained using an electro-optical modulator. Energy conservation of the non-linear process

is fulfilled by the relation of the frequencies of the incoming and outgoing photons given by $2 \cdot \nu_{\text{in}} = \nu_{\text{out}}$. To guarantee momentum conservation, phase matching of the linear crystal is necessary. The nonlinear crystal is birefringent, its refractive index $n(\nu, \varphi)$ depends on the frequency and the angle φ of incidence with respect to the fast axis. The condition for the second harmonic generating process to take place written in terms of wave vectors becomes $\mathbf{k}_{\text{out}} = n(2\nu_{\text{in}}, \varphi)\hat{\mathbf{e}}_{\text{out}}/c = 2 \cdot \mathbf{k}_{\text{in}} = 2 \cdot n(\nu_{\text{in}}, \varphi)\hat{\mathbf{e}}_{\text{in}}/c$. It is achieved by adjusting the temperature and the angle of the crystal. The SHG cavity typically creates 800 mW of output power. This light is converted to typical values of 300 mW in the FHG cavity. The efficiency of the conversion process decreases with smaller input power from typically $\approx 44\,\%$ in the SHG to $\approx 38\,\%$ in the FHG.

For future extensions, outcoupling of 626 nm-light is available. A rotatable half-wave plate is used to couple out an adjustable amount of light through a polarizing beam splitter. A second fixed half-wave plate turns the polarization back. The light can be shifted in frequency and then frequency doubled in another cavity. This could be used for instance for a probe laser beam for spectroscopy on the LCI, a repumper or for a second cooling beam for Raman cooling.

3.3.2 Wavelength Stabilization

For wavelength stabilization, a wavelength meter WSU-2 manufactured by HighFinesse is used. The necessary absolute calibration of this device is provided by a helium-neon laser system LJSC-3-11 manufactured by Lasertex and stabilized to an iodine transition.

The wavelength meter uses a set of Fizeau-type interferometers and a CCD array to record the interference patterns. It is specified to have an accuracy of better than 2 MHz and a resolution of 500 kHz. The measurement sampling rate depends on the exposure time of the CCD and has an upper limit of 150 Hz. A software based Proportional-Integral-Derivative controller (PID) with adjustable parameters is included into the wavelength meter. The output signal is converted to an analog voltage and used to adjust the laser frequency via the ECDL piezo.

Environmental variables slightly change the interferometric behavior and, without correction, limit the achievable accuracy. Although the wavelength meter is equipped with temperature and pressure sensors correcting for shifts, it is necessary to recalibrate the wavelength meter regularly to ensure accuracy. The 2 MHz accuracy requires in conformity with the manufacturer's specifications a recalibration at least every 2 min. The reference frequency is delivered by the helium-neon laser system. It features a relative frequency stability of $\delta\nu/\nu = 1 \cdot 10^{-11}$ over an averaging period of 1 s and a frequency uncertainty smaller than 12 kHz. The absolute accuracy is achieved by an intra-cavity iodine spectroscopy. The wavelength is locked to a hyperfine component of the R(127) 11-5 transition, accepted as a frequency standard [5].

3.3.3 Optical Fibers

The laser system will be installed in a dedicated room next to the ALPHATRAP laboratory where the magnet with the trap system is installed. The laser light has to be guided from the table in the laser room to the support frame of the magnet over a distance of roughly

[5] The hyperfine component "f" of the R(127) 11-5 transition is recognised as a realization of the meter by the Bureau International des Poids et Mesures [91].

4 m. To avoid instability of the laser beam due to relative vibrations and motion between the laser table and the magnet support frame, an optical fiber should be used to transport the 313 nm light to the incoupling mechanism installed under the magnet (c.f. figure 3.1 (q)).

Difficulties with the fiber transport arise from the short wavelength. Fibers are typically manufactured from doped fused silica glass, which tends to form chemical defects absorbing and scattering radiation, so-called color centers, when exposed to ultraviolet radiation [92]. Two approaches help to circumvent this problem: The degrading of the fiber due to the formation of color centers is proportional to the intensity of the radiation. Enlarging the mode field area reduces the intensity. Increasing the concentration of hydrogen in the glass and subsequent irradiation with ultraviolet light alters the defects in the material and prevents future formation of further color centers.

Classical step-index fibers are characterized by the dimensionless fiber parameter V with

$$V = 2\pi \frac{a}{\lambda} \sqrt{n_{\text{core}}^2 - n_{\text{cladding}}^2}, \tag{3.14}$$

where λ is the wavelength, a the radius of the fiber core and n the refractive indices of the core and the cladding. The numerical aperture of the fiber is given by $NA = (n_{\text{core}}^2 - n_{\text{cladding}}^2)^{1/2}$. [93]. Depending on the core diameter, the guidance can either be single or multi mode. Single-mode operation is given under the condition $V < 2.405$. Fibers with a larger V allow more than one mode to propagate. The number of modes M supported by the fiber under the assumption $V \gg 1$ can be approximated as [93]

$$M \approx \frac{4V^2}{\pi^2}. \tag{3.15}$$

Typical multimode fibers supporting ultraviolet light have a core diameter larger than 50 µm and a numerical aperture larger than 0.22. Using equation (3.15), fibers with these characteristics support more than 1×10^4 different modes. Coupling between these modes and thereby guidance efficiency of the fundamental mode is highly sensitive to environmental conditions, especially to strain. Single-mode guidance of the fiber is for a reliable operation desirable. This requirement conflicts with the necessity of a large mode field radius in step index fibers reducing the degrading of the fiber due to solarization.

To circumvent this difficulty, Photonic Crystal Fibers (PCF) are used. The fiber consists of a structure of small air holes forming a regular crystal-like pattern. An effective index created by this structure replaces the change in refractive index in step-index fibers. The material and structure is chosen in a way that the numerical aperture becomes proportional to the wavelength $NA = (n_{\text{core,eff}}^2 - n_{\text{cladding,eff}}^2)^{1/2} \propto \lambda$. As a consequence the fiber parameter V is independent of λ. With appropriately chosen parameters, the fiber can be used in single-mode operation over a broad range of wavelengths, a property called endless single-mode guidance.

PCFs have been shown to withstand continuous-wave radiation at 313 nm over a long time [92, 94]. However, these fibers have been chemically modified before to prevent an excessive formation of color-centers. This was achieved by putting them for several days into an H_2 environment at a pressure of around 100 bar. Subsequently, the fiber is exposed to ultraviolet light, a process denominated as curing. The color-centers formed during this process react with the hydrogen in the fiber to form structures that are either optically

inactive or interact at different wavelengths [94]. Successful operation of a PCF with a different type of structure without prior hydrogen loading at 218 nm over several days has been reported [95].

Tests of hydrogen loaded photonic crystal fiber are currently in progress [6]. A LMA-10-PM PCF manufactured by NKT Photonics A/S is used. If the attenuation of $0.13(4)\,\mathrm{dB\,m^{-1}}$ and incoupling efficiency of 70 % from reference [94] are assumed, a total transmission efficiency of 66.4 % is obtained for a 4 m fiber. However, reported results have only been measured with fiber lengths of up to 2 m.

3.3.4 Integration in the Setup

Without fluorescence detection, only minimal modifications to the current ALPHATRAP setup are necessary to implement laser cooling. The laser light is coupled into the trap from the bottom of the setup together with the microwaves. The window of the viewport in the trap chamber and the outer isolation vacuum have to be transparent for microwaves around 100 GHz and for ultraviolet light at 957 THz corresponding in vacuum to a wavelength of 313 nm. This viewport is slightly tilted with respect to the laser beam to prevent the built-up of resonances. The light will exit the fiber through a fiber collimator with integrated lens and pass a telescope to adjust the beam size. A microwave directional coupler will be used to align the microwaves with the laser light in the same waveguide. An adjustable mount allows to align laser and microwaves with the trap axis[7].

[6] PhD thesis by Alexander Egl and PhD thesis by Matthew Bohman, both in preparation
[7] PhD thesis by Alexander Egl, Master thesis by Timo Steinsberger, both in preparation

	level(s)	$B = 3.86\,\mathrm{T}$ (AT)	$B = 4\,\mathrm{T}$ (PT)
Zeeman and HFS	$^2\mathrm{S}_{1/2}\ m_J = +\frac{1}{2}\ m_I = +\frac{3}{2}$	53.583 30(14) GHz	55.543 73(14) GHz
	$^2\mathrm{S}_{1/2}\ m_J = +\frac{1}{2}\ m_I = -\frac{3}{2}$	54.592 61(14) GHz	56.555 46(14) GHz
	$^2\mathrm{S}_{1/2}\ m_J = -\frac{1}{2}\ m_I = +\frac{3}{2}$	−53.655 13(14) GHz	−55.617 98(14) GHz
	$^2\mathrm{S}_{1/2}\ m_J = -\frac{1}{2}\ m_I = -\frac{3}{2}$	−54.520 81(14) GHz	−56.481 25(14) GHz
	$^2\mathrm{P}_{1/2}\ m_J = +\frac{1}{2}\ m_I = +\frac{3}{2}$	17.8646(28) GHz	18.5158(28) GHz
	$^2\mathrm{P}_{1/2}\ m_J = -\frac{1}{2}\ m_I = -\frac{3}{2}$	−18.0425(28) GHz	−18.6937(28) GHz
	$^2\mathrm{P}_{3/2}\ m_J = +\frac{3}{2}\ m_I = +\frac{3}{2}$	108.082 GHz	112.002 GHz
	$^2\mathrm{P}_{3/2}\ m_J = +\frac{1}{2}\ m_I = +\frac{3}{2}$	36.026 GHz	37.310 GHz
	$^2\mathrm{P}_{3/2}\ m_J = -\frac{1}{2}\ m_I = -\frac{3}{2}$	−36.001 GHz	−37.307 GHz
	$^2\mathrm{P}_{3/2}\ m_J = -\frac{3}{2}\ m_I = -\frac{3}{2}$	−108.073 GHz	−111.993 GHz
transition (σ^+ polarization)	$^2\mathrm{S}_{\frac{1}{2}}\ m_J = +\frac{1}{2}\ m_I = +\frac{3}{2} \leftrightarrow {}^2\mathrm{P}_{3/2}\ m_J = +\frac{3}{2}\ m_I = +\frac{3}{2}$	957.451 30(14) THz	957.453 26(14) THz
	$^2\mathrm{S}_{\frac{1}{2}}\ m_J = -\frac{1}{2}\ m_I = +\frac{3}{2} \leftrightarrow {}^2\mathrm{P}_{3/2}\ m_J = +\frac{1}{2}\ m_I = +\frac{3}{2}$	957.486 48(14) THz	957.489 73(14) THz
	$^2\mathrm{S}_{\frac{1}{2}}\ m_J = -\frac{1}{2}\ m_I = +\frac{3}{2} \leftrightarrow {}^2\mathrm{P}_{1/2}\ m_J = +\frac{1}{2}\ m_I = +\frac{3}{2}$	957.271 17(16) THz	957.273 78(16) THz
transition (σ^- polarization)	$^2\mathrm{S}_{\frac{1}{2}}\ m_J = -\frac{1}{2}\ m_I = -\frac{3}{2} \leftrightarrow {}^2\mathrm{P}_{3/2}\ m_J = -\frac{3}{2}\ m_I = -\frac{3}{2}$	957.343 25(14) THz	957.341 29(14) THz
	$^2\mathrm{S}_{\frac{1}{2}}\ m_J = +\frac{1}{2}\ m_I = -\frac{3}{2} \leftrightarrow {}^2\mathrm{P}_{3/2}\ m_J = -\frac{1}{2}\ m_I = -\frac{3}{2}$	957.306 21(14) THz	957.302 94(14) THz
	$^2\mathrm{S}_{\frac{1}{2}}\ m_J = +\frac{1}{2}\ m_I = -\frac{3}{2} \leftrightarrow {}^2\mathrm{P}_{1/2}\ m_J = -\frac{1}{2}\ m_I = -\frac{3}{2}$	957.127 01(16) THz	957.124 40(16) THz

Table 3.3: Summary of Zeeman shifts and transition frequencies in $^9\mathrm{Be}^+$ driven during laser cooling. For details, see text.

4 Characterization of the Cooling Laser System

The purpose of the measurements presented in this chapter is twofold: Firstly, the temporal and frequency characteristics of the laser beam and its stabilization have been investigated. The obtained quantities allow to make a prediction whether efficient laser cooling with the chosen laser system will be possible at all. Secondly, the spatial characteristics of the beam have been measured. These parameters allow to optimize the integration of the cooling laser into the ALPHATRAP setup.

4.1 Cooling Laser

The laser light can be characterized by its frequency, peak field amplitude and spatial distribution. Those parameters are subjected to changes over time. On short timescales, power and spatial characteristics are assumed to be constant. The frequency fluctuations, determining the frequency stability on a certain timescale, are characterized by a linewidth. Results for this quantity are presented in section 4.1.1. On long timescales, from seconds to hours, the frequency is assumed to be stable as an active regulation of the wavelength is used. Power however varies with external environmental parameters, such as temperature and pressure. Measurement of this influence are presented in section 4.1.2. The spatial characteristics are assumed to be constant even on long timescales. The results of the beam profile measurements are discussed in section 4.1.3.

4.1.1 Linewidth

Linewidth measurements have been performed on two different timescales, with an integration time of roughly 3.2 µs and on a longer timescale with an integration time of 100 ms. These measurements require two different techniques. For the short integration time, a self-heterodyne setup was used, necessitating only one source of light. A heterodyne measurement scheme using the light from two spectral-wise similar laser systems provides an upper limit estimate of the linewidth for a long integration time. The linewidth shape is determined by the spectrum of the frequency noise-creating underlying process. A linewidth includes all fluctuations on timescales smaller than the integration time, with which the measurement was performed. All changes on timescales longer than the integration time become visible as drifts.

Spontaneous emission in the gain medium creates random phase fluctuations modeled by a Gaussian process and thus creating a Lorentzian line shape. The width of this line shape can be estimated using the well-known formula by SCHAWLOW and TOWNES [96]. The intrinsic line shape of diode lasers however is dominated by relaxation oscillation of carrier density, influencing the refractive index of the gain medium [97]. Electronic noise

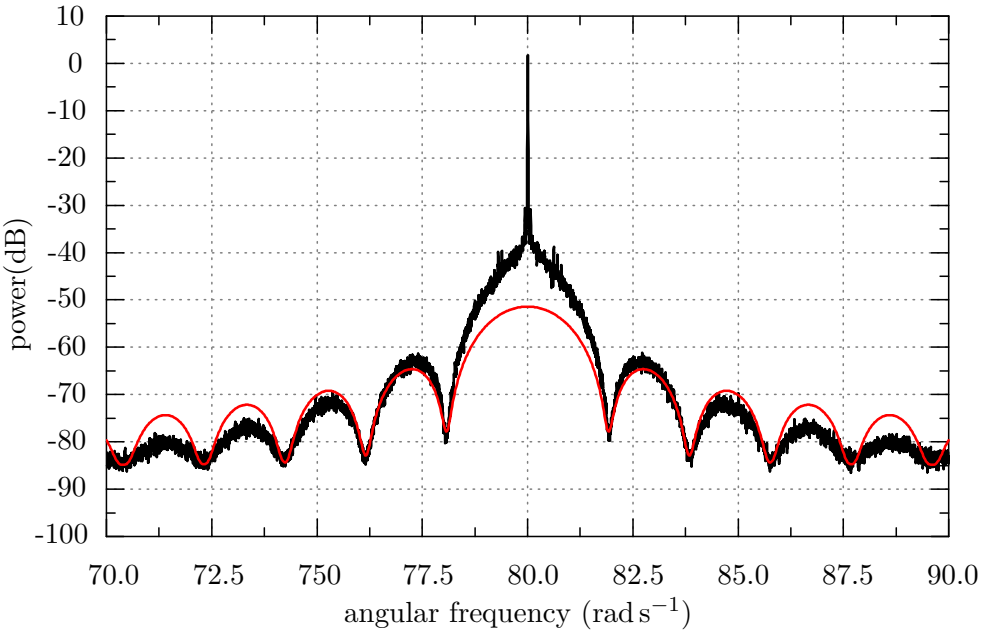

Figure 4.1: Self-heterodyne measurement of the laser linewidth. The data is shown in black on a logarithmic scale with arbitrary units. A fit to the data is drawn in red. For details, see text.

and change in environmental parameters as well as intensity fluctuations influence the noise spectrum of laser diodes [98].

Two main types of phase noise can be observed. White noise with spectral density $S(\nu) \propto 1$ is dominant for high frequencies, while flicker noise $S(\nu) \propto \nu^{-1}$ becomes dominant for frequencies below 100 kHz [99]. White noise creates a Lorentzian line shape if the measurement bandwidth is not limited [100]. For flicker noise, a Gaussian line shape with a strong dependence on the integration time can be observed [98]. To account for both types of noise, it has been proposed to use a Voigt spectrum given by the convolution of a Lorentzian with a Gaussian line shape [101, 102]. Thus, on short timescales around 1 µs, the frequency noise spectrum can be modeled as constant in frequency. The analysis of the self-heterodyne measurement described below assumes a white noise spectrum. For a long 100 ms integration time, the frequency flicker noise contributions have to be taken into account. The expected line shape is therefore a Voigt profile.

The self-heterodyne technique [103] uses a Mach-Zehnder type interferometer with a long delaying fiber in one arm and an acousto-optical modulator (AOM) in the other arm. The length of the fiber determines the delay between the two light components brought into interference. They have left the laser resonator at different points in time and the temporal distance between them defines the integration time of the measurement. A fast photodiode is used to capture the beat note of the two interfering light pathways. The AOM is used to shift the beat note signal away from DC to a higher frequency, where the noise gives a smaller contribution facilitating the detection with a spectrum analyzer.

The integration timescale for this measurement is around 3 µs, corresponding to approxi-

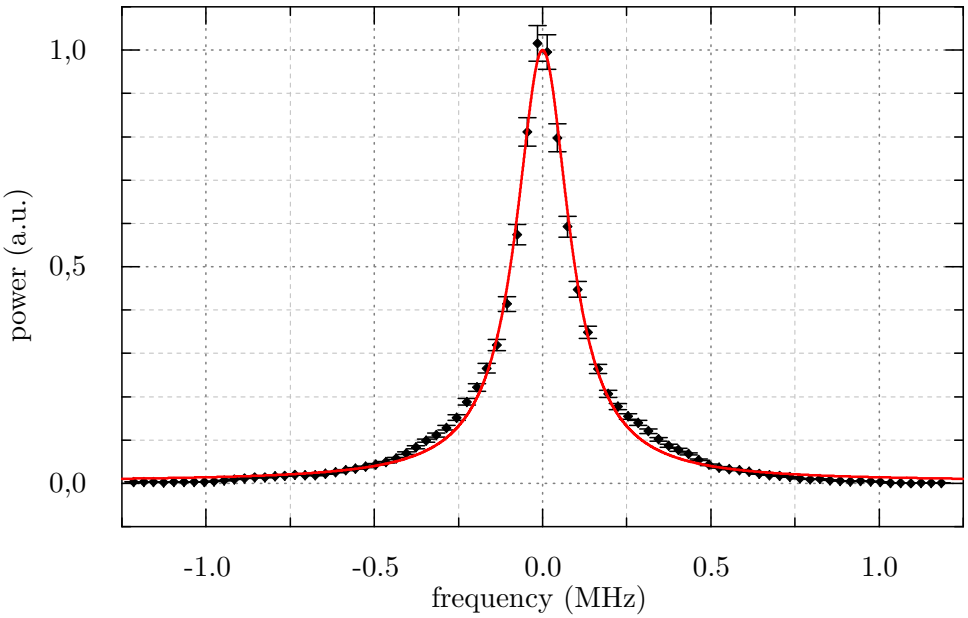

Figure 4.2: Heterodyne measurement of the superimposed signal of two similar laser systems. The data is shown in black with a Lorentzian fit in red. For details, see text.

mately 1 km of delaying fiber. Under the assumption that the noise contribution on this timescale can be modelled as white noise, the spectral distribution of the signal has been shown to become [104]:

$$S(\omega) \propto \frac{\tau_c}{1+(\omega-\Omega)^2\,\tau_c^2}\left(1-e^{-\frac{|\tau|}{\tau_c}}\left(\cos\left((\omega-\Omega)\,|\tau|\right)+\frac{\sin\left((\omega-\Omega)\,|\tau|\right)}{(\omega-\Omega)\,\tau_c}\right)\right). \\ +\pi e^{-\frac{|\tau|}{\tau_c}}\,\delta\left(\omega-\Omega\right) \tag{4.1}$$

Here, τ is the delay time of the fiber and Ω the modulation frequency of the AOM. $\delta(\nu)$ represents in this formula the Dirac delta function. The coherence time τ_c characterizes the length of coherent emission from the laser and is closely related to the FWHM linewidth by

$$\Delta\nu_{\text{laser}} = \frac{1}{\tau_c}. \tag{4.2}$$

The coherence time can be obtained by a fit to the beat note spectrum. The last term in equation (4.1) containing the Dirac delta function is omitted.

The measurement has been performed by the manufacturer of the laser system, Toptica Photonics AG, with light of 626 nm wavelength. The fiber has an optical path length of 980(10) m and the AOM was set to a frequency of 80 MHz/(2π). Between the laser system and the interferometer, an optical isolator was installed. The obtained frequency spectrum on the photodiode around the modulation frequency is plotted in figure 4.1.

Accounting for the noise and the overall amplification of the detection system, a fit of the form $f(\nu)[\text{dB}] = 10 \cdot \log_{10}(\sqrt{A^2_{\text{signal}} S(\nu)^2 + A^2_{\text{noise}}})$ to the logarithmic data in arbitrary

units was used, where A_{signal} and A_{noise} represent the corresponding amplitudes. The central Dirac delta peak was omitted in the fit. With a fixed modulation frequency $\Omega = 80\,\text{rad}\,\text{s}^{-1}$, the fit gives for the time delay of the interferometer arm with the fiber a value of $\tau = 3.2719\,\mu\text{s} \pm 0.0072\,\mu\text{s}$. The obtained coherence time is $\tau_c = 74.9\,\mu\text{s} \pm 7.2\,\mu\text{s}$. Signal and noise amplitudes are given by $A_{\text{noise}} = 104 \pm 11$ and $A_{\text{noise}} = (3.20 \pm 0.18) \cdot 10^{-9}$. The fit describes well the minima in the data, revealing the underlying Lorentzian with a width given by the coherence time. On the other hand, the fit does not describe well the strength of the side lobes. This behavior was observed elsewhere [102].

The linewidth has been measured at 626 nm, for the 313 nm light relevant for laser cooling, it is larger by a factor of 2. Thus the linewidth with a 3 µs integration time becomes

$$\Delta\nu_{313\,\text{nm}} = (26.7\,\text{kHz} \pm 2.6\,\text{kHz})\,. \tag{4.3}$$

This value is well below the natural linewidth of the laser cooling transition and justifies the assumption, that the laser linewidth can be neglected with regard to the resonance linewidth of the ion.

The heterodyne measurement setup uses two lasers, where equal characteristics of both light sources are assumed. The light is brought into interference on a fast photodiode. One light source is detuned with respect to the other, shifting the beat note to a frequency typically on the order of 100 MHz. The signal is analyzed with a spectrum analyzer and exhibits a convolution of the linewidths of both lasers.

For this measurement, the TA FHG pro laser described and characterized in the context of this work was used in conjunction with a laser system of the same type owned by the proton g-factor experiment at University of Mainz[1] [105] . For the detection, an Osi Optoelectronics FCI-125G-006HR fast photodiode was used in photoconductive mode with a reverse bias voltage of 15 V. The supply voltage was filtered by a simple RC low-pass filter with 15 kHz cut-off frequency to remove electronic noise. The signal was amplified using a Mini Circuits ZFL-500LN amplifier and analysed with a Rohde & Schwarz ZVL spectrum analyser. Both lasers were freely drifting with a frequency detuning of roughly 85 MHz. The spectrum analyser was scanning a frequency span from 72.05 MHz to 87.05 MHz while using a real bandwidth of 30 kHz and a sweep time of 100 ms without averaging.

The drift of the two lasers in between consecutive steps with respect to each other was removed from the obtained spectra by fitting a symmetric Gaussian to the data and thereby determining the center wavelength. The adjusted spectra were summed up with the result depicted in figure 4.2. A fit of $f(\nu) = A_{\text{noise}} + A_{\text{signal}} \cdot L(\nu, \Delta\tilde{\nu})$ with a Lorentzian line shape $L(\nu, \Delta\tilde{\nu}) = (2/\pi) \cdot (\Delta\tilde{\nu}/(4\nu^2 + \Delta\tilde{\nu}^2))$ reveals a FWHM linewidth of $\Delta\tilde{\nu}_{626\,\text{nm}} = 191.3(32)\,\text{kHz}$. A Voigt profile, being the expected line shape, has been fitted as well, converging to the shown Lorentzian line shape with a Gaussian width compatible with 0. Although a Lorentzian and a Voigt profile do not describe the observed line shape perfectly in the wings, this behavior is a hint that the noise spectrum on the chosen timescale is dominated by white noise.

It can be shown that the convolution of two Lorentzian linewidths of the same finite FWHM width $\Delta\nu$ results in a Lorentzian line shape with twice the linewidth $\Delta\tilde{\nu}$ such that $L(\nu, \Delta\nu) * L(\nu, \Delta\nu) = L(\nu, \Delta\tilde{\nu})$ with $\Delta\tilde{\nu} = 2\Delta\nu$. The obtained linewidth for both laser at

[1] The optical parts of this system, with exception of the additional out coupling option of 626 nm-light at the ALPHATRAP laser, are the same. The proton g-factor experiment laser uses a different analogue control system, it is however assumed that the diode drivers are comparable in noise performance.

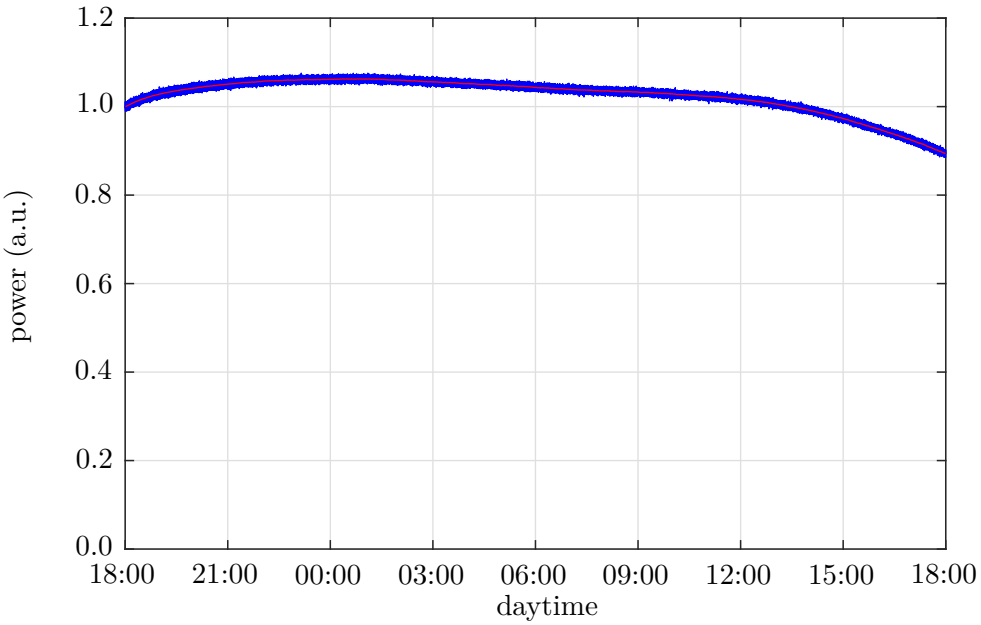

Figure 4.3: Long-term power measurement. The noisy data of the power meter (blue) was averaged over full minutes (orange).

626 nm has therefore to be multiplied by a factor of 1/2. Relevant for laser cooling is the light at 313 nm, where the linewidth of the laser is doubled during the non-linear process, yielding another factor of 2. The measured linewidth for an integration time of 100 ms thus becomes

$$\Delta\nu_{313\,\mathrm{nm}} = 191.3\,\mathrm{kHz} \pm 3.2\,\mathrm{kHz}. \tag{4.4}$$

This linewidth assumes two lasers with equal linewidth. A more conservative approach would treat the result of the measurement as an upper limit estimate for the laser linewidth of a single laser. This would result in $\Delta\nu_{313\,\mathrm{nm}} < 382.6(64)\,\mathrm{kHz}$. Even the more conservative estimate of the linewidth is well below the natural linewidth of the laser cooling transition. At a 10 Hz regulation interval of the wavelength stabilization, no significant heating due to frequency fluctuations of the laser system should occur.

4.1.2 Power

With variations in environmental parameters such as temperature and pressure, the laser power drifts slowly over time. It has been measured over 24 h to estimate the magnitude of these drifts. The measurement was performed using a PM100D power meter with a S120VC photo diode sensor, both manufactured by Thorlabs. The power as function of daytime is shown in figure 4.3.

On the eve of the measurement, the built-in power optimization using an algorithm driven alignment of the motorized in coupling mirrors to the TA, SHG and FHG has been performed. The data has been averaged over 1 min steps and 1 h steps and the maximal relative change has been calculated. A maximum drift of $0.16\,\%\,\mathrm{min}^{-1}$ for 1 min averaging

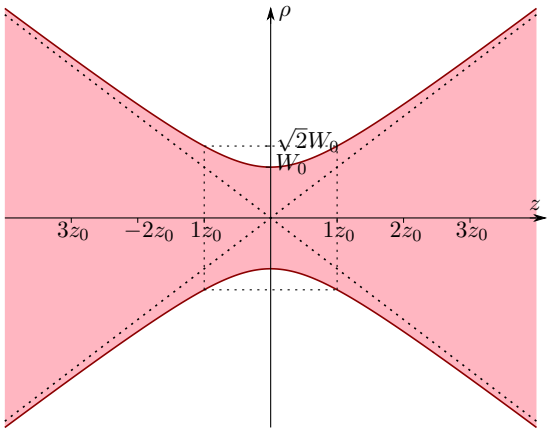

Figure 4.4: Sketch of a Gaussian beam. The envelope where the intensity dropped to $1/e^2$ with respect to the maximum is shown. The Rayleigh range z_0 describes the depth of focus and gives the distance at which the beam has broadened by a factor $\sqrt{2}$ with respect to the beam waist W_0 at the focal point.

time and a drift of $2.9\,\%\,\mathrm{h}^{-1}$ for an averaging time of 1 h have been observed. Considering the fact, that a g-factor measurement campaign takes many days, the laser power drifts significantly on these timescales and under lab conditions in an air conditioned room.

The laser has however a built-in power stabilization regulation loop measuring the power coupled out from the cavities and regulating the current in the TA. This power regulation will thus be useful to keep the power constant. This mechanism can however not correct for changing efficiencies of the fiber transport to the trap. An additional power stabilization measuring the power arriving behind the fiber might be necessary.

4.1.3 Beam Profile

Laser beams of a finite extent will weakly but significantly diverge in compliance with Heisenberg's uncertainty principle applied to the photon. A mathematical description of an ideal beam with minimal angular spread is given by the Gaussian Beam. This beam shape owes its name to the intensity distribution of Gaussian shape in radial direction. The Gaussian beam constitutes the fundamental mode of Hermite-Gaussian Beams, which can serve as a basis for the description of an arbitrary shape. Many laser beams can however be approximated by only the fundamental mode, i.e. by a Gaussian beam.

An ideal Gaussian Beam is fully characterized by two parameters. A convenient way is to choose the beam waist radius W_0 and the Rayleigh range z_0 for description. The beam waist describes the diameter of the beam in the focus, while the Rayleigh range is the distance at which the beam has broadened by a factor of $\sqrt{2}$, describing the depth of focus. The propagation of a Gaussian Beam is sketched in figure 4.4. For an ideal Gaussian Beam, the Rayleigh range and the beam waist radius are related by $z_0\lambda = \pi W_0^2$ [106]. For real laser beams, the relation between the divergence and the focusability has to be modified, introducing a beam quality factor $\mathfrak{M}^2$. The relation between beam waist and Rayleigh

range becomes

$$\mathfrak{M}^2 = \frac{\pi}{\lambda}\frac{W_0^2}{z_0}. \tag{4.5}$$

For a Gaussian beam, this value is one. Typical values for diode lasers lie within the range between 1.1 to 1.7. Helium-neon lasers typically exhibit $\mathfrak{M}^2$ values between 1 and 1.1 [93].

The intensity distribution of a Gaussian Beam propagating along the z-axis is given by

$$I(x, y, z) = I_0 \left(\frac{W_0}{W(z)}\right)^2 \exp\left(-\frac{2(x^2 + y^2)}{W(z)^2}\right), \tag{4.6}$$

where the beam width is given by [93]

$$W(z) = W_0\sqrt{1 + (z/z_0)^2}. \tag{4.7}$$

In the far field for $z \gg z_0$, the beam broadens linearly with the distance from the focal point, described by the divergence angle $\theta = W_0/z_0$. Measurement of the beam width around the focal point and around a Rayleigh range apart allows to determine the two fundamental parameters by a fit to the obtained beam width.

The profile of the 313 nm beam in a distance of 25 cm behind the laser aperture is depicted in figure 4.5. This data was taken using a beam profiler with CCD camera (Ophir Optronics Solutions SP620U). The pixel size is 4.4 µm × 4.4 µm. Several neutral density filters tilted with respect to the beam axis were used to attenuate the beam. The neutral density filters protecting the sensor are opaque for the UV light and had to be removed. Dust on the sensor and the filters cause interference leading to the rough appearance of the Gaussian shape. The beam has a pronounced excentricity roughly oriented along the preferred directions of the laser system given by the horizontal and the vertical of the laboratory system. Beam profiles are therefore measured for these two directions.

For the measurement of the beam quality factor, an aspheric lens (Thorlabs Inc. ASL10142) with a focal length of $f = 79$ mm was used. The beam profiler, mounted on a translation stage with a scale unit of 10 µm, was used to measure intensity distributions. Data was taken in a randomized order at 313.13 nm ± 0.01 nm. The obtained intensity distributions were summed over the x- and y-direction and a Gaussian line shape fitted to the sum data. Within the framework of Gaussian beams, the beam width $W(z)$ is defined as the half width where the intensity has dropped to $1/e^2$ of its maximum. The obtained data is plotted in figure 4.6 for both directions. The error bars account for the uncertainty of the fit.

The beam width as described by equation (4.7) is fitted to the obtained data. The results are summarized in table 4.1. The data shows clearly the astigmatism of the beam, probably due to the set of two cylindrical lenses used for beam shaping behind the FHG. The beam quality factor $\mathfrak{M}^2$ is approximately 1.3, in good agreement with the expected value for a diode laser. Values for both directions agree with each other within the uncertainty. Note that these values give only an upper limit for the beam quality factor. The beam quality factor is however not only influenced by the laser beam itself but also by the quality of the focusing lens. The lens used to perform the measurement under discussion is specified to be diffraction limited for wavelengths in the range 350 nm to 1620 nm and therefore the given $\mathfrak{M}^2$ constitute only an upper limit.

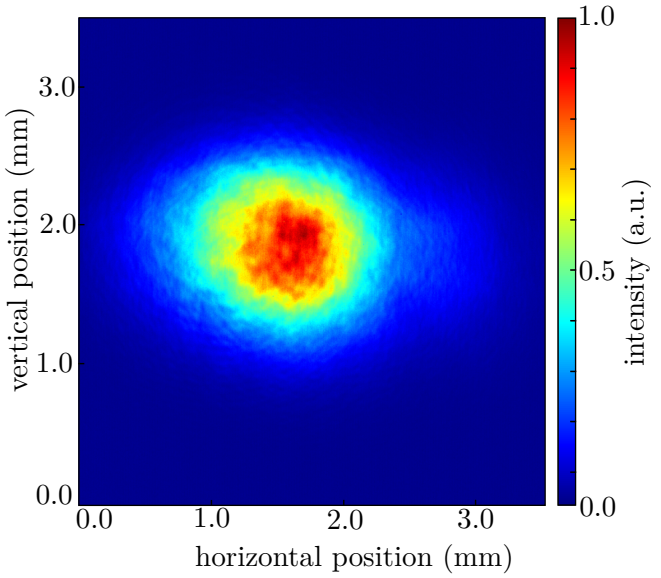

Figure 4.5: Beam profile in the radial plane of the 313 nm beam 25 cm after the beam aperture.

4.2 Wavelength Stabilization

The helium-neon laser provides a frequency standard for the calibration of the wavelength meter. Not only the linewidth of the laser on timescales of the regulation loop interval is crucial, but the wavelength meter also has to deliver accurate wavelength information. The helium-neon reference laser is assumed to provide light of a known wavelength with an accuracy of $\sigma_\nu < 2.5 \cdot 10^{-11}$, a negligible uncertainty compared to the precision of the wavelength meter. Under this assumption, the wavelength meter without frequent recalibration can be characterized against the light from the reference laser. The reference laser delivers 100 µW of light, which is coupled into a single mode fiber. Using the internal power measurement of the wavelength meter, around 3.5 µW are available for the wavelength determination after transport through a single mode fiber. This limits the minimum exposure time to a value of roughly 100 ms.

To estimate the uncertainty of the frequency measurement, the standard deviation of the

property	horizontal data	vertical data
beam waist W_0	14.69 µm ± 0.12 µm	9.85 µm ± 0.16 µm
Rayleigh range z_0	1705 µm ± 30 µm	753 µm ± 20 µm
beam quality factor $\mathfrak{M}^2$	1.270 ± 0.031	1.293 ± 0.055

Table 4.1: Summary of Gaussian beam parameters obtained by a fit to the measured beam width data in figure 4.6.

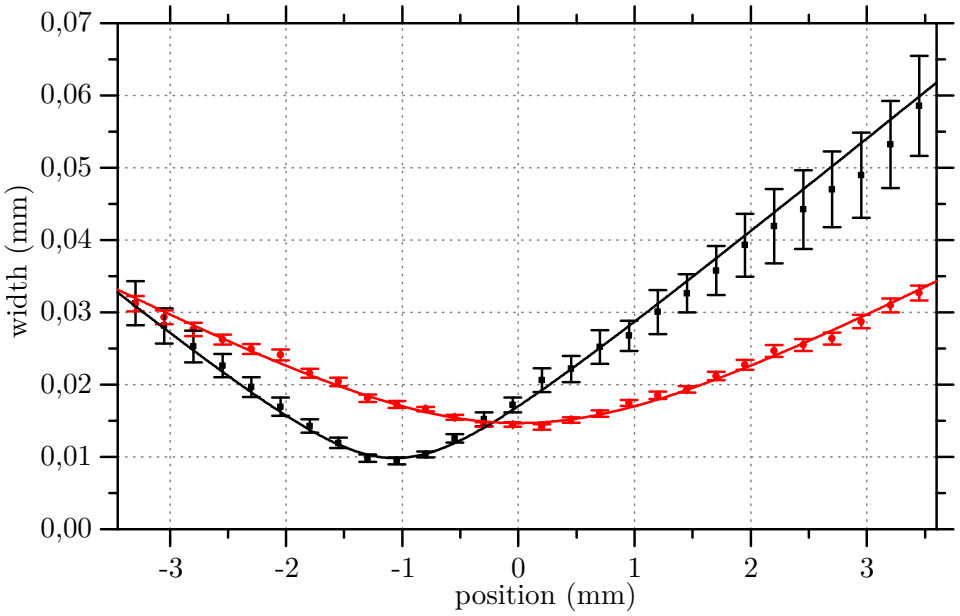

Figure 4.6: Beam width of a Gaussian Beam measured with a diffraction limited lens. The vertical data is shown in black, the horizontal data in red. The width is defined with respect to a drop of $1/e^2$ of the maximal intensity.

measured frequencies has been calculated. Samples with different exposure times between the minimum and the maximum exposure time of 10 s have been taken. The results are plotted in figure 4.7. The frequency uncertainty at an exposure time of 100 ms is 181.6 kHz. A slight trend to higher standard deviation at longer exposure times can be observed. This is due to drifts of the wavelength meter on long time scales.

To characterize the time stability of the frequency measurement, again as function of exposure time, the Allan variances of the measured frequencies of the reference laser have been calculated. If the samples of a series of measured frequencies are given by ν_i and the expectation value is denoted by $\langle\cdot\rangle$, the Allan deviation is defined as

$$\sigma_\nu(\tau) = \sqrt{\frac{1}{2}\langle(\nu_{n+1} - \nu_n)^2\rangle}. \tag{4.8}$$

The data was taken at corresponding exposure times, each sample represented by a value ν_n. The obtained values are plotted in figure 4.7.

The data shows a clear trend of decreasing Allan deviation towards longer exposure time. A turnaround is observed around 3 s, where the drift of the wavelength meter becomes dominant over the noise. The best performance of the device is thus at exposure times around this timescale. The minimal measured Allan deviation is 3.2×10^{-10} at an exposure time of 3.2 s. With this value at hand, one could make a worst case estimate of the drift of the wavelength meter between two consecutive recalibration processes with the helium-neon

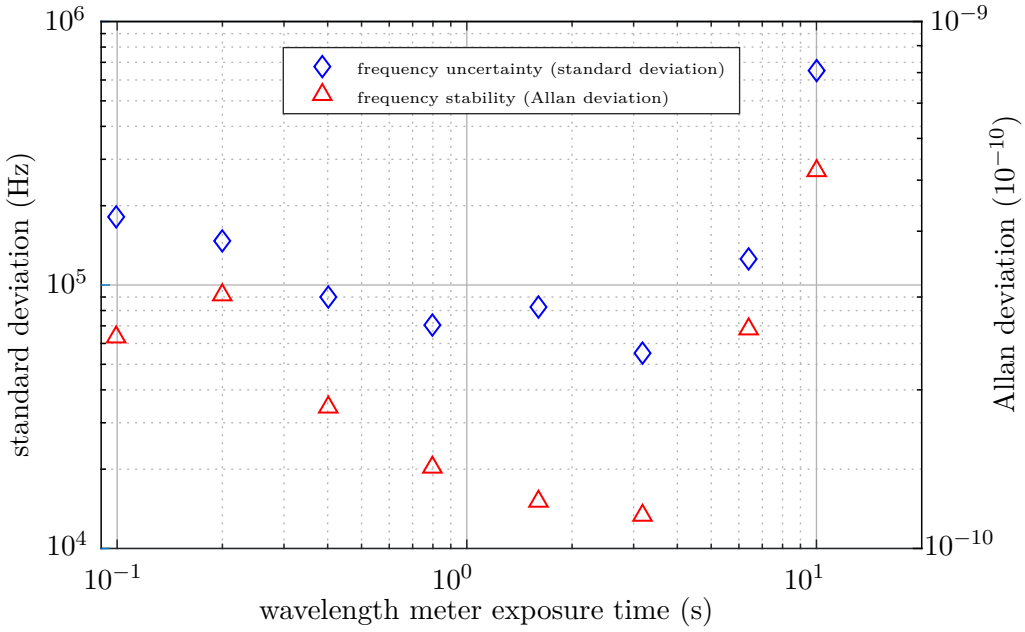

Figure 4.7: Noise and stability of the wavelength meter measured against the helium-neon laser. The standard deviations of a set of individual subsequent samples as a function of exposure time are plotted as diamonds. Additionally the Allan deviation of this sample is calculated, represented by the triangles. The overall measurement time for each data point was 10.14 min.

reference laser, repeated every 2 min:

$$\left(\left(3.2 \cdot 10^{-10} + 1\right)^{\frac{120\,\mathrm{s}}{3.2\,\mathrm{s}}} - 1\right) \cdot 957\,\mathrm{THz} = 11.48\,\mathrm{MHz}. \tag{4.9}$$

This value is still below the natural linewidth of the cooling transition.

To obtain an estimate of the optimal regulation time interval, the Allan deviation of light of the cooling laser in a freely drifting wavelength meter has been determined additionally. The result is shown in figure 4.8. A minimum can be observed around 100 ms. This constitutes the optimal regulation interval. From comparison of the observed minima in figures 4.7 and 4.8, it becomes apparent that the drifts of the laser limit the stability at lower exposure times than the drifts of the wavelength meter. Active regulation of the laser frequency will increase the wavelength stability.

4.3 Conclusion

For efficient cooling, the laser linewidth should be significantly below the natural transition wavelength. This requirement has to hold on all timescales below the time interval on which the laser frequency is actively regulated. Measurements of the linewidth with a 3 µs integration time reveal a frequency of 26.7(26) kHz. This linewidth is in agreement

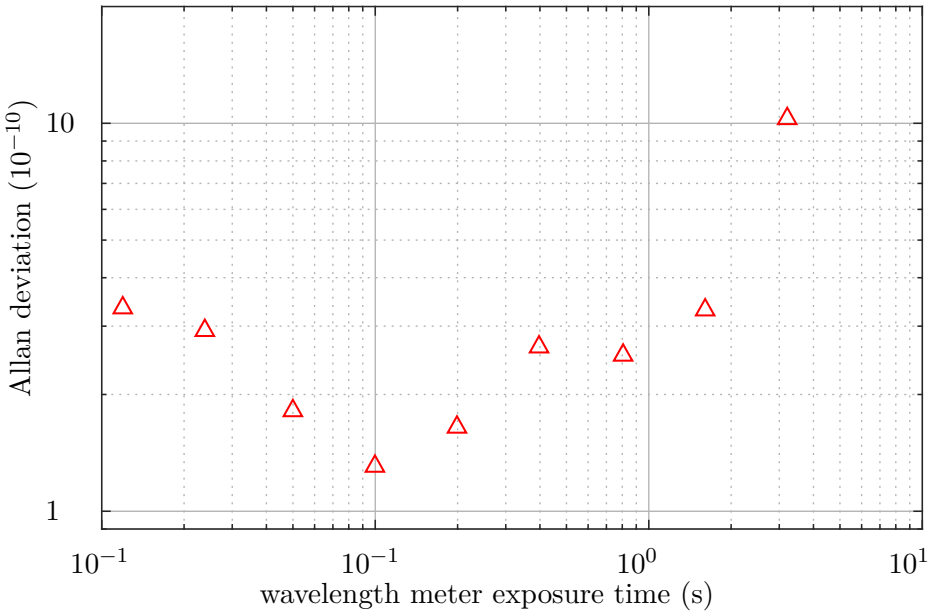

Figure 4.8: Stability of the laser measured with an uncalibrated wavelength meter. The Allan deviation as a function of exposure time is shown. The overall measurement time for each data point was 1 min. Wavelength meter and laser are freely drifting.

with typical linewidths of External Cavity Laser Diodes, as reported in references. The measurement of the linewidth with an integration time of 100 ms is of particular interest to ensure frequency stability between two regulation intervals. The measured value of 191.3(32) kHz is two orders of magnitude below the natural linewidth of the cooling transition. Frequency drifts with characteristic timescales above 100 ms will be avoided by the wavelength stabilization.

For this purpose, an accurate measurement of the frequency is necessary. The frequency measurement has been shown to have a frequency uncertainty of 181.6 kHz for an 100 ms interval. The accuracy is ensured by frequent calibration with the helium-neon reference laser with stabilization to a I_2 transition. The optimal time scale for the wavelength regulation interval has been found to be around 100 ms.

The beam quality factor has been measured and is with an upper limit of $\mathfrak{M}^2 \approx 1.3$ within the expectations for a diode laser. The necessity for power stabilization is emphasized by the results of a long-term power measurement, as data taken should be independent of environmental parameters and the shifts depend via the achievable ion temperature on the laser power.

In combination with a successful test of the achievable wavelengths, it has been shown that the requirements on the wavelength stability specified in section 3.3 are fulfilled.

5 Outlook

In the context of this thesis, the laser system for laser cooling of $^{9}Be^{1+}$ ions has been commissioned. A suitable mechanism for laser cooling with beryllium has been evaluated in the third chapter. The interaction of the external magnetic field of the Penning trap with the nuclear and electronic spin alters the energy of the electronic energy levels of the ion. Shifts for the magnetic field in the ALPHATRAP precision and analysis trap are summarized in table 3.3. The intrinsic repumping mechanism has been evaluated under the given circumstances at ALPHATRAP, revealing that a sufficiently fast repumping process should take place. As a result, specifications of a suitable laser system have been discussed. Key requirements are a wavelength at an integration time of 100 ms significantly below the natural linewidth of the chosen cooling transition and a frequency stabilization with an accuracy better than 2 MHz.

The linewidth has been measured in the context of this thesis with the results presented in the fourth chapter. It has been found that the Laser systems meets the requirements. The stability and precision of the wavelength meter has been characterized. Only the absolute accuracy of the frequency measurement could not be verified in the context of this thesis, as no suitable independent frequency standard was available. Additionally, the spatial characteristics of the laser beam have been investigated. These parameters play an important role in the design of the light transport to the trap, including coupling to an optical photonic crystal fiber.

Implementation and testing of the light transport into the trap constitute the next important step towards laser cooling of beryllium ions at ALPHATRAP. This does not only include the mechanical adjustment of the laser beam, but necessitates also suitable vacuum viewports, transparent at the same time to microwaves and ultraviolet laser light. For the transport of the ultraviolet light, a hydrogen loaded fiber is necessary. Tests of suitable single-mode photonic crystal fiber are currently in progress.

After the successful completion of the assembly and commissioning, ALPHATRAP is expected to measure the g-factor of highly charged ions. As a successor of the g-factor experiment at University of Mainz, delivering data on many light ions with a low to medium atomic number Z, ALPHATRAP will focus on heavy HCI and their extreme electromagnetic field strengths, extending the validated range of BS-QED. A first candidate would be $^{131}Xe^{53+}$, where laser cooling will help to make the spin state detection more reliable. Laser access to the trap also extends the experimental capabilities, making ALPHATRAP additionally an versatile laser spectroscopy experiment. With an independent spin state detection at hand, spectroscopy can be significantly simplified in special cases. The main advantage of laser cooling is however the expected formation of Coulomb crystals in a trap suitable for high precision measurement of g-factors. This prospect builds a base for the direct phase-sensitive measurement of g-factor differences. These new techniques allows for instance, among other interesting experiments, the measurement of the fine structure constant, such that ALPHATRAP will live up to its name.

Bibliography

[1] J. Schwinger, *On Quantum-Electrodynamics and the Magnetic Moment of the Electron,* Physical Review **73**, 416 (1948).

[2] W. E. Lamb Jr and R. C. Retherford, *Fine Structure of the Hydrogen Atom by a Microwave Method,* Physical Review **72**, 241 (1947).

[3] D. Hanneke, S. Fogwell, and G. Gabrielse, *New Measurement of the Electron Magnetic Moment and the Fine Structure Constant,* Physical Review Letters **100**, 120801 (2008).

[4] T. Aoyama, M. Hayakawa, T. Kinoshita, and M. Nio, *Tenth-order QED Contribution to the Electron g-2 and an Improved Value of the Fine Structure Constant,* Physical Review Letters **109**, 111807 (2012).

[5] H. Häffner, T. Beier, N. Hermanspahn, H.-J. Kluge, W. Quint, S. Stahl, J. Verdú, and G. Werth, *High-Accuracy Measurement of the Magnetic Moment Anomaly of the Electron Bound in Hydrogenlike Carbon,* Physical Review Letters **85**, 5308 (2000).

[6] J. Verdú, S. Djekić, S. Stahl, T. Valenzuela, M. Vogel, G. Werth, T. Beier, H.-J. Kluge, and W. Quint, *Electronic g-Factor of Hydrogenlike Oxygen* $^{16}O^{7+}$*,* Physical Review Letters **92**, 093002 (2004).

[7] A. Wagner, S. Sturm, F. Köhler, D. A. Glazov, A. V. Volotka, G. Plunien, W. Quint, G. Werth, V. M. Shabaev, and K. Blaum, *g-Factor of Lithiumlike Silicon* $^{28}Si^{11+}$*,* Physical Review Letters **110**, 033003 (2013).

[8] S. Sturm, A. Wagner, B. Schabinger, J. Zatorski, Z. Harman, W. Quint, G. Werth, C. H. Keitel, and K. Blaum, *g-Factor of Hydrogenlike* $^{28}Si^{13+}$*,* Physical Review Letters **107**, 023002 (2011).

[9] F. Köhler, K. Blaum, M. Block, S. Chenmarev, S. Eliseev, D. A. Glazov, M. Goncharov, J. Hou, A. Kracke, D. A. Nesterenko, *et al.*, *Isotope Dependence of the Zeeman effect in lithium-like calcium,* Nature Communications **7** (2016), 10.1038/ncomms10246.

[10] S. Sturm, F. Köhler, J. Zatorski, A. Wagner, Z. Harman, G. Werth, W. Quint, C. H. Keitel, and K. Blaum, *High-precision measurement of the atomic mass of the electron,* Nature **506**, 467–470 (2014).

[11] J. Schwinger, *On Gauge Invariance and Vacuum Polarization,* Physical Review **82**, 664 (1951).

[12] D. Wineland, J. Bollinger, and W. M. Itano, *Laser-Fluorescence Mass Spectroscopy,* Physical Review Letters **50**, 628 (1983).

[13] C. Monroe, D. Meekhof, B. King, W. M. Itano, and D. J. Wineland, *Demonstration of a Fundamental Quantum Logic Gate,* Physical Review Letters **75**, 4714 (1995).

[14] A. Landé, *Über den anomalen Zeemaneffekt (Teil I),* Zeitschrift für Physik A **5**, 231–241 (1921).

[15] G. E. Uhlenbeck and S. Goudsmit, *Ersetzung der Hypothese vom unmechanischen Zwang durch eine Forderung bezüglich des inneren Verhaltens jedes einzelnen Elektrons,* Naturwissenschaften **13**, 953–954 (1925).

[16] W. Pauli, *Zur Quantenmechanik des magnetischen Elektrons,* Zeitschrift für Physik **43**, 601–623 (1927).

[17] P. A. Dirac, *The Quantum Theory of the Electron,* Proceedings of the Royal Society of London A , 610–624 (1928).

[18] P. Kusch and H. Foley, *The Magnetic Moment of the Electron,* Physical Review **74**, 250 (1948).

[19] G. Breit, *The Magnetic Moment of the Electron,* Nature **122**, 649 (1928).

[20] T. Beier, *The g_j factor of a bound electron and the hyperfine structure splitting in hydrogenlike ions,* Physics Reports **339**, 79–213 (2000).

[21] H. Margenau, *Relativistic Magnetic Moment of a Charged Particle,* Physical Review **57**, 383 (1940).

[22] R. S. Van Dyck Jr, P. B. Schwinberg, and H. G. Dehmelt, *New high-precision comparison of electron and positron g-factors,* Physical Review Letters **59**, 26 (1987).

[23] D. A. Glazov, A. V. Volotka, V. M. Shabaev, and G. Plunien, QED Theory of the Bound-Electron Magnetic Moment, in *Fundamental physics in particle traps*, Vol. 256, edited by W. Quint and M. Vogel (Springer, 2014) Chap. 4.

[24] K. Pachucki, A. Czarnecki, U. D. Jentschura, and V. A. Yerokhin, *Complete two-loop correction to the bound-electron g-factor,* Physical Review A **72**, 022108 (2005).

[25] F. Sauter, *Über das Verhalten eines Elektrons im homogenen elektrischen Feld nach der relativistischen Theorie Diracs,* Zeitschrift für Physik A **69**, 742–764 (1931).

[26] S. K. Suslov, *Expectation values in relativistic Coulomb problems,* Journal of Physics B: Atomic, Molecular and Optical Physics **42**, 185003 (2009).

[27] M. Hayakawa, Theory of Anomalous Magnetic Dipole Moments of the Electron, in *Fundamental Physics in Particle Traps*, edited by W. Quint and M. Vogel (Springer, 2014) Chap. 2.

[28] D. Glazov and V. Shabaev, *Finite nuclear size correction to the bound-electron g-factor in a hydrogenlike atom,* Physics Letters A **297**, 408–411 (2002).

[29] V. Shabaev, *QED theory of the nuclear recoil effect on the atomic g-factor,* Physical Review A **64**, 052104 (2001).

[30] A. V. Volotka and G. Plunien, *Nuclear Polarization Study: New Frontiers for Tests of QED in Heavy Highly Charged Ions,* Physical Review Letters **113**, 023002 (2014).

[31] S. Sturm, private communication (2017).

[32] V. Shabaev, D. Glazov, N. Oreshkina, A. Volotka, G. Plunien, H.-J. Kluge, and W. Quint, *g-Factor of Heavy Ions: A New Access to the Fine Structure Constant,* Physical Review Letters **96**, 253002 (2006).

[33] V. Yerokhin, E. Berseneva, Z. Harman, I. Tupitsyn, and C. H. Keitel, *g-Factor of Light Ions for an Improved Determination of the Fine-Structure Constant,* Physical Review Letters **116**, 100801 (2016).

[34] H. Dehmelt, *Continuous Stern-Gerlach effect: Principle and idealized apparatus,* Proceedings of the National Academy of Sciences **83**, 2291–2294 (1986).

[35] S. Sturm, *The g-factor of the electron bound in* $^{28}Si^{13+}$*: The most stringent test of bound-state quantum electrodynamics*, Ph.D. thesis, Universität Heidelberg (2011).

[36] H. Häffner, T. Beier, S. Djekić, N. Hermanspahn, H.-J. Kluge, W. Quint, S. Stahl, J. Verdú, T. Valenzuela, and G. Werth, *Double Penning-trap technique for precise g-factor determinations in highly charged ions,* The European Physical Journal D-Atomic, Molecular, Optical and Plasma Physics **22**, 163–182 (2003).

[37] S. Earnshaw, *On the Nature of the Molecular Forces which regulate the Constitution of the Luminiferous Ether,* Trans. Camb. Phil. Soc **7**, 97–112 (1842).

[38] F. Penning, *Ein neues Manometer für niedrige Gasdrucke, insbesondere zwischen* 10^{-3} *und* 10^{-5} *mm,* Physica **4**, 71–75 (1937).

[39] J. L. V. Galiana, *Ultrapräzise Messung des elektronischen g-Faktors in wasserstoffähnlichem Sauerstoff*, Ph.D. thesis, Johannes Gutenberg-Universität Mainz (2003).

[40] G. Gabrielse and F. C. MacKintosh, *Cylindrical Penning traps with orthogonalized anharmonicity compensation,* International Journal of Mass Spectrometry and Ion Processes **57**, 1–17 (1984).

[41] F. G. Major, V. N. Gheorghe, and G. Werth, *Charged Particle Traps: Physics and Techniques of Charged Particle Field Confinement*, Vol. 37 (Springer, 2006).

[42] M. Vogel and W. Quint, Magnetic Moment of the Bound Electron, in *Fundamental Physics in Particle Traps*, Vol. 256, edited by W. Quint and M. Vogel (Springer, 2014) Chap. 3.

[43] L. S. Brown and G. Gabrielse, *Geonium theory: Physics of a single electron or ion in a Penning trap,* Reviews of Modern Physics **58**, 233 (1986).

[44] S. Ulmer, *First observation of spin flips with a single proton stored in a cryogenic Penning trap*, Ph.D. thesis, Universität Heidelberg (2011).

[45] D. Wineland and H. Dehmelt, *Principles of the stored ion calorimeter,* Journal of Applied Physics **46**, 919–930 (1975).

[46] C. Patrignani, P. Richardson, O. Zenin, R.-Y. Zhu, A. Vogt, S. Pagan Griso, L. Garren, D. Groom, M. Karliner, D. Asner, *et al.*, *Review of Particle Physics,* Chin. Phys. C **40**, 100001 (2016).

[47] E. A. Cornell, R. M. Weisskoff, K. R. Boyce, and D. E. Pritchard, *Mode coupling in a Penning trap: π pulses and a classical avoided crossing,* Physical Review A **41**, 312 (1990).

[48] S. Sturm, A. Wagner, B. Schabinger, and K. Blaum, *Phase-Sensitive Cyclotron Frequency Measurements at Ultralow Energies,* Physical Review Letters **107**, 143003 (2011).

[49] J. Ketter, T. Eronen, M. Höcker, S. Streubel, and K. Blaum, *First-order perturbative calculation of the frequency-shifts caused by static cylindrically-symmetric electric and magnetic imperfections of a Penning trap,* International Journal of Mass Spectrometry **358**, 1–16 (2014).

[50] D. Winters, M. Vogel, D. Segal, and R. Thompson, *Electronic detection of charged particle effects in a Penning trap,* Journal of Physics B: Atomic, Molecular and Optical Physics **39**, 3131 (2006).

[51] D. J. Wineland, R. E. Drullinger, and F. L. Walls, *Radiation-Pressure Cooling of Bound Resonant Absorbers,* Physical Review Letters **40**, 1639 (1978).

[52] T. W. Hänsch and A. L. Schawlow, *Cooling of gases by laser radiation,* Optics Communications **13**, 68–69 (1975).

[53] W. Neuhauser, M. Hohenstatt, P. Toschek, and H. Dehmelt, *Optical-Sideband Cooling of Visible Atom Cloud Confined in Parabolic Well,* Physical Review Letters **41**, 233 (1978).

[54] W. D. Phillips and H. Metcalf, *Laser Deceleration of an Atomic Beam,* Physical Review Letters **48**, 596 (1982).

[55] S. Chu, L. Hollberg, J. E. Bjorkholm, A. Cable, and A. Ashkin, *Three-dimensional viscous confinement and cooling of atoms by resonance radiation pressure,* Physical Review Letters **55**, 48 (1985).

[56] C. J. Foot, *Atomic Physics*, Vol. 7 (Oxford University Press, 2005).

[57] T. Andersen, K. Jessen, and G. Sørensen, *Mean-Life Measurements of Excited Electronic States in Neutral and Ionic Species of Beryllium and Boron,* Physical Review **188**, 76 (1969).

[58] W. M. Itano and D. Wineland, *Laser cooling of ions stored in harmonic and Penning traps,* Physical Review A **25**, 35 (1982).

[59] J. Eschner, G. Morigi, F. Schmidt-Kaler, and R. Blatt, *Laser cooling of trapped ions,* JOSA B **20**, 1003–1015 (2003).

[60] H. Powell, D. Segal, and R. Thompson, *Axialization of Laser Cooled Magnesium Ions in a Penning Trap,* Physical Review Letters **89**, 093003 (2002).

[61] R. Drullinger, D. Wineland, and J. Bergquist, *High-resolution optical spectra of laser cooled ions,* Applied Physics A: Materials Science & Processing **22**, 365–368 (1980).

[62] J. Bollinger, J. Wells, D. Wineland, and W. M. Itano, *Hyperfine structure of the* $2p^2P_{1/2}$ *state in* $^9Be^+$*,* Physical Review A **31**, 2711 (1985).

[63] K. Koo, J. Sudbery, D. Segal, and R. Thompson, *Doppler cooling of* Ca^+ *ions in a Penning trap,* Physical Review A **69**, 043402 (2004).

[64] A. Kramida, Y. Ralchenko, J. Reader, and and NIST ASD Team, NIST Atomic Spectra Database (ver. 5.3), [Online, 2017, June 12]. National Institute of Standards and Technology, Gaithersburg, MD. `http://physics.nist.gov/asd` (2015).

[65] D. Larson, J. C. Bergquist, J. J. Bollinger, W. M. Itano, and D. J. Wineland, *Sympathetic cooling of trapped ions: A laser-cooled two-species nonneutral ion plasma,* Physical Review Letters **57**, 70 (1986).

[66] H. Imajo, K. Hayasaka, R. Ohmukai, U. Tanaka, M. Watanabe, and S. Urabe, *High-resolution ultraviolet spectra of sympathetically-laser-cooled Cd+ ions,* Physical Review A **53**, 122 (1996).

[67] M. Van Eijkelenborg, M. Storkey, D. Segal, and R. Thompson, *Sympathetic cooling and detection of molecular ions in a Penning trap,* Physical Review A **60**, 3903 (1999).

[68] L. Gruber, J. P. Holder, and D. Schneider, *Formation of Strongly Coupled Plasmas from Multicomponent Ions in a Penning Trap,* Physica scripta **71**, 60 (2005).

[69] J. Yu, M. Desaintfuscien, and F. Plumelle, *Ion density limitation in a Penning trap due to the combined effect of asymmetry and space charge,* Applied Physics B: Lasers and Optics **48**, 51–54 (1989).

[70] R. C. Thompson, *Ion Coulomb crystals,* Contemporary Physics **56**, 63–79 (2015).

[71] M. Jones and D. Ceperley, *Crystallization of the One-Component Plasma at Finite Temperature,* Physical Review Letters **76**, 4572 (1996).

[72] K. R. Brown, C. Ospelkaus, Y. Colombe, A. C. Wilson, D. Leibfried, and D. J. Wineland, *Coupled quantized mechanical oscillators,* Nature **471**, 196–199 (2011).

[73] A. Egl, Comissioning of the Offline Transfer Beamline for the ALPHATRAP Experiment, Master thesis, Universität Heidelberg (2016).

[74] J. Crespo López-Urrutia, J. Braun, G. Brenner, H. Bruhns, *et al.*, *Optimization of the charge state distribution of the ion beam extracted from an EBIT by dielectronic recombination,* Review of scientific instruments **75**, 1560–1562 (2004).

[75] T. Sailer, A Laser Ion Source for the ALPHATRAP Experiment, Master thesis, Universität Heidelberg (2017).

[76] M. Turkalj Oreskovic, Development of a cryogenic vacuum valve and an eletromechanical switch for ALPHATRAP, Master thesis, Universität Heidelberg (2014).

[77] A. Weigel, Entwicklung des kryogenen Nachweissystems für ALPHATRAP und THe-Trap, Master thesis, Universität Heidelberg (2014).

[78] H. Alloul and C. Froidevaux, *Nuclear spin relaxation in beryllium metal,* Journal of Physics and Chemistry of Solids **29**, 1623–1631 (1968).

[79] G. Breit and I. Rabi, *Measurement of Nuclear Spin,* Physical Review **38**, 2082 (1931).

[80] N. Shiga, W. M. Itano, and J. J. Bollinger, *Diamagnetic correction to the $^9Be^+$ ground-state hyperfine constant,* Physical Review A **84**, 012510 (2011).

[81] W. M. Itano, *Chemical shift correction to the Knight shift in beryllium,* Physical Review B **27**, 1906 (1983).

[82] M. Puchalski and K. Pachucki, *Fine and hyperfine splitting of the $2P$ state in Li and Be^+,* Physical Review A **79**, 032510 (2009).

[83] C. Cohen-Tannoudji, B. Diu, and F. Laloë, *Quantenmechanik* (De Gruyter Berlin/New York, 1999).

[84] W. M. Itano and D. Wineland, *Precision measurement of the ground-state hyperfine constant of $^{25}Mg^+$,* Physical Review A **24**, 1364 (1981).

[85] D. Budker, D. F. Kimball, and D. P. DeMille, *Atomic physics: an exploration through problems and solutions* (Oxford University Press, USA, 2004).

[86] Toptica Photonics AG, Scientific lasers, Brochure br-199-54a (2015).

[87] L. Ricci, M. Weidemüller, T. Esslinger, A. Hemmerich, C. Zimmermann, V. Vuletic, W. König, and T. W. Hänsch, *A compact grating-stabilized diode laser system for atomic physics,* Optics Communications **117**, 541–549 (1995).

[88] S. D. Saliba and R. E. Scholten, *Linewidths below 100 kHz with external cavity diode lasers,* Applied optics **48**, 6961–6966 (2009).

[89] F. Rohde and J. Eschner, *Remote ion traps for quantum networking: Two-photon interference and correlations*, Ph.D. thesis, PhD thesis, ICFO—The Institute of Photonic Sciences (2009).

[90] R. Drever, J. L. Hall, F. Kowalski, J. Hough, G. Ford, A. Munley, and H. Ward, *Laser phase and frequency stabilization using an optical resonator,* Applied Physics B **31**, 97–105 (1983).

[91] Mise en pratique: Iodinie ($\lambda \approx 633$ nm), Bureau International des Poids et Mesures (2003).

[92] C. D. Marciniak, H. B. Ball, A. T.-H. Hung, and M. J. Biercuk, *Towards fully commercial, UV-compatible fiber patch cords,* Optics express **25**, 15643–15661 (2017).

[93] B. E. Saleh, M. C. Teich, and B. E. Saleh, *Fundamentals of Photonics*, 2nd ed. (Wiley New York, 2007).

[94] Y. Colombe, D. H. Slichter, A. C. Wilson, D. Leibfried, and D. J. Wineland, *Single-mode optical fiber for high-power, low-loss UV transmission,* Optics express **22**, 19783–19793 (2014).

[95] F. Gebert, M. Frosz, T. Weiss, Y. Wan, A. Ermolov, N. Joly, P. Schmidt, and P. S. J. Russell, *Damage-free single-mode transmission of deep-UV light in hollow-core PCF,* Optics express **22**, 15388–15396 (2014).

[96] A. L. Schawlow and C. H. Townes, *Infrared and Optical Masers,* Physical Review **112**, 1940 (1958).

[97] C. Henry, *Theory of the linewidth of semiconductor lasers,* IEEE Journal of Quantum Electronics **18**, 259–264 (1982).

[98] K. Petermann, *Laser diode modulation and noise*, Vol. 3 (Springer, 2012).

[99] Y. Salvadé and R. Dändliker, *Limitations of interferometry due to the flicker noise of laser diodes,* JOSA A **17**, 927–932 (2000).

[100] G. Di Domenico, S. Schilt, and P. Thomann, *Simple approach to the relation between laser frequency noise and laser line shape,* Applied optics **49**, 4801–4807 (2010).

[101] S. Viciani, M. Gabrysch, F. Marin, F. M. di Sopra, M. Moser, and K. H. Gulden, *Lineshape of a vertical cavity surface emitting laser,* Optics communications **206**, 89–97 (2002).

[102] L. B. Mercer, *1/f frequency noise effects on self-heterodyne linewidth measurements,* Journal of Lightwave Technology **9**, 485–493 (1991).

[103] T. Okoshi, K. Kikuchi, and A. Nakayama, *Novel method for high resolution measurement of laser output spectrum,* Electronics letters **16**, 630–631 (1980).

[104] L. Richter, H. Mandelberg, M. Kruger, and P. McGrath, *Linewidth determination from self-heterodyne measurements with subcoherence delay times,* IEEE Journal of Quantum Electronics **22**, 2070–2074 (1986).

[105] C. C. Rodegheri, K. Blaum, H. Kracke, S. Kreim, A. Mooser, W. Quint, S. Ulmer, and J. Walz, *An experiment for the direct determination of the g-factor of a single proton in a Penning trap,* New Journal of Physics **14**, 063011 (2012).

[106] H. J. Eichler and J. Eichler, *Laser: Bauformen, Strahlführung, Anwendungen* (Springer, 2015).

Erklärung

Ich versichere, dass ich diese Arbeit selbständig verfasst und keine anderen als die angegebenen Quellen und Hilfsmittel benutzt habe.

Sandro Kraemer — Heidelberg am 10. August 2017

Danksagung

Mein herzlichen Dank gilt zunächst dir, Klaus. Du hast mir die Möglichkeit gegeben, meine Passion für experimentelle Physik immer wieder neu zu entdecken und leidenschaftlich und konzentriert über einen längeren Zeitraum an einem Projekt wie ALPHATRAP zu arbeiten. Gleichzeitig hast du mich aber auch immer dabei unterstützt, über den Tellerrand hinaus zu blicken. Dein offenes Ohr und dein Rat waren mir eine große Hilfe.

Für die ausgezeichnete Betreuung und drei für mich persönlich sehr lehrreiche Jahre möchte ich dir, Sven, besonders danken. In zahllosen Diskussionen hast du uns unermüdlich die großen Zusammenhänge und die kleinen Feinheiten der Experimentalphysik näher gebracht.

ALPHATRAP wäre nicht ALPHATRAP ohne die vielen fleißigen Hände und Köpfe, die tagtäglich an großen und kleinen Problemen tüfteln. Alex, Andi, Ioanna, Martin, Robert und Tim, thanks to all of you for a really great time at ALPHATRAP!

I would also like to thank Matthew, Georg and Andreas for all the support you gave us, whenever we burst in into your lab in Mainz. You advanced ALPHATRAP a big step forward.